

Controlled Manipulation of Engineered Colloidal Particles

Janine Nunes

A dissertation submitted to the faculty of the University of North Carolina at Chapel Hill in partial fulfillment of the requirements for the degree of Doctor of Philosophy in the Department of Chemistry

Chapel Hill
2010

Approved by

Joseph M. DeSimone

Edward T. Samulski

Michael Rubinstein

M. Gregory Forest

Sergei Sheiko

© 2010
Janine Nunes
ALL RIGHTS RESERVED

Abstract

Janine Nunes: Controlled Manipulation of Engineered Colloidal Particles
(Under the direction of Joseph M. DeSimone)

This research utilized the Particle Replication in Non-wetting Templates (PRINT[®]) technology to fabricate highly tailored colloidal particles. The behavior of these engineered particles were studied as they were subjected to different precisely controlled external influences, including electric fields, magnetic fields and a templating approach based on the PRINT process. Given the tunability in particle properties afforded by the PRINT process, exceptional control of the resulting particle assemblies and particle mobility were observed, suggesting potential applications in numerous materials and life science applications that require control on the nanoscale.

As the PRINT process was integral to all aspects of this research, it was important to gain a clear understanding of mechanism by which perfluoropolyether (PFPE) elastomeric molds can generate monodisperse arrays of discrete, uniform particles with tailored size, shape and composition. Thus, fundamental studies were conducted on the PFPE elastomers, focusing on contact mechanics measurements and capillary flow experiments. The results confirmed the low surface energy of PFPE, an important property that renders the PFPE molds ideal for the PRINT process. Capillary flow experiments were conducted to study the method by which PFPE molds can be filled during the PRINT process. The flow in closed PFPE microchannels was compared to that in PDMS and glass.

Suspensions of PRINT particles were studied in the

presence of electric and magnetic fields. Electric field experiments were conducted using non-uniform alternating current electric fields and uniform direct current electric fields. Magnetic field experiments were conducted using both stationary and rotating magnetic fields. Particle assemblies were observed to form and could be tuned by particle shape and composition. Particle motion, both translational and rotational, was also controlled. Properties were found to be both shape and composition dependent. These experiments were applied to the fabrication of steerable micromotors and the driving of deformable particles through confined environments.

Using the inherent templating nature of the PRINT process, highly ordered polymer composite films were fabricated to completely avoid particle aggregation. The fabrication process was optimized for different compositions and film nanostructures. These experiments were applied to the fabrication of dielectric composite films for capacitors.

To my brother, Justin Nunes (1984 – 2007), you were the best part of all of us

To my mother, Beverly Nunes

To my brother, Joel Nunes

Acknowledgements

There are many people to whom I wish to convey my heartfelt gratitude. First, I would like to thank my advisor, Joseph DeSimone, for providing an opportunity to learn and work in a wonderful research environment. A significant amount of the work documented in this dissertation was conducted jointly with Dr. Kevin P. Herlihy, and I am forever grateful for his great ideas and motivating approach to research. I am extremely grateful for Elizabeth Enlow - for her willingness to serve as counselor, brainstorming partner, advisor and great friend. I would also like to thank Kelly Chang, who has always been willing to listen or advise as necessary. Over the years, I have had the opportunity to work with different postdoctoral associates in the DeSimone group: Dr. Benjamin Maynor, Dr. Alexander Ermoshkin, Dr. Libin Du and Dr. Merve Ertas. I thank them all for their advice and assistance. I enjoyed the collaborative atmosphere in the group and I have benefited from the knowledge and expertise of many group members who I wish to acknowledge, including Dr. Stuart Williams, Dr. Meredith Hampton, Dr. Jennifer Kelly, Ron Traud, Dr. Zhaokang Hu, Tim Merkel, Dr. Stephanie Gratton, Dr. Henry Zhang Dr. Candice Brannen and Dr. Patricia Ropp.

The surface energy experiments were conducted through a collaboration with Professor Manoj Chaudhury at Lehigh University. I would like to thank him for welcoming me into his lab for two extended visits to perform experiments. I would also like to thank his students, Hyounghwan Kim and Peter Phivilay, for their assistance. I also collaborated with the Superfine research group on some of the magnetic and electric field

Experiments, so I would like to thank Professor Richard Superfine and his students, Lamar Mair, Briana Fiser, Adam Shields and Jeremy Cribb. I would also like to express my gratitude to the personnel at the different user facilities that I worked at: Dr. Carrie Donley, Dr. Amar Kumbhar and Dr. Wallace Ambrose at the Chapel Hill Analytical and Nanofabrication Lab (CHANL); Dr. Kirk Bryson, Dr. Jay Dalton and Dr. Mark Walters at the Shared Materials Instrument Facility (SMIF, Duke University); David Vellenga and Chris Hardiman at the Nanofabrication Facility in North Carolina State University. Collin McKinney of the Department of Chemistry Electronics Facility has also been a great help.

On a personal note, I am so grateful for my family and friends. My mother and brothers have been the most amazing support system and any success that I have achieved has been because of them. It has been challenging being far away from them for so long, especially when faced with difficult times.

This work would not be possible without financial support. I acknowledge the Schlumberger Faculty for the Future Fellowship, the National Science Foundation Science and Technology Center, the Office of Naval Research, the University Cancer Research Fund and Liquidia Technologies.

Table of Contents

	Page
List of Tables	xxii
List of Figures	xxiii
List of Abbreviations and Symbols.....	xix
Chapter 1. Introduction to the Manipulation of Colloids	1
1.1 Overview	2
1.2 Particle Fabrication Methodologies	4
1.2.1 Shape Anisotropy	5
1.2.2 Chemical Anisotropy	9
1.3 Autonomous Particle Manipulation	12
1.3.1 Controlled Aggregation	12
1.3.2 Catalytic Motion	17
1.3.3 Fluidic Assembly.....	20
1.4 Externally Controlled Field Driven Manipulation of Colloids	21
1.4.1 Electric Fields	21
1.4.1.1 Electrophoresis and Electroosmosis	22
1.4.1.2 Dielectrophoresis	24
1.4.2 Magnetic Fields	26
1.4.3 Optical Fields.....	27
1.5 Applications	29
1.5.1 Smart Fluids.....	29
1.5.2 Photonic Crystals.....	30
1.5.3 Micro-electronics.....	30
1.5.4 Micro-Pumps and Micro-Motors for Lab-on-a-Chip Machinery.....	31
1.5.5 Colloidal Surfactants	31

1.5.6 <i>In vivo</i> Transport/Therapeutic Delivery	32
1.5.7 Particle-based Display Technologies	32
1.6 Summary	33
1.7 References	36
Chapter 2. PRINT [®] Technology and PFPE Characterization	44
2.1 Introduction	45
2.1.1 PRINT Technology	45
2.1.2 Solid Surface Energy Measurements.....	47
2.1.3 Capillary Flow	49
2.2 Research Objectives	50
2.3 Experimental	51
2.3.1 PFPE Synthesis.....	51
2.3.2 Contact Angle and Mechanical Characterization of PFPE Elastomers.....	52
2.3.3 JKR Studies	53
2.3.3.1 Experimental Procedure.....	53
2.3.3.2 Results and Discussion	57
2.3.4 Capillary Flow Experiments.....	62
2.3.4.1 Experimental Procedure.....	62
2.3.4.2 Results and Discussion	63
2.4 Conclusion.....	65
2.5 References	67
Chapter 3. Electrical Manipulation of PRINT Particles	69
3.1 Specific Research Objectives	70
3.2 Dielectrophoretic Assembly of PRINT Particles	70
3.2.1 Particle Fabrication and Characterization	70
3.2.2 Experimental Design and Set-up	73
3.2.3 Results and Discussion.....	75
3.3 Particle Electrophoresis in Confined Geometries	87
3.3.1 Particle Fabrication and Characterization	87
3.3.2 Experimental Design and Set-up.....	89

3.3.3 Results and Discussion	91
3.4 Summary and Future Outlook	94
3.5 References	96
Chapter 4. Magnetic Manipulation of PRINT Particles	97
4.1 Specific Research Objectives	98
4.2 Experimental	99
4.2.1 Particle Fabrication and Characterization	99
4.2.2 Magnetic Chaining Experiments	103
4.2.3 SQUID Experiments.....	103
4.2.4 Magnetic Stage Set-up for Imaging Particle Rotation and Chaining in Water	104
4.2.5 Particle Polymerization Experiment.....	104
4.2.6 Magnetic Stage Set-up for Particle Tracking Experiments in H ₂ O ₂	105
4.3 Results and Discussion.....	106
4.3.1 Magneto-Polymer PRINT Composite Particles	106
4.3.2 Magnetic Manipulation of Microscale Composite Particles	114
4.3.3 End-labeling Composite Particles for Use as Micromotors	119
4.4 Summary and Future Outlook.....	124
4.5 References	126
Chapter 5. Hierarchically Controlled PRINT Composite Thin Films	127
5.1 Specific Research Objectives	128
5.2 Experimental	129
5.2.1 Materials and Instrumentation.....	129
5.2.2 Ordered Composite Film Fabrication and Characterization.....	131
5.2.2.1 Crosslinked Polymer/Polymer Systems.....	132
5.2.2.1.1 Fabrication	132
5.2.2.1.2 Characterization.....	133
5.2.2.2 Thermoplastic Polymer Systems.....	138
5.2.2.2.1 Fabrication	138
5.2.2.2.2 Characterization.....	140
5.2.2.3 Polymer/Barium Titanate.....	142

5.2.2.3.1 Barium Titanate Sol-gel Synthesis.....	142
5.2.2.3.2 Bulk Ceramic Synthesis and Characterization.....	142
5.2.2.3.3 BaTiO ₃ Particle Array Fabrication and Characterization	144
5.2.2.3.4 Polymer/BaTiO ₃ Composite Film Fabrication and Characterization	147
5.2.2.4 Polymer/Metal.....	152
5.4 Conclusions and Future Outlook.....	153
5.5 References	155

List of Tables

Table 1.1 Selected applications that utilize controlled colloidal manipulation techniques	33
Table 2.1 Water contact angle data	53
Table 2.2 Results for unextracted PFPE samples	59
Table 2.3 Results for PFPE samples extracted in solkane	60
Table 2.4 Permeability of PFPE compared with PDMS.....	65
Table 3.1 Particle properties	78
Table 3.2 Zeta potential measurements of rod particles	88
Table 4.1 Saturation magnetization of B3 particles	113
Table 4.2 Composite particle polymerization experimental results	119
Table 4.3 Particle translational velocities for all particle sizes under a stationary magnetic field (no field) with varying solutions of H ₂ O ₂	122
Table 5.1 Summary of Ordered Composite Films	131
Table 5.2 Electrical characterization of PC/BaTiO ₃ and PVDF/BaTiO ₃ composite films ...	151

List of Figures

Figure 1.1. SEM and TEM images of different types of particles illustrating four of the major particle shape classes: Top row – Spherical and derivatives where (a) are PS latex spheres, (b) clusters of PS microspheres with triangular dipyramid structure, (c) PS ellipsoids and (d) PS disks. Second row – Polyhedra shapes where (e) are silver right bipyramids, (f) silver nanocubes, (g) silver octahedrons, and (h) truncated silver octahedrons. Third row – Branched and filamentous structures where (i) are CdSe/CdS nanotetrapods, (j) gold nanorods, (k) worm-like micellar structures of blends of different molecular weight PS-*b*-PEO copolymers, and (l) cross-linked PEG nanoworms. Fourth row – Lithographically-defined particle shapes where (m) rough side wall cylinders, (n) fenestrated hexagons, (o) arrow-shaped particles, and (p) open ring structure.8

Figure 1.2. Chemical anisotropy in different particle systems. Left panel shows bulk chemical anisotropy, and right panel shows surface chemical anisotropy, where (a) triphasic Au-CdSe-Au nanorods, (b) bi-colored particles with half containing carbon black and the other half containing titanium dioxide, (c) triphasic triangular particles fabricated with hydrodynamic focusing lithography, (d) blend particles of PS-*b*-PB and homopolymer PS, (e) superparamagnetic composite colloids with SiO₂-coated Fe₃O₄ core and a PS shell, (f) superparamagnetic composite colloids with SiO₂-coated Fe₃O₄ nanoparticle chains in PEG DA microspheres, (g) Janus particle formed using a glucose partial protecting layer, (h) gold patches deposited on polystyrene particles, (i) crosslinked EPTA particles with PS patches, (j) striped mixed SAM on gold nanoparticle, (k) end-functionalized PRINT cylindrical particles and (l) colloidosome Janus particles.11

Figure 1.3. Process utilizing templating and capillary forces. A) Illustration of the templating process; B, C) 2D lattices assembled from 1.75 μm PS beads in channels 10.0 and 10.5 μm, respectively; D) Double layered zig-zag chains formed by assembling PS beads in an array of channels (direction of flow indicated by arrow); E) Particle aggregate after annealing and release from the template shown in D.17

Figure 1.4. Example where fluidic assembly is used to assemble microdevices onto a plastic substrate. A) Overview of process; B) Closer detailed view; C) Collected freestanding single crystal silicon FETs; D) triangular FETs; E) cross-shaped FETs; F) Plastic substrate with empty binding sites; G) Substrate after assembly with transistor and resistor in place.21

Figure 1.5. Schematic illustration of the three electric field phenomena: A) Positively charged particle in a DC electric field, where the black arrow indicates the electrophoretic force and the red arrow indicates electroosmotic flow, and B) Particle in a non-uniform AC electric field, with an induced dipole indicated by small red arrow, experiencing a dielectric force either to a higher or lower field gradient (black arrows); dashed lines represent AC field.22

Figure 1.6. Examples of external field driven assemblies. A) Chaining of PS microspheres using dielectrophoresis. B) Staggered chain formation of metallodielectric Janus particles using dielectrophoresis. C) Chaining of magnetic composite particles in a magnetic field (arrow indicates field direction); particles exhibit directional preference in the field. D) 800

nm PS spheres (in water) assembled into a star configuration with dynamic optical trapping patterns.....	28
Figure 2.1. Schematic representation of the PRINT process. A) Roller is brought into contact with the particle precursor and the mold; B) Roller evenly distributes the precursor into cavities of mold. Excess liquid is pulled away by the high surface energy polymer sheet; C) Liquid is solidified in the mold to form particles; D) Particles are removed from the mold; E) Particles are collected in solution.	46
Figure 2.2. PFPE DMA	47
Figure 2.3. Contact interaction of a semi-sphere and planar surface, where the radius of deformation, a , is a function of the load, P	49
Figure 2.4. Reaction scheme for PFPE-DMA from the PFPE diol	52
Figure 2.5. Chain extension reaction to form 2× PFPE diol	52
Figure 2.6. Preparation of PFPE lenses	54
Figure 2.7. Optical side view image of the PFPE lens	55
Figure 2.8. Schematic representation of the JKR experimental apparatus	56
Figure 2.9. Plot of $a^{3/2}/R$ versus $P/a^{3/2}$ for 3×4K PFPE	58
Figure 2.10. Plot of $a^{3/2}/R$ versus $P/a^{3/2}$ for extracted 4K PFPE	58
Figure 2.11. Experimental set-up for capillary flow experiment	63
Figure 2.12. (a) Advancing liquid-air interface in dead-end PFPE micro-channels of different lengths and (b) Advancing liquid-air interface in dead-end PFPE and PDMS microchannels (25 μm × 38 μm × 6 mm)	64
Figure 3.1. Representative scanning electron micrograph and fluorescent images of (from left to right) 2.5 x 1 μm hexnut particles with 1 μm hole, 1.6 x 1.6 x 5 μm trapezoidal particles, 6.5 x 0.8 μm disk-shaped particles, 9.6 x 3.4 x 1 μm boomerang-shaped particles. Scale bars represent 2 μm	73
Figure 3.2. Illustration of the dielectrophoretic cell	74
Figure 3.3. Turbidity measurements on 5 mg/mL hexnut suspensions at three CTAB concentrations: 0.2 wt%, 1.0 wt% and 5.0 wt%	75
Figure 3.4. Turbidity curves for aqueous particle suspensions containing 1.0 wt% CTAB where A) 5 mg/mL hexnut suspension, B) 10 mg/mL rod suspension, C) 20 mg/mL disk suspension, and D) 10 mg/mL boomerang suspension.....	77
Figure 3.5. Representative fluorescence images of randomly dispersed (A, C, E, G) and electrically aligned (B, D, F, H) particles with a 5 μm scale bar. Particles shown were aligned at 40-50 V and 500 Hz	79
Figure 3.6. Evolution of chains as a function of time for rod particles, where each frame was taken every 2 seconds after application of the E field.	80

Figure 3.7. Fluorescence images of aligned particles with applied AC electric field. 5 μm scale bar. Particles shown were aligned in a 40-50 V field at 500 Hz.....	83
Figure 3.8. Low magnification fluorescence images of particle alignment in nonuniform AC electric field for (A) hexnut, (B) rod, (C) disk and (D) boomerang shaped particle suspensions	85
Figure 3.9. Fluorescence image of (A) hexnut and (B) rod shaped particles with applied AC electrical field on the electrode. 5 μm scale bar	86
Figure 3.10. PVP/PEG composite formed in DEP cell.....	87
Figure 3.11. SEM images of the rigid particle series (A) 2.8 \times 2.8 \times 0.9 μm (AR = 0.3), (B) 2.8 \times 2.8 \times 2.2 μm (AR = 0.8) and (C) 2.8 \times 2.8 \times 6.5 μm (AR = 2.3).....	88
Figure 3.12. Deformable CEA particles image (A) DIC image of dried drop of particles, and (B, C) SEM images of particles dried on a woven fiber membrane	89
Figure 3.13. Two types of microfluidic channels where (A) is a straight channel design and (B) is a microchannel design with patterned gaps	90
Figure 3.14. Third type of microfluidic device consisting of a cubic feature array	91
Figure 3.15. Particle speed as function of electric field strength for positively charged 2.8 \times 2.8 \times 0.9 μm particles suspended in (A) 1 wt% CTAB and (B) 1 wt% Pluronic.....	92
Figure 3.16. Particle speed as function of electric field strength for negatively charged particles suspended in 1 wt% Pluronic, where the particle sizes are (A) 2.8 \times 2.8 \times 2.2 μm (AR = 0.8) and (B) 2.8 \times 2.8 \times 6.5 μm (AR = 2.3)	92
Figure 3.17. Optical image of a patterned microchannel with particles moving towards the negative electrode (E field strength = 1.25 V/cm). Clogging was present near some of the gaps	93
Figure 3.18. Bright field images of particle crystallization occurring near the negative electrode (Field strength = 2.5 V/cm).....	93
Figure 3.19. DIC images of deformable particles in 5 μm array	94
Figure 4.1. TEM images of the magnetite samples used in the PRINT composite (A) microparticles and (B) nanoparticles	100
Figure 4.2. Schematic of an in-house magnetic stage for particle rotation and alignment experiments in water. The runner (gray) rotates in a circular fashion around the magnetic particle sample (red) in the center of the microscope stage (light blue). Magnets at opposite ends of the runner (orange) create a magnetic field across the particle sample that rotates with the runner.	104
Figure 4.3. Schematic of the microscope and magnet setup for micromotor experiments. The magnet was mounted on a motor and was suspended above the sample, slightly off-center from the path of the transmitted light.	106

Figure 4.4. SEM (A-C) and TEM (D-F) images of PRINT magneto-polymer nanoparticles on the harvesting layer and collected from solution, respectively. (A,D) are 80×2000 nm worm particles, (B,E) are 80×320 nm rice particles, and (C,F) are 200×200 nm cylindrical particles.....	107
Figure 4.5. Fluorescent micrograph of particles in the mold containing (A) 1, (B) 10, and (C) 50 wt% magnetite particles. Aggregates of magnetite are visible in the particles as dark spots in the green fluorescent polymer background.....	108
Figure 4.6. A schematic representation of the PRINT process where (A) is the PFPE mold (shown in green) and pre-particle solution (shown in red) containing randomly dispersed Fe_3O_4 , (B) shows the full mold placed in a magnetic field created by two permanent magnets and linear aggregates of Fe_3O_4 are formed prior to photopolymerization of the composite particle, and (C) ESEM image of harvested boomerang particles with linear aggregates of magnetite visible via the backscattered electron detector.....	109
Figure 4.7. Fluorescence microscopy images of four samples of $10 \mu\text{m}$ boomerang-shaped particles in the PFPE mold with (A) no linear Fe_3O_4 aggregates, (B) aggregates in the plane and parallel to one arm of the boomerang, (C) aggregates normal to the plane of the particle, and (D) aggregates in the plane at a 45° angle to the arms of the boomerang. Scale bar is $10 \mu\text{m}$	110
Figure 4.8. The number of magnetite chains observed in composite particles cured in a strong magnetic field as a function of the time held in the field prior to curing as well as the concentration of the magnetite nanoparticles within the composite resin	111
Figure 4.9. Magnetite nanoparticle chain length as a function of time, nanoparticle concentration and field strength.....	112
Figure 4.10. ESEM images of B3 particles ($2 \times 2 \times 5 \mu\text{m}$) with magnetite (A) randomly oriented, B3-R, (B) aligned along the long axis, B3-L, and (C) aligned along the short axis, B3-S.	112
Figure 4.11. Magnetization curves for B3 particles with dispersed magnetite and linear aggregates of magnetite aligned perpendicular and parallel to the length of the particles. All magnetic orientations exhibit very low remnant magnetization, as shown in the inset curves near 0T	113
Figure 4.12. Anisotropic surface functionalization of PRINT particles, where (A) is an ESEM image of Pt-capped B2 particles containing linear aggregates of magnetite, (B) is an SEM image of a single-capped B2 particle on a graphite surface indicating the location of an energy dispersive X-ray elemental line scan (magenta), and (C) the line scan results displaying the location of the iron (red) and platinum (teal) in the particle. The Y axis of the elemental line scan is signal intensity (kcps).....	114
Figure 4.13. Clockwise rotation of boomerang-shaped particles, with magnetite aligned along one arm, in rotating magnetic field.....	115
Figure 4.14. Clockwise rotation of boomerang-shaped particles, with magnetite aligned perpendicular to the plane of the particle, in rotating magnetic field.....	116

Figure 4.15. Fluorescence microscopy images of a dispersion of block-shaped B3 composite particles with different magnetite arrangements in the absence (A,C,E) and presence (B,D,F) of a magnetic field. (B) Particles without linear aggregates in an applied magnetic field formed disordered chains while (D) particles with linear aggregates parallel to the length of the composite particle formed somewhat organized chains stacking head-to-tail and (F) particles with linear aggregates perpendicular to the length of the composite particle formed somewhat organized chains stacking side-to-side respectively. Arrows indicate direction of applied magnetic field.....	118
Figure 4.16. Particle polymerization experiment using B3 composite particles: (A) particle chain length as a function time and magnetite chain orientation, and (B) the number of particles per chain as a function of time and magnetite chain orientation.....	119
Figure 4.17. Overlaid image showing the path of a magnetically-guided micromotor in 30 % hydrogen peroxide solution. The motor, which exhibits linear translational motion, turns when the magnetic field changes direction. The platinum end of the particle was chemically functionalized with a red dye for ease of visualization.....	121
Figure 4.18. Traces of B3 particles with random magnetic moments (orange) in a rotating magnetic field overlaid with particles with magnetic moments parallel to the long particle axis in 30% H ₂ O ₂ in a stationary (dotted) and rotating (solid) magnetic field.....	124
Figure 5.1. Simplified fabrication scheme for crosslinked PRINT composite films.....	133
Figure 5.2. (a-c) SEM images of film cross-sections and (d-f) top-view optical/fluorescence images of composite films. The examples are (a) a PEG/triacrylate resin composite film with 7 μm cylindrical triacrylate particles, (b) is an epoxy/triacrylate resin composite film with 7 μm cylindrical triacrylate particles, (c) is a PEG/triacrylate resin composite film with 200 nm cylindrical triacrylate particles, (d) is a PEG/triacrylate resin 2-layer composite film with 7 μm cylindrical triacrylate particles (rhodamine B dye used in particles for imaging), (e) is a PEG/PS 3-layer composite film with 7 μm cylindrical PS particles and (f) is a PEG/MDMO-PPV 2-layer composite film with 7 μm cylindrical MDMO-PPV particles.	134
Figure 5.3. Angled views of the 3-D confocal microscopy projection of a PEG/PVP 3-layer composite film with 10 wt% Paclitaxel in the 5 μm cubic PVP inclusions (fluorescein <i>o</i> -acrylate dye used in particles for imaging).....	135
Figure 5.4. TGA decomposition curves for pure PEG, pure PS and the ordered PEG/PS composite film	136
Figure 5.5. Dynamic Mechanical Analysis of an all-PEG composite where (a) shows the tan δ curves for pure 750 g/mol PEG-DMA, pure 550 g/mol PEG-DMA, a 4:1 blend of 750 g/mol PEG-DMA and 550 g/mol PEG-DMA and an ordered composite 4:1 750/550 g/mol PEG-DMA, and (b) is an SEM image of the ordered 4:1 750/550 g/mol PEG-DMA composite film cross-section containing 16 particle layers with an inset picture of the transparent film	138
Figure 5.6 Simplified fabrication scheme for thermoplastic PRINT composite films	139

Figure 5.7. (A) Simplified fabrication scheme for continuous thermoplastic PRINT composite films and (B) cleaved capillary tube with ordered composite PVDF/PEG composite film wrapped around it	140
Figure 5.8. SEM images of cross-sections of PVDF/PEG composite films where the $3 \times 3 \mu\text{m}$ PEG particles have increasing aspect ratio: (A) 0.25, (B) 0.5 and (C) 1	141
Figure 5.9. Confocal microscopy study of ordered PC/PEG bilayer composite films showing two different relative layer orientations where in (a) both particle layers are parallel and in (b) the particle layers are perpendicular. Scale bars represent $10 \mu\text{m}$	142
Figure 5.10. XRD spectrum for sol-gel derived BaTiO_3 powder.	143
Figure 5.11. FTIR Spectrum of BaTiO_3 xerogel and ceramic films	144
Figure 5.12. SEM images of BaTiO_3 embossed films fabricated from (A) a $200 \times 200 \text{ nm}$ template and (B) a $3 \mu\text{m}$ hexnut template.....	145
Figure 5.13. SEM images of scum-free BaTiO_3 cubic particles analyzed with Energy Dispersive Spectroscopy, where (A) shows line scans and (B) elemental mapping indicating the presence of Mg, Ba and Ti.	146
Figure 5.14. SEM images showing the shrinkage that occurs in the conversion of the BaTiO_3 xerogel (at left) to the polycrystalline ceramic (at right)	147
Figure 5.15. Ordered polymer/ceramic composite films showing (a) simple fabrication scheme with SEM images of examples of PVDF/ BaTiO_3 film cross-sections with (b) $400 \times 200 \text{ nm}$ cylinders, (c) $3 \times 0.5 \mu\text{m}$ cylindrical particles and (d) $3 \times 2.5 \mu\text{m}$ cylindrical particles, with Energy Dispersive Spectroscopy elemental mapping identifying the Ba and Ti from the ceramic particles and the F from the polymer.	148
Figure 5.16. TGA study of PC/ BaTiO_3 ordered composite films where (a) shows the decomposition curves for films with increasing number of particle layers and ESEM images of the composite film cross-sections with (b) 1, (c) 2, (d) 3, and (e) 6 particle layers. Scale bars represent $10 \mu\text{m}$	149
Figure 5.17. Schematic illustration of the breakdown testing apparatus	150
Figure 5.18. (A) SEM image crosslinked phosphate resin/ BaTiO_3 composite particles on a harvesting layer and (B) SEM image of a cross-section of a tri-phasic PVDF/crosslinked phosphate resin/ BaTiO_3 composite film	152
Figure 5.19. ESEM images of (a) top view harvesting layer with silver flakes on PC, (b) side view harvesting layer with silver flakes on PC and (c) PC/silver ordered composite film ...	153

List of Abbreviations and Symbols

°C	degrees Celcius
®	registered
γ	surface tension
%	percent
°	degrees
μm	micrometer
ϵ	dielectric constant (permittivity)
$\tan \delta$	dielectric loss tangent
μL	microliter
V_B	breakdown voltage
v	migration speed
μ	electrophoretic mobility
ζ	zeta potential
η	viscosity
2D	two dimensional
3D	three dimensional
AC	alternating current
AEM	2,2'-aminoethyl methacrylate
ar	aspect ratio
ATR FTIR	attenuated total reflectance fourier transform infrared spectroscopy
BaTiO_3	barium titanate
C	capacitance

CEA	2,2'-carboxyethyl acrylate
CdS	cadmium sulfide
CdSe	cadmium selenide
cm	centimeter
CTAB	cetyltrimethylammonium bromide
DC	direct current
DEAP	2,2'-diethoxyacetophenone
DEP	dielectrophoresis
DIC	differential interference contrast
DMF	dimethyl formamide
DMTA	dynamic mechanical thermal analysis
DMSO	dimethyl sulfoxide
DSC	differential scanning calorimetry
E	electric field
EDS	energy dispersive spectroscopy
emu	electromagnetic units
EPTA	ethoxylated trimethylolpropane triacrylate
ER	electrorheological
ESEM	environmental scanning electron microscopy
et al.	and others
etc.	et cetera
Fe ₃ O ₄	iron oxide (magnetite)
FET	field effect transistor

g	gram
g/mol	gram/mole
HCl	hydrochloric acid
HCPK	1-hydroxycyclohexyl phenyl ketone
H ₂ O ₂	hydrogen peroxide
H ₂ SO ₄	sulfuric acid
Hz	Hertz
JKR	Johnson, Kendall, Roberts
kcps	kilocounts per second
kGauss	kilogauss
kHz	kilohertz
kV	kilovolt
LCR	inductance capacitance resistance
MDMO-PPV	poly[2-methoxy-5-(3',7'-dimethyloctyloxy)-1,4-phenylenevinylene]
MEK	methylethylketone
MEMS	microelectromechanical systems
mg	milligram
MgO	magnesium oxide
MHz	megahertz
MIMIC	micromolding in capillaries
mL	milliliter
mm	millimeter
M _n	number average molecular weight

mNm ⁻¹	milliNewton per meter
MPa	megapascal
MR	magnetorheological
M _s	saturation magnetization
N ₂	nitrogen
nm	nanometer
O ₂	oxygen
PC	polycarbonate
PDI	polydispersity index
PDMS	polydimethylsiloxane
PEG	poly(ethylene glycol)
PEG-DMA	poly(ethylene glycol) dimethacrylate
PEG-TA	poly(ethylene glycol) triacrylate
PEO	poly(ethylene oxide)
PET	poly(ethylene terephthalate)
PFPE	perfluoropolyether
PFPE-DMA	perfluoropolyether dimethacrylate
PMMA	poly(methyl methacrylate)
Ppy	polypyrrole
PRINT	Particle Replication in Non-wetting Templates
PS	polystyrene
PS-b-PB	polystyrene-block-polybutadiene
psi	pounds per square inch

PVDF	poly(vinylidene fluoride)
PVOH	poly(vinyl alcohol)
PVP	polyvinylpyrrolidone
RFID	radio frequency identification
SAM	self-assembled monolayer
SEM	scanning electron microscopy
SQUID	superconducting quantum interference device
sec	second
T	tesla
TEM	transmission electron microscopy
T _g	glass transition temperature
TGA	thermogravimetric analysis
TMPTA	trimethylolpropane triacrylate
UV	ultraviolet
V	volt
wt	weight
XRD	x-ray diffraction
XPS	x-ray photoelectron spectroscopy

Chapter 1

Introduction to the Manipulation of Colloids

1.1 Overview

For many years, the study of colloidal systems has proved to be a very valuable and fundamental endeavor, both academically and commercially. A subfield of colloid science of growing importance is the manipulation of colloids to create useful structures or to perform some form of work. This has been the focus of much research over the years and interest is continuing to grow because the synthesis of colloidal particles has advanced to the stage where particles are now engineered with a very high degree of control, suggesting a higher probability that these colloidal systems can be used in the ever-increasing number of technologically advanced applications that demand nanoscale structuring or nanoscale control. Some of the current advanced applications include magnetorheological and electrorheological fluids in the automotive industry (brakes, suspension etc.),¹ particle based display technologies^{2,3} and rheological modifiers in coatings.⁴

Arguably, one of the most important characteristics of colloidal particles is the particle shape. A large body of work in this field has focused on spherical particles because of the availability of monodisperse samples with uniform chemical and physical properties. Only recently have publications begun to accumulate that explore non-spherical particle shapes in colloidal systems. A second major consideration of colloidal systems is composition, which in turn affects particle charge, as well as mechanical, magnetic and electrical properties. Particle composition can be homogeneous, randomly heterogeneous or segmented, as is the case for core-shell particles or Janus particles. Another strategy that introduces compositional complexity is through modification of the particle surface. Again this can be done homogeneously over the entire particle surface or it can be anisotropic or patchy, a term coined by Glotzer *et al.*⁵ These properties provide avenues through which

particles can be manipulated. In order for processes to be efficient however, uniformity is key. Broad distributions in the particle properties prevent global responses, as well as introduce defects into the system.

Factors that affect which tool or tools are chosen to manipulate colloidal systems include (1) effectiveness: whether all or only a percentage of the particles respond in the expected fashion; (2) time scale: if the response is instantaneous or requires a long time period; (3) scale: single or few particle manipulations versus large-scale processes; (4) required resources: whether the materials and equipment are expensive, complex and sensitive versus low-cost and simple; (5) property matching: if the particle properties are suitable, for example, magnetic manipulation cannot be used with a particle system that has no magnetic properties; and (6) target application: high value versus commodity.

It is not surprising that even though there is a great deal of research devoted to synthesizing and fabricating novel colloids and nanoparticles, there has been a shift in research emphasis from the fabrication/synthesis to the application of these building blocks to performing useful work individually or collectively, or being organized into larger more complex entities capable of functioning as an integrated whole. This begets the question: how then do we in a systematic and controlled manner manipulate particles? And more importantly, can we then use this knowledge to attack grand scientific challenges such as advancing solar energy and energy storage technologies, curing cancer, surpassing current standards in electronics, and exploring fundamental scientific theories. At present, there are many different processes used to manipulate colloids, and they can be broadly organized according to the degree of external force required. There are those processes that proceed almost independently of external contribution and which depend solely on the particle and

suspending medium properties; these include many self-assembly and catalytic processes. Then there are those processes that, in addition to particle and medium properties, are strongly dependent on external forces such as magnetic, electric and optical fields. In this chapter, particle fabrication and the processes used for the manipulation of colloids are reviewed.

1.2 Particle Fabrication Methodologies

There is a vast body of literature on synthesizing colloidal particles with tailored properties, where the fabrications of an impressive range of exotically-shaped particles with geometric and chemical asymmetries have been demonstrated. The caveat, however, is that there are varying degrees to the efficiencies, scalabilities and versatilities of the different approaches where some have greater potential as broad platform technologies than others. Regardless, there is a great deal of knowledge and methodologies to draw from in synthesizing and fabricating tailored colloidal micro- and nanoparticles. Furthermore, everyday new and more creative approaches are being developed. In this section, colloidal micro- and nanoparticle synthesis is overviewed briefly with the intent of identifying methods where information is programmed into the particle shape and chemistry for manipulation. This discussion is not meant to be exhaustive but illustrative of the breadth of complexity available. There are numerous published reviews that explore particle synthesis and fabrication in greater detail.⁶⁻⁸ In general, particles can be synthesized via bottom-up or top-down processes. Bottom-up methods start with molecular precursors and build up to the particle, whereas top-down processes start with a pre-existing framework that defines the

desired particle shape and size and then the material is introduced to fabricate the particle. The particle size for this discussion ranges from nanoparticles (1 – 100 nm) to intermediate colloidal particles (100 nm – 10 μ m) to mesoscale particles (10 μ m – 1 mm). This section will be divided into the two major design parameters for controlling and manipulating particles: shape and chemical anisotropy

1.2.1 Shape Anisotropy

Spherical particles have been the foundation of colloidal science for numerous years as it is possible to synthesize uniform monodisperse spherical particles with different compositions, typically through emulsion processes for polymer latexes and controlled precipitation for inorganic oxides.⁹ More recent discoveries in particle synthesis and fabrication are slowly shifting the field from the more prevalent spherical particle to other particle shapes.

Figure 1.1 summarizes some of the major particle shape classes that have been generated to date. Bottom-up syntheses often generate spherical particles as that morphology is the most favorable to adopt to minimize interfacial energy.⁹ Researchers, however, have developed novel methods for deriving geometrical complexity from the spherical particle. One simple approach is the controlled aggregation of spherical particles to form new particle species with increasing polyvalency. Manoharan *et al.* fused spherical particles together to form new particle species with nontrivial symmetries (Figure 1.1b).¹⁰ Xia and coworkers also fused spherical particles to create new particles but instead of an emulsion process, they used templating to define the size and geometry of the new particle shape.^{11, 12} Mechanical

deformation of thermoplastic spherical particles is another route researchers have taken to introduce geometrical anisotropy from spherical systems.¹³⁻¹⁵ Thermoplastic spherical particles, such as polystyrene (PS) or poly(methyl methacrylate) (PMMA), are dispersed in a deformable matrix, such as poly(vinyl alcohol). The film is stretched creating voids around the dispersed particles. Either heat or solvent is used to fill the voids with the particle composition and then the particles are resolidified. The particles are collected after dissolving the poly(vinyl alcohol) matrix. In this manner, Champion *et al.* fabricated disks, rods, worms, ellipsoids and cylindrical particles from polystyrene nanospheres (Figure 1.1c,d).¹³

Multi-sided particles with defined, straight edges have also been synthesized but these polyhedra particles have been, for the most part, inorganic in composition. Numerous factors influence the inorganic particle morphologies when synthesized via solution phase, such as anisotropic interactions with capping agents, impurities or solvent, defects present during nucleation, and reaction temperature.⁷ Xia *et al.* reviewed many of the metal nanoparticles morphologies that have been synthesized, which include numerous polyhedra structures, such as prisms, cubes, tetrahedra, octahedra and icosahedra, as well as triangular and hexagonal plate-like structures (Figure 1.1e-h).⁷ Hollow structures are also possible, for example, by galvanic replacement reactions.^{16, 17}

One interesting particle structure is that of branched nanoparticles synthesized through the seeded growth of nanocrystals. For example, Talapin *et al.* synthesized branched cadmium selenide/cadmium sulfide (CdSe/CdS) nanotetrapods (Figure 1.1i).¹⁸ High aspect ratio particles such as rods and fibers can also be readily synthesized in a range of compositions. Metal nanorods, nanowires and nanobelts have been synthesized by varying

the reagent concentration in solution processes.¹⁹⁻²¹ Hard templating, using anodized alumina (AAO) or track-etched polymer membranes, is an attractive and very popular route to the synthesis of high aspect ratio rod-shaped particles.²²⁻²⁴ For example, anodized alumina (AAO) templates have been used along with electrodeposition to fabricate metallic, semiconductor and polymeric nanowires, nanotubes and nanorods.²²⁻²⁴ For organic particles, self-assembled block copolymer systems can be designed to form stable filamentous micelles (Figure 1.1k).^{25, 26}

Another class of particle shapes, referred to as lithographically-defined,⁸ has emerged due to the development of top-down particle fabrication processes, such as stop-flow lithography,²⁷ photolithography²⁸ and Particle Replication in Non-wetting Templates (PRINT[®]),²⁹ where the particle shape (at least the 2D cross-section) can be virtually any shape imaginable, once it can be drawn using computer-aided design (CAD) software. These shapes generally have at least 2 coplanar faces, but there are opportunities to overcome this limitation with advances in inclined UV lithography,³⁰ or by combining angled deposition with photolithography. In addition to many of the shapes described for the other particle fabrication approaches, unusual shapes, including arrows, stars, letters, rings, torroids, fenestrated hexagons, crosses and ball and stick configurations can be easily fabricated with lithography in a range of sizes and compositions (Figure 1.1m-p).^{6, 28, 31, 32}

One component of shape anisotropy that may occasionally be overlooked is that of surface roughness. The texture of the particle surface can be a significant particle parameter that will affect its ability to assemble. There are different ways to modify the roughness of the particle surface. A common bottom-up approach to surface roughness is through the use of Pickering emulsions where small particles adsorb to the surface of emulsion droplets,

resulting in particles coated with smaller particles.³³ In another example, Badaire *et al.* modified the etching conditions to change the surface roughness of photolithographically-fabricated particles (Figure 1.1m).^{34, 35}

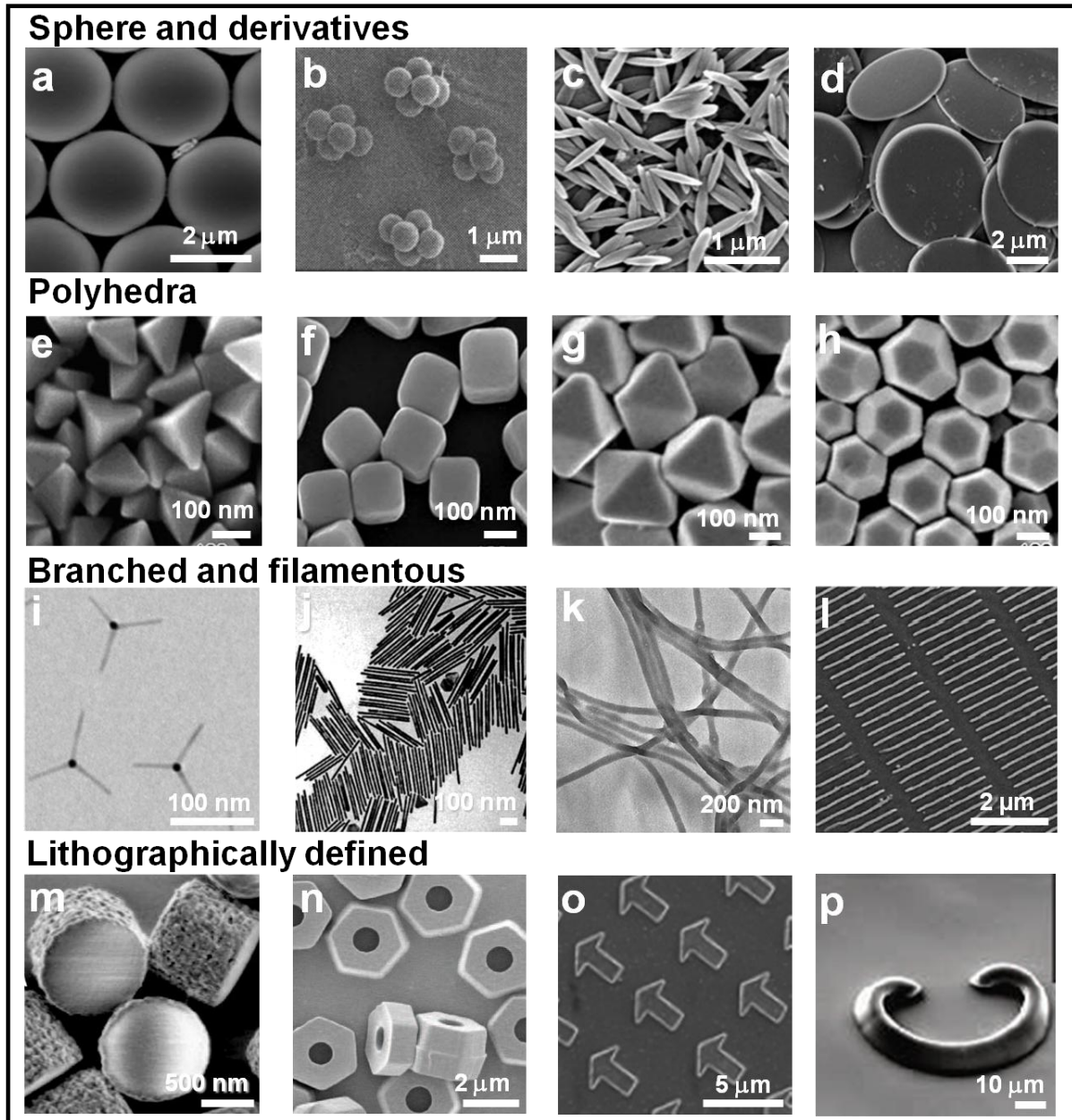


Figure 1.1. SEM and TEM images of different types of particles illustrating four of the major particle shape classes: Top row – Spherical and derivatives where (a) are PS latex spheres,¹³ (b) clusters of PS microspheres with triangular dipyrnid structure,¹⁰ (c) PS

ellipsoids¹³ and (d) PS disks.¹³ Second row – Polyhedra shapes where (e) are silver right bipyramids,⁷ (f) silver nanocubes,⁷ (g) silver octahedrons,⁷ and (h) truncated silver octahedrons.⁷ Third row – Branched and filamentous structures where (i) are CdSe/CdS nanotetrapods,¹⁸ (j) gold nanorods,¹⁹ (k) worm-like micellar structures of blends of different molecular weight PS-*b*-PEO copolymers,²⁶ and (l) cross-linked PEG nanoworms.³⁶ Fourth row – Lithographically-defined particle shapes where (m) rough side wall cylinders,³⁴ (n) fenestrated hexagons,³⁷ (o) arrow-shaped particles,³² and (p) open ring structure.³⁸

1.2.2 Chemical Anisotropy

Like shape anisotropy, chemical anisotropy is of fundamental importance when considering the manipulation of colloids, especially for mobility. Figure 1.2 illustrates the range of chemical anisotropies in different particle systems. The particle can be segmented, with distinct internal spatially resolved compartments of differing compositions, or have surface anisotropy. Janus (and multi-segmented) particles can be synthesized by the sequential addition of material to templates, as is the case for the fabrication of bi- and multi-metallic nanorods in AAO templates (Figure 1.2a).^{23, 39} Similarly, segmented organic particles have been fabricated using the PRINT process.⁴⁰ Using microfluidic approaches, co-flowing different precursors results in multicomponent particles (Figure 1.2b,c).²⁷ Kim and coworkers used a seeded polymerization technique in which monomer-swollen particles were polymerized. During the polymerization, a phase separation occurred, resulting in two-phase dumbbell-shaped particles; the resulting particles exhibited both chemical and shape anisotropy.⁴¹ Internal chemical anisotropy was also achieved with particles fabricated from block copolymers and polymer blends.⁴²⁻⁴⁶ For example, particles synthesized from polystyrene-*block*-poly(butadiene) (PS-*b*-PB) blended with polystyrene homopolymer using an emulsion process exhibited very unique internal morphologies (Figure 1.2d). These

morphologies could be tuned by adjusting the droplet size and weight fraction of the PS homopolymer.⁴⁴ Loading and ordering of magnetic material within particles is another approach towards chemical anisotropy. The composite particles can have a random internal structure, a core-shell structure (Figure 1.2e),⁴⁷ an aligned chain structure (Figure 1.2f),⁴⁸ or the composite particles can be Janus particles, with the magnetic nanoparticles concentrated on one side.⁴⁹⁻⁵²

One common method for chemically modifying the particle surface is through the use of a protecting layer to conceal one section of the particles, followed by modification of the exposed surface of the particles. For example, Cayre *et al.* used a technique where a monolayer of polystyrene spheres were deposited on a substrate. A glucose film was used to protect part of the particle surfaces, leaving the top surfaces exposed. The exposed surfaces were modified with an oppositely charged species by microcontact printing (Figure 1.2g).⁵³⁵⁴ Similarly, Cui *et al.* used a PDMS layer to partially protect the surfaces of a layer of spheres and the exposed surfaces were modified with silver via electroless deposition.⁵⁵ Pawar and Kretzschmar did not use a partially protecting layer, but instead prepared a 2D close packed layer of spheres, then used glancing angle vapor deposition to selectively modify small regions of the particle surface (Figure 1.2h).⁵⁶ Pickering emulsions are another approach to modifying the surface texture of particles. Kim *et al.* used polystyrene latex particles to stabilize an oil-in-water emulsion, where the oil phase was photocurable ethoxylated trimethylolpropane triacrylate (EPTA). EPTA-PS composite microparticles with coordinated patches resulted (Figure 1.2i).⁵⁷ In yet another approach, Jackson *et al.* showed that a self-assembled monolayer (SAM) of mixed ligands organize into striped domains on the surface of gold and silver nanoparticles due to the curvature of the particles (Figure

1.2j).⁵⁸ Recently, Percec *et al.* presented an extensive systematic study on self-assembled particle structures (dendrimerosomes) from a library of amphiphilic Janus dendrimers.⁵⁹ In addition to particle shape control, they demonstrated great control of the outer/internal chemical environment of the dendrimerosomes.

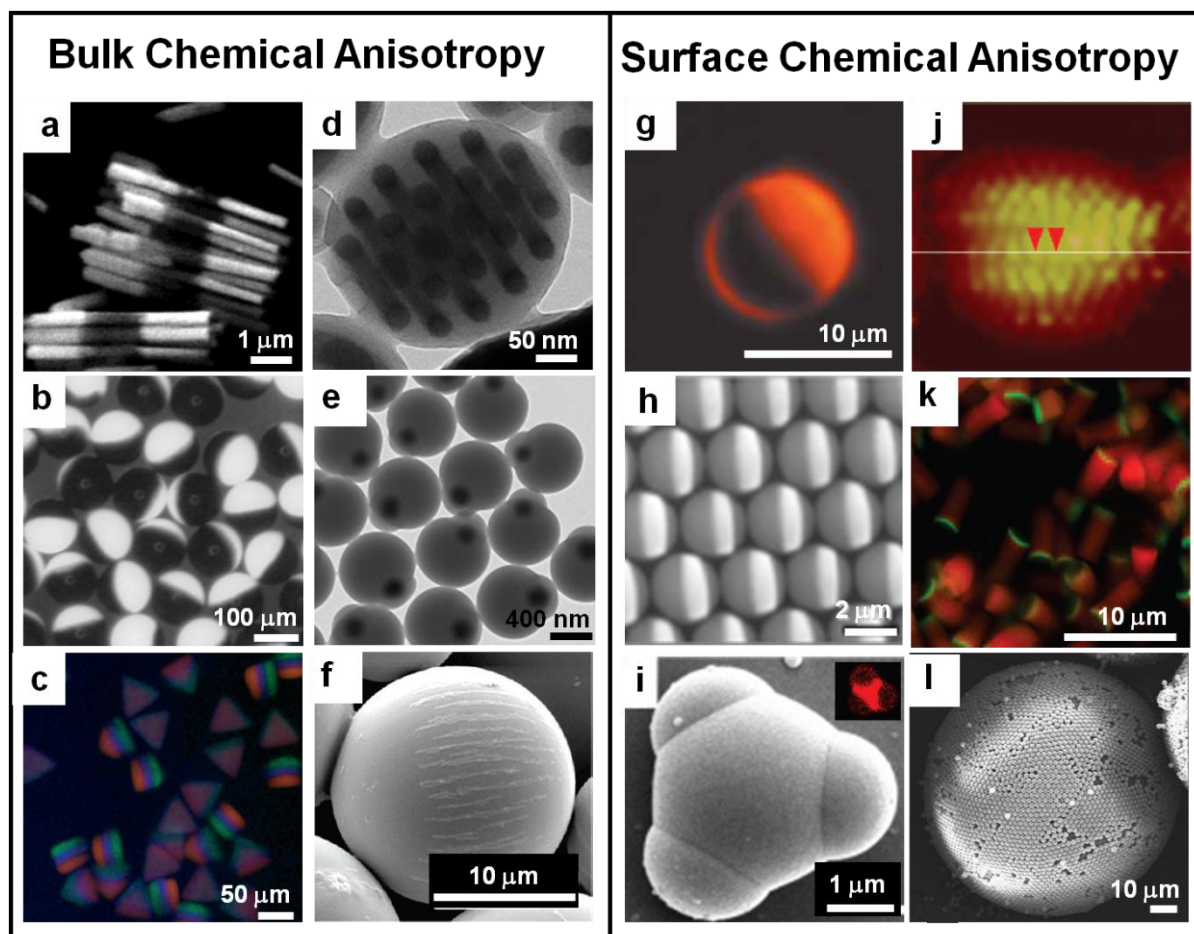


Figure 1.2. Chemical anisotropy in different particle systems. Left panel shows bulk chemical anisotropy, and right panel shows surface chemical anisotropy, where (a) triphasic Au-CdSe-Au nanorods,⁶⁰ (b) bi-colored particles with half containing carbon black and the other half containing titanium dioxide,⁶¹ (c) triphasic triangular particles fabricated with hydrodynamic focusing lithography,⁶² (d) blend particles of PS-*b*-PB and homopolymer PS,⁴⁴ (e) superparamagnetic composite colloids with SiO₂-coated Fe₃O₄ core and a PS shell,⁵⁰ (f) superparamagnetic composite colloids with SiO₂-coated Fe₃O₄ nanoparticle chains in PEG

DA microspheres,⁴⁸ (g) Janus particle formed using a glucose partial protecting layer,⁵⁴ (h) gold patches deposited on polystyrene particles,⁵⁶ (i) crosslinked EPTA particles with PS patches,⁵⁷ (j) striped mixed SAM on gold nanoparticle,⁵⁸ (k) end-functionalized PRINT cylindrical particles,²⁹ and (l) colloidosome Janus particles.⁶³

1.3 Autonomous Particle Manipulation

1.3.1 Controlled aggregation

It is possible for three-dimensional (3D) colloidal crystals to form spontaneously depending on environmental conditions. In the simplest case of a system of hard spheres, entropic considerations predict that crystals will form when the particle volume fraction is increased.⁶⁴ Generating colloidal crystals, even if predicted from phase diagrams, are not always possible as the systems are generally very sensitive to external conditions, and very often get trapped in gelled or glassy states.⁶⁵ Furthermore, crystallizing colloidal particles in this manner is extremely slow so the applicability is limited. A faster alternative is to use gravitational sedimentation, where the spherical particles are concentrated and crystallized. This can be further accelerated with centrifugation, filtration and other methods.⁶⁶ Many researchers use convective assembly approaches for fabricating 2D crystals. Entropic ordering favors the formation of ordered structures from monodisperse particles at sufficiently high volume fractions. During evaporation of surrounding solvent, the particle volume fraction increases until they crystallize at a critical volume fraction determined by the shape of the particles. Complete evaporation of the solvent fixes the particles in the close-packed geometry.⁶⁷

The entropically-driven assembly and crystallization of particles can occur through depletion interactions. In a system of suspended particles in a solvent or other smaller particles, attraction occurs when the larger particles get close together so that no smaller particles (or solvent or solute molecules) can fit between them, and the particles experience a net osmotic pressure acting to push them together. It is possible to tune the purely entropic attractive interaction by adding solutes of varying sizes and concentrations to the system. This depletion effect has been used to assemble monodisperse particles into chains and 2D crystals.^{28, 34, 68, 69} Moreover, this approach can be used with anisotropically shaped particles, where shape effects need to be considered. Hernandez and Mason showed that micron-sized crosses formed long columns with a high degree of arm alignment. Side by side arm interlocking of the crosses was also observed. When crosses and donuts were suspended together, lock and key insertion of the arm of the cross into the fenestration of the donut was observed.²⁸ Researchers have also studied the effect of particle surface roughness on this entropically-driven assembly.^{34, 69} Zhao and Mason demonstrated that depletion interactions between hexagonal platelets could be suppressed if the height asperities on the surface of the particles exceeded the size of the depletion agent. They designed their particles to either form long columnar aggregates or a dimer phase depending on anisotropic surface roughness.⁶⁹ Similarly, Badaire *et al.* demonstrated that they could induce cylindrical particles to preferentially form linear end-to end aggregates where the particles' flat smooth ends came into contact, as opposed to 2D crystals, where the particles would assemble with their rounded rougher surfaces interacting side by side. In this way, the shape and roughness of the particles defined the assemblies which formed.³⁴

Beyond entropic forces, the use of attractive forces is another tool that can be used in assembly. Introducing ionic interactions to the system of hard spheres can result in the formation of 3D colloidal crystals as demonstrated by Leunissen *et al.*, where two PMMA particle populations with opposite charges were allowed to interact and crystallize. After 35 hours, they observed the formation of crystallites, which continued to grow to form CsCl-type crystals (body-centered cubic lattice).⁷⁰ Again, crystallization processes such as these are very slow, so other approaches that use attractive forces are more appealing. The layer-by-layer technique is one such popular approach for assembling colloidal systems, usually for nanocomposite films.⁷¹ For example, alternating layers of polyelectrolyte and particles with opposite charges can form a dense composite film, with well-controlled thickness. Podsiadlo *et al.* used a dip-coating process to assemble alternating layers of poly(vinyl alcohol) and montmorillonite clay particles, resulting in a well-ordered nanocomposite film with exceptional mechanical properties.⁷²

In the examples provided thus far, the liquid (typically water) was isotropic. Introducing anisotropy to the solvent is another method for controlling particle assemblies. There has been research into the use of anisotropic liquids, such as liquid crystals, to guide the assembly and movement of particles. Liquid crystals can be aligned by patterning (for example, rubbing) a substrate, which in turn affects rotation, motility and assembly of particles.⁷³⁻⁷⁸ Lapointe *et al.* combined the effects of an anisotropic liquid with anisotropically shaped particles. They observed that altering the particle shapes led to significant changes in the forces experienced by the particles, and as a result, the colloidal assemblies that formed in a nematic liquid crystal.⁷⁴

Capillary forces are another important consideration for the assembly of particles. It has long been established that colloidal particles will assemble at liquid-liquid and liquid-gas interfaces, functioning as surfactants to stabilize foams and emulsions.⁷⁹ When there is anisotropy with respect to chemistry, another level of control is achieved in controlling particle assemblies at interfaces.⁸⁰⁻⁸⁴ Bowden *et al.* fabricated polydimethylsiloxane (PDMS) millimeter sized objects with hydrophilic and hydrophobic surfaces that floated at the interface of a water/perfluorodecalin 2-phase solvent system. With gentle mixing, a range of crystalline assemblies formed to minimize the interfacial free energy of the system by eliminating the curved menisci at the hydrophobic particle surfaces.^{80, 82} In another example, Dendukuri *et al.* fabricated amphiphilic wedge-shaped microparticles, and described their assembly in different solvent systems. The amphiphilic particles were found to form micelles in water, as well as orient themselves at the interface of oil-in-water and water-in-oil emulsions.⁸⁵ Similarly, Kim *et al.* used dumbbell-shaped amphiphilic particles as “colloid surfactants” to stabilize hexadecane-water emulsions. They found that the colloidal surfactants stabilized both spherical and non-spherical droplets because once the particles jammed at the liquid-liquid interface, the droplets were unable to relax to the spherical shape by expelling particles, so the droplets maintained their ellipsoidal or cylindrical shapes. Their study underscored the major difference between colloidal surfactants and molecular surfactants as molecular surfactants are unable to jam at the interface because of shorter relaxation times and dynamic exchange between adsorbed and freely diffusing species in the continuous phase.⁸³

Templates are regular features in the environment that guide the assembly process, and they can be used with the different self assembly approaches, such as sedimentation and

convective assembly, to encourage crystallization.^{86, 87} There are different types of templates that can be used, but they can be broadly classified into two main groups: physical and chemical. Physical templates are substrates where the surface has a physical pattern on it, with defined features and dimensions that may be, for example, etched into the substrate.^{11, 12,}⁸⁸ van Blaaderen *et al.* showed that the slow sedimentation of spherical silica particles (diameter ~ 500 nm) onto a polymer substrate patterned with 500 nm holes on a square lattice was able to direct large scale crystallization and allowed for the tailoring of lattice properties.⁸⁷ Xia *et al.* used lithographically etched holes and channels to assemble microspheres into different one and two dimensional assemblies (Figure 1.3).¹² Chemical templates are substrates where, for example, the pattern is defined by self-assembled monolayers (SAMs),⁸⁹⁻⁹² that have been deposited using processes such as dip-pen lithography⁹³ or micro-contact printing.⁹⁴ Rao *et al.* used a chemically patterned substrate with two distinct surface regions, one polar and the other nonpolar, to assemble single-walled carbon nanotubes.⁹⁰ In another example, a template with negatively and positively charged regions was fabricated by microcontact printing charged SAMs onto a substrate. Negatively charged gold stars were assembled onto the positively charged regions of the substrate by electrostatic interactions.⁹² Another method for patterning charged regions on a substrate was demonstrated by Jacobs and Whitesides, where a charged template was patterned by the injection of charge into an electret surface.⁹⁵

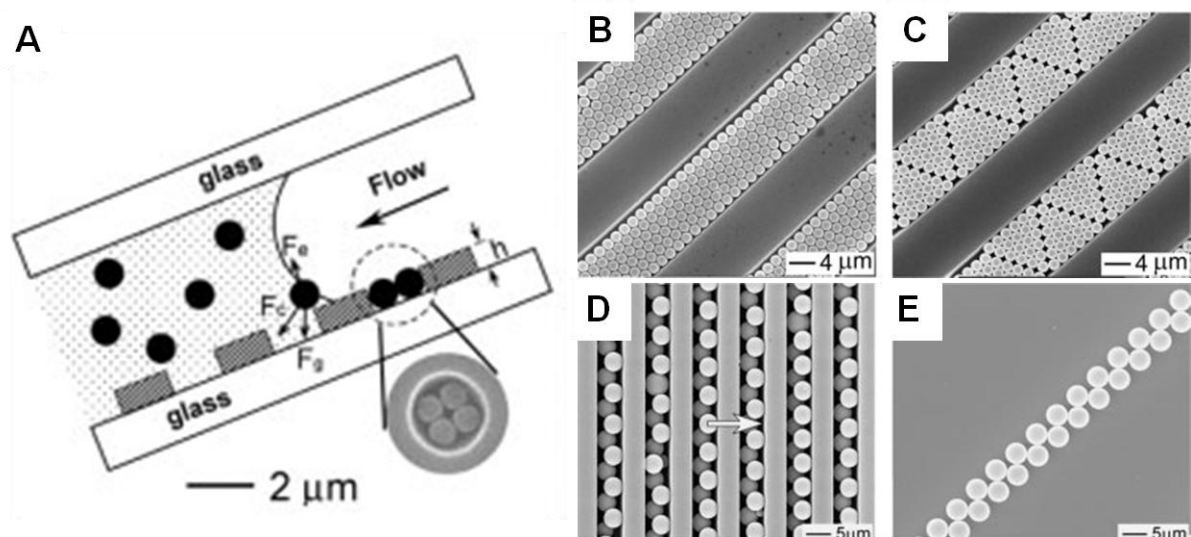


Figure 1.3. Process utilizing templating and capillary forces. A) Illustration of the templating process; B, C) 2D lattices assembled from 1.75 μm PS beads in channels 10.0 and 10.5 μm , respectively; D) Double layered zig-zag chains formed by assembling PS beads in an array of channels (direction of flow indicated by arrow); E) Particles aggregate after annealing and are released from the template shown in D.¹²

1.3.2 Catalytic Motion

The critical component to propulsive nano- and micro-systems is the asymmetric placement of catalyst on the body of the particle and the presence of a suitable reagent in the environment to result in the non-uniform consumption of the reagent and distribution of the reaction products leading to motion. One of the common propulsive catalyst systems in the literature is that of platinum, with hydrogen peroxide (H_2O_2) as the substrate. In the presence of platinum, H_2O_2 decomposes to form water and oxygen. The actual mechanism for motion varies depending on the particle composition. Howse *et al.* studied the mobility of polystyrene spheres (diameter 1.62 μm) with platinum coated on one half. They found that at short times, the particles move in a directed manner away from the platinum side of the

particle with velocities dependent on the concentration of H_2O_2 . They attributed the motion to a process of self-diffusiophoresis as more products are generated than reactants are available, setting up an asymmetric distribution of reaction products that propels the particles.

Others, however, have proposed a different mechanism. For a very similar system of silica spheres half-coated with platinum, another mechanism was proposed - that of bubble propulsion. It was suggested that the detachment of oxygen bubbles provides the driving force for the particles.⁹⁶ One micromotor system that clearly makes use of the bubble propulsion mechanism was developed by Sovolev *et al.* Their nanomotor consists of a microtube composed of a platinum inner layer, followed by gold (for adhesion), then iron (for magnetic control) and titanium. The researchers observed speeds as great as 2 mm/s which was equivalent to 50 body lengths per second.⁹⁷

Mallouk and Sen have led the field in studying the propulsion of bi- and trimetallic nanorods, using the platinum/ H_2O_2 catalytic system.⁹⁸ For example, platinum/gold (PtAu) rods (2 μm long, 370 nm wide) were found to move at speeds of approximately 8 $\mu\text{m/s}$ in 3.3% aqueous H_2O_2 , where the direction of motion was in the direction of the platinum half of the particles. The direction of motion was opposite to the platinum/non-metal Janus particles used in the previous examples, indicating that a very different mechanism was occurring in the PtAu case. Sen *et al.* defined this motion as self-electrophoresis, where protons are generated on the platinum end and consumed on the gold end, thereby generating an ion flux that induces particle motion.⁹⁸ Specifically, the pair of electrochemical reactions at the two metals creates an electric field near the particle surface (due to electron transfer) that moves the solvent via electroosmosis. This idea of self-electrophoresis is in direct

contrast to motion due to bubble propulsion or diffusiophoresis, but it requires at least a bi-metallic structure. The Wang group has optimized these systems to move faster.⁹⁹ In particular, Laocharoensuk and coworkers introduced carbon nanotubes (CNTs) to the platinum segment of the particle, and hydrazine to the hydrogen peroxide solution to accelerate the particle motion. With CNT addition, the average speed increased from 7.2 $\mu\text{m/s}$ to 51.0 $\mu\text{m/s}$. The speed was increased further to 94 $\mu\text{m/s}$ with hydrazine addition.⁹⁹ In addition to translation, the particles can be fabricated to rotate where the key design change is the location of the catalyst and shape of the particle.¹⁰⁰⁻¹⁰³

One interesting example of catalytic propulsion where inspiration is taken from nature to propel synthetic particles is through the use of actin polymerization, which is an essential process in cell motility.^{104, 105} Cameron *et al.* applied the concept of actin polymerization to the propulsion of synthetic particles.¹⁰⁴ They made use of the fact that *Listeria monocytogenes*, a gram positive intercellular bacterial pathogen that moves rapidly through host cells or cytoplasm extract, is propelled by actin polymerization. The moving bacteria are associated with an actin-rich structure that looks like the tail of a comet. The actin filaments remain fixed in space as the bacterium moves, and it is suspected that filament elongation provides the force necessary to propel the bacterium through the cytoplasm. The researchers tested this propulsion mechanism with synthetic polystyrene beads coated with the bacterial protein, ActA, which is responsible for the local catalytic polymerization of actin filaments. They found that for beads smaller than 500 nm uniformly coated with ActA, unidirectional motion resulted as the actin cytoskeleton that was generated spontaneously self-organize into a polar structure which generated a unidirectional force. Interestingly for larger beads, they found that motion was initiated only if the ActA protein

was asymmetrically coated on the sphere surface, similar to the manner in which the relatively large *L. monocytogenes* requires a polar distribution of ActA on its surface to move.

1.3.3 Fluidic Assembly

Fluidic assembly methods have been finding a great deal of interest among the micro/nanoelectromechanical systems (MEMS/NEMS) community. Mastrangeli *et al.* reviewed numerous processes that use the idea of fluidic self-assembly with shape matching.¹⁰⁶ In this process, both components (sizes ranging from mm to μm) and substrates are processed with complementary geometries. The components are dispersed in an inert carrier fluid across the substrate, and allowed to bind to complementary receptor sites. Components that do not bind are recycled for other passes. For example, Stauth and Parviz showed that single-crystal silicon field-effect transistors (FETs) and diffusion resistors could be fabricated onto flexible plastic substrates using fluidic assembly (Figure 1.4).¹⁰⁷ Separate from self-assembled systems, fluidic methods of assembling components, such as railed microfluidics, hold promise in the fabrication of complex structures. Park *et al.* developed a complex railed microfluidic system that is capable of sorting, flipping and assembling prefabricated disordered microstructures.¹⁰⁸

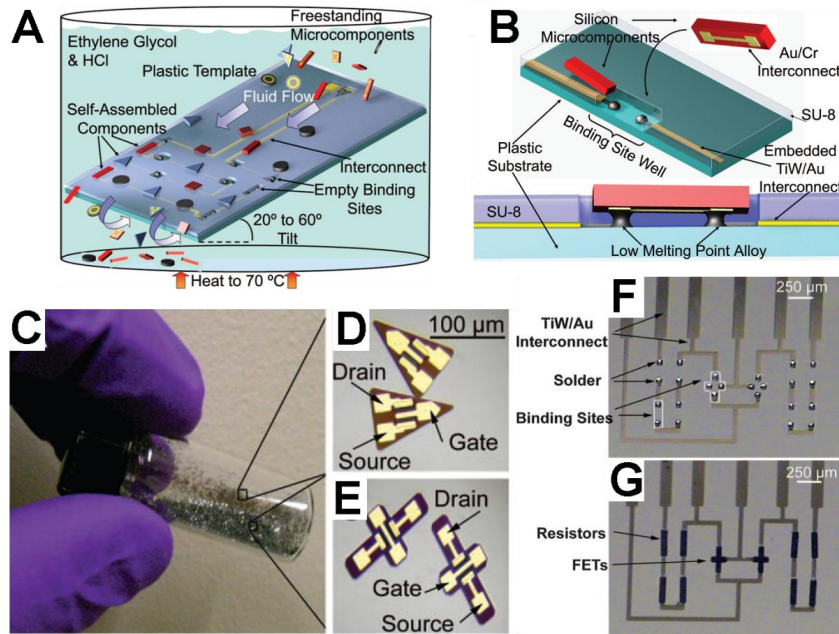


Figure 1.4. An example using fluidic assembly to assemble microdevices onto a plastic substrate. A) Illustrative overview of process; B) Closer detailed view; C) Collected freestanding single crystal silicon FETs; D) triangular FETs; E) cross-shaped FETs; F) Plastic substrate with empty binding sites; G) Substrate after assembly with transistor and resistor in place.¹⁰⁷

1.4 Externally Controlled Field Driven Manipulation of Colloids

1.4.1 Electric fields

In the presence of direct (DC) or alternating current (AC) fields, colloidal particles exhibit a variety of responses. The particles may become motile, where the direction of motion is generally determined by the field direction and particle/solvent composition, or the particles may be induced to interact with one another and assemble into a specific configuration. Some of the major phenomena resulting from electric fields in fluid systems include electrophoresis, electroosmosis and dielectrophoresis. Figure 1.5 illustrates these cases.

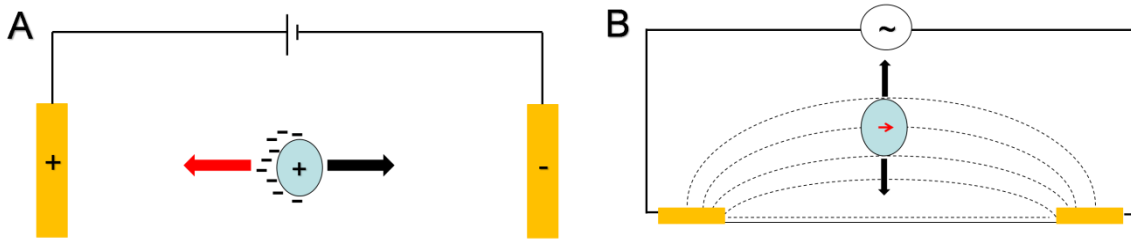


Figure 1.5. Schematic illustration of the three electric field phenomena: A) Positively charged particle in a DC electric field, where the black arrow indicates the electrophoretic force and the red arrow indicates electroosmotic flow, and B) Particle in a non-uniform AC electric field, with an induced dipole indicated by small red arrow, experiencing a dielectric force either to a higher or lower field gradient (black arrows); dashed lines represent AC field.

1.4.1.1 Electrophoresis and Electroosmosis

Particles suspended in water undergo electrophoresis in the presence of a DC electric field, where the particles are attracted to the oppositely charged electrode. The particle's migration speed, v , is a product of its electrophoretic mobility, μ , and the electric field strength, E (Equation 1.1). The electrophoretic mobility is proportional to the dielectric constant of the solvent, ϵ , the zeta potential of the particle, ζ , and inversely proportional to the solvent viscosity, η (Equation 1.2).

$$v = \mu E \quad \text{Equation 1.1}$$

$$\mu \propto \frac{\epsilon \zeta}{\eta} \quad \text{Equation 1.2}$$

The exact form of Equation 1.2 depends on the size of the electric double layer surrounding the particle relative to the particle size. Electroosmosis, on the other hand, refers to bulk fluid flow resulting from the movement of ions in solution. These ions originate from the particle counter-ions, as well as ions from the walls of the experimental cell or channel. When a DC electric field is applied, the mobile counter-ions are set in motion, creating a fluid flow parallel to the particle surface. Shear stresses are exerted upon the particle by the fluid flow, affecting its speed and direction. For the case of DC fields and aqueous systems, both electrophoretic and electroosmotic effects are typically present so the particle migration depends on the relative magnitudes of the two phenomena (Figure 1.5A).

In DC and AC electric fields, it is possible to assemble ordered colloidal aggregates.¹⁰⁹⁻¹¹² This process has been referred to as electrophoretic assembly, and though the mechanism details are not well understood, electroosmosis is thought to play a part. Additionally, a process referred to as induced-charge electrophoresis or AC particle electrophoresis has been used to induce particle translational motion in uniform AC fields. This was successfully demonstrated with metallodielectric Janus particles.¹¹³ Electroosmosis can also result in the translational mobility of particles. For example, semiconductor diode nanowires composed of bisegmented polypyrrole/cadmium (Ppy/Cd) or trisegmented cadmium selenide/gold/cadmium selenide (CdSe/Au/CdSe) were found to exhibit directed motion in the presence of a uniform AC field. The authors confirmed the absence of dielectrophoretic forces on the micro-diodes, by comparing its response to the field with polystyrene spheres, monocomponent wires and bisegmented Ppy/Au nanowires (ohmic junction). The non-diode particles did not exhibit directed motion in the uniform AC field

indicating that the local electroosmotic flux powered by the external field was driving the motion of the micro-diodes.¹¹⁴

1.4.1.2 Dielectrophoresis

The main source of AC electric field responses in particle suspensions is the frequency dependent polarization of particles. The movement of particles is dependent on the local electric field, the dielectric properties of the particles and the suspending medium, frequency, surface charge density, concentration of free charges in the vicinity of the particle, geometry of the particle, and electrode geometry.¹¹⁵⁻¹¹⁷ At most frequencies, metallic and conductive particles are always strongly polarized. For dielectric particles, the polarization is very frequency dependent. At low frequencies, the particles are more polarizable than water because of the high conductance, and thus the higher induced polarization, of the counter-ions. This is the case regardless of whether the particle permittivity is greater or less than water. At high frequencies however, the counter-ions can no longer be effectively polarized by the field because the change in field direction is too rapid for the ions to follow. The interactions between the induced dipoles and a non-uniform AC electric field result in the dielectrophoretic force, causing particle mobility. Note that if the AC field is uniform, there is no particle motion because the force acting on each of the two poles in the induced dipole within the particle is equal and opposite. In non-uniform fields, particle mobility occurs because the force acting on the two poles is not the same because of the field gradient. For particles more polarizable than the media, they experience a force towards regions of higher field intensity (positive dielectrophoresis). Particles less polarizable than the media are

forced away from these regions (negative dielectrophoresis). Though dielectrophoresis can occur in both AC and DC fields, AC fields are generally preferred as large DC field strengths cannot be applied to aqueous media as water electrolysis can occur.

Dielectrophoresis has been shown to be a facile method for the assembly of colloidal suspensions.^{116, 118-120} This is due to the fact that the induced dipoles within the particles interact with one another when the particles come into close contact. The particles align in chains along the direction of the field lines (Figure 1.6A). This process has been used to align particulates, such as carbon nanotubes, ceramic nanoparticles and glass fiber, in composites for improved mechanical or electrical performance.¹²¹⁻¹²⁴ In these composite examples, the particles were generally highly polydisperse and comprised of random nonspecific shapes, so the assemblies were not well-structured. In one interesting example using Janus metallodielectric spherical particles, the chains had a zig-zag conformation so that the metallic hemispheres aligned and the polymer hemispheres oriented in alternating directions without contacting any other particles (Figure 1.6B).¹²⁵ Particle crystallization also occurred when, once the chains form and move to the regions of high field intensity (positive dielectrophoresis), they then attract one another laterally to crystallize. These assemblies are reversible by switching on/off the field. Most of the examples of the dielectrophoretic assembly of monodisperse colloidal systems have been with spherical particles, which generally crystallize into hexagonal close packed assemblies.¹²⁶ Some research has focused on the assembly of anisotropic rod-like particles via dielectrophoresis, where the particles have been primarily biological,^{117, 127-130} such as cells, viral particles and bacteria for the fabrication of biofilms and tissue or in diagnostics and separation. Both experimental and theoretical studies have indicated that ellipsoidal particles exhibit more

complex behavior in nonuniform electric fields because there are more degrees of freedom from the typical isotropic case of the sphere.¹³¹ In fact, there is a preferred or more stable orientation for these shapes, where they align with their long axis parallel to the axis of the electric field.¹³⁰⁻¹³²

1.4.2 Magnetic Fields

Magnetic particles are widely used in a variety of applications including different magnetic separation techniques, for magnetically induced hyperthermia of tumors, as contrast enhancement agents for magnetic resonance imaging, drug delivery, and high density data storage.¹³³⁻¹³⁵ Magnetic particles can be synthesized in a range of shapes and sizes, as well as a range of magnetic material such as Co, Fe₃O₄, Fe₂O₃, FePt, Ni, Mn₃O₄ and MnO.⁶⁷ Magnetic particles can also be composite particles. In terms of assemblies, magnetic nanoparticles self-assemble with their magnetic moments aligned in the direction of the local magnetic field due to neighboring particles or applied magnetic fields. The outcome of this is directional assemblies such as chains/wires or rings.^{136, 137}

Composite magnetic particles are particularly interesting because of the different opportunities for organizing the magnetic material within the composite particle. Alignment of the magnetic nanoparticles within the composite particle plays an important role in the overall magnetic properties, and thus the behavior of such particles in the presence of an external magnetic field. For example, Dyab *et al.* showed that aligning and concentrating magnetite nanoparticles in their microparticles resulted in a change from superparamagnetic behavior of the nanoparticles to ferromagnetic behavior of the composite microparticles; furthermore, for Janus microparticles, the colloidal materials exhibited zigzag chaining in an

external magnetic field.⁴⁹ Hwang *et al.* studied the effect of shape on the alignment of magneto-polymer composite particles with the magnetic nanoparticles uniformly distributed. They found that unlike the spheres, disks and plugs exhibited a directional preference to an external magnetic field arising from their shape asymmetry (Figure 1.6C).¹³⁸ The directed assembly or the self-assembly of magnetic particles has been found to be exceedingly useful in the fabrication of photonic crystals^{11, 48, 139} and as nanowire contacts in electronic devices.¹⁴⁰⁻¹⁴² They are also used as device components in microfluidics.¹⁴³⁻¹⁴⁶ Additionally, there has been growing interest in the use of magnetic particles in the fabrication of nanomotors and nanomachines.¹⁴⁷⁻¹⁵⁰

Magnetic forces can be used for both the propulsion and steering of micromotors. For example, a micromotor system was fabricated by stringing streptavidin coated magnetic beads together linked by dibiotinylated double stranded DNA molecules. The magnetic chain was then attached to a red blood cell. A transverse oscillating magnetic field was used to generate a beating motion of the magnetic tail of the motor resulting in unidirectional motion in a manner similar to spermatozoa, where a bending wave propagated from the head to the tail inducing a net translational velocity. The speed and direction of the motor was adjusted by manipulating the external field.¹⁴⁸

1.4.3 Optical fields

In the 1970s, it was discovered that colloidal particles can be held using the single-beam gradient force trap or optical tweezers.^{151, 152} This technique has garnered prominence as a powerful tool for manipulating individual particles.¹⁵³ In general, the light's electric field gives rise to electric dipoles in small particles, and the particles are then directed along

intensity gradients to the focus. Larger particles, however, act as lenses, refracting rays of light and redirecting the momentum of their photons. The resulting recoil draws them towards the higher flux of the photons near the focus.¹⁵³ Optical tweezers are ideal for systems with small quantities of particles (Figure 1.6D), and it is not yet considered applicable to the large scale manipulation of colloidal systems. A larger scale optical approach requires the generation of an interfering electromagnetic wave.^{154, 155} For example, Burns *et al.* demonstrated the formation of arrays of extended crystalline structures from the interaction of dielectric particles with electromagnetic fields.¹⁵⁴ Another approach that uses light to order particles is using the holographic patterning of photocurable monomers and metal precursors to generate periodic polymer/metal nanocomposites.¹⁵⁶

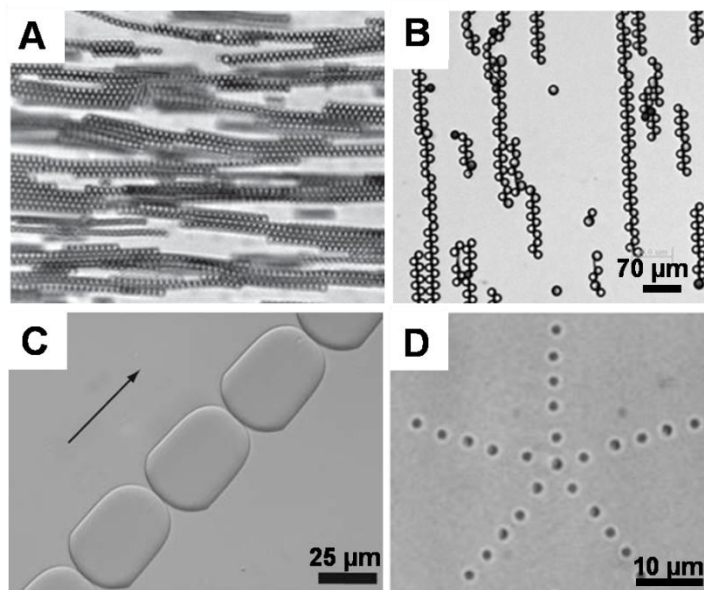


Figure 1.6. Examples of external field driven assemblies. A) Chaining of PS microspheres using dielectrophoresis.¹⁵⁷ B) Staggered chain formation of metallodielectric Janus particles using dielectrophoresis.¹⁵⁷ C) Chaining of magnetic composite particles in a magnetic field (arrow indicates field direction) where particles exhibit directional preference in the field.¹³⁸

D) 800 nm PS spheres (in water) assembled into a star configuration with dynamic optical trapping patterns.¹⁵³

1.5 Applications

There are numerous applications that utilize manipulated colloids, and a few of these applications are showcased in this section. Some of these applications rely exclusively on colloidal technology, such as magnetorheological and electrorheological fluids, while others have found varying measures of success with alternate technologies, such as photonic crystal fabrication. The applications also vary with respect to their commercial success. Table 1.1 outlines these applications.

1.5.1 Smart Fluids

Both magnetorheological (MR) and electrorheological (ER) fluids are referred to as smart fluids because they exhibit significant resistance to flow upon the application of an external field due to the formation of particle chains oriented parallel to the direction of the field. The properties of these fluids depend strongly and reversibly on the applied field. In both cases, the carrier liquid is typically silicone oil. Of the two, MR fluids dominate the smart fluid field in terms of commercial applications. MR fluids are used widely in automotive applications, such as controllable suspension struts, seat dampers and in rotary brakes. ER fluids, however, have not achieved commensurate commercial success.^{1, 158}

1.5.2 Photonic Crystals

A photonic crystal is a regularly structured material that exhibits a strong interaction with light.¹⁵⁹ Photonic crystals can be fabricated from the assembly and crystallization of particles. For example, monodisperse spherical particles can be assembled by sedimentation to form a fcc colloidal crystal. Infiltration of a high dielectric constant material into the interstitial spaces, followed by etching of the spherical particles, produces a high dielectric constant inverse opal photonic crystal structure. In addition, as some metal nanoparticles exhibit strong surface plasmon resonances in the visible wavelength range, assemblies of ordered arrays of interacting metallic nanoparticles can result in interesting novel optical responses.¹⁶⁰ One dimensional photonic crystals, using particle technology, are commercially available in thin film optics. There have been several start-up companies with photonic crystals as a major research and development focus, and though 3D periodic photonic crystals, such as opals, are sold, they have been largely for research purposes and not engineering applications.¹⁶¹

1.5.3 Micro-electronics

Light-emitting diodes and field-effect transistors are just some of the microelectronic devices that can be fabricated by manipulating colloidal particles (nanowires and other device components). The components can be effectively manipulated with fluidic assembly, magnetic fields and dielectrophoresis, for example.¹⁰⁶ In particular, fluidic assembly has been successfully applied to the manufacture of radio frequency identification (RFID) tags.^{106, 162}

1.5.4 Micro-Pumps and Micro-Motors for Lab-on-a-Chip Machinery

Well-controlled micro-devices are desirable components of microfluidic systems and colloidal particles can act as these device components. Kavcic *et al.* designed a micropump from superparamagnetic colloidal spheres where the spheres were assembled using an external magnetic field and then the rotor was powered using dielectrophoresis.¹⁴⁴ Biswal and Gast assembled paramagnetic particles into chains and used magnetic actuation for rapid and controlled mixing in microchannels.¹⁴³ Optical traps can also be used to manipulate colloidal particles to perform as valves and pumps in microfluidic devices.¹⁶³

1.5.5 Colloidal Surfactants

Pickering emulsions, where particles accumulate at the interface between two immiscible liquids and stabilize the emulsion drops against coalescence by forming a mechanically robust monolayer at the liquid-liquid interface,⁸³ have been used industrially for many years, for example in crude oil recovery and cosmetic preparations.¹⁶⁴ Particles adsorb to the liquid-liquid interface typically because they are wetted by both liquids. Chemical anisotropy can increase the efficiency of adsorption, for example amphiphilic Janus particles adsorb more easily than their isotropic counterparts because of their amphiphilicity, and they adsorb more strongly than molecular surfactants because of their size.⁸³ Thus it is expected that Janus particles, with both chemical and shape anisotropy, would produce better emulsions for the many industrial processes and products that use emulsion technology.

1.5.6 *In vivo* Transport/Therapeutic Delivery

Controlling the transport of drug delivery vectors is an important challenge in disease treatment. External fields have been used to try to address this issue. Magnetic fields can be used to manipulate particles in simulated blood flow conditions using very strong electromagnets, such as a low T_c superconducting coil.¹⁶⁵ Also, magnetofection uses magnetic fields to efficiently and reliably introduce nucleic acids to various cell types.¹⁶⁶ Electric fields can also be used to manipulate particles in living systems. For example, iontophoresis has been used to enhance the penetration of drug-loaded nanoparticles into ocular structures, where the mechanism for particle mobility may involve electrorepulsion, electroosmosis and current-induced tissue damage.¹⁶⁷ Particle design is also a key parameter in transport and therapeutic delivery. For example, chemical modification of the particle surface with targeting ligands increases the probability that the particle is taken up by the target cells.¹⁶⁸ Additionally, the mechanical properties of the particle affect its ability to circulate in blood vessels and traverse the tumor vasculature.¹⁶⁹

1.5.7 Particle-based Display Technologies

Particle-based displays are an emerging technology that depends greatly on particle properties and particle manipulation. Building on the ground-breaking work of Comiskey *et al.*² in the development of electrophoretic image display (EPID) technology, researchers have pursued the fabrication of stable, flexible and inexpensive EPIDs to replace conventional paper.^{170, 171} This technology has been commercialized by E-Ink Corporation,¹⁷² and has

been used in electronic book products. Other display technologies, such as AC-electroluminescent displays,³ are also being explored.

Table 1.1. Selected applications that utilize controlled colloidal manipulation techniques

Application	Method of Manipulation	Non-colloidal alternatives	Commercialization	Refs.
Smart fluids	Magnetic, electric fields	none	Yes; e.g. automotive industry	1
Photonic crystals	Convective assembly, templating, external fields	Lithography	Yes, but largely for research purposes	161
Microelectronics	External fields, fluidic assembly, templating	Lithography	Yes, e.g. RFID manufacture	106
Colloidal surfactants	Capillary forces; particle design	Molecular surfactants	Commodity, not high value, e.g. cosmetic preparation	83, 84
Micro-machinery in microfluidics	Magnetic, electrical, optical fields	Channel geometry, peristaltic pumping etc.	No	143, 163
<i>In vivo</i> transport/ Therapeutic delivery	Magnetic/electric fields; particle design	Non-particulate methods of treatment	No	165, 167, 169
Particle-based displays	Electric fields	Liquid crystal displays, light emitting diode displays etc.	Yes; e-books etc	2, 3

1.6 Summary

Smart, multifunctional materials are needed for numerous applications in both materials and life sciences, and this has kindled a great deal of interest in the fabrication and manipulation of colloidal particles. Furthermore, the need for tailored particles has far

exceeded what can be supplied commercially today. Commodity colloids, capable of being produced at a capacity of 1 million metric tons per year by the leading suppliers (Dow, Rohm and Haas, BASF), are used in paints, glues, inks, among other household items.¹⁷³ On a relatively smaller scale, higher quality, more expensive particles are supplied (largely for research purposes) by a number of relatively smaller companies (Interfacial Dynamics, Polysciences, Duke Scientific, etc.).¹⁷³ Xia *et al.* provides a longer, more detailed list of high quality particle suppliers.⁹ Though very costly, it is also possible to have particles customized to have specific properties. These particles, however, are all spherical. Anisotropically-shaped metal nanoparticles are commercially available, such as gold nanorods and nanowires from Sigma-Aldrich.¹⁷⁴ Many emerging particle fabrication techniques were mentioned in this chapter and though much has been achieved, each process has its drawbacks, be it materials specificity, low production yields or particle size limitations. Thus, there is still the challenge of scaling up the production of highly tailored particles. This is the focus of small companies, such as Liquidia Technologies.¹⁷⁵ Velegol *et al.* proposed that one approach to address the particle demand is for small companies to develop “colloidal microfactories” for adaptable batch unit operations of high-value specialty colloidal products to meet the niche market, by producing on a 10 -100 g/batch scale with a rapid turnaround time.¹⁷³

As described in this chapter, researchers are working actively to meet the challenge of controlled particle manipulation. Depending on the application, the techniques discussed can be used independently to control the growth of particle assemblies or particle movement, however, greater control can be achieved if multiple techniques are combined for a more effective and comprehensive process. For example, many of the catalytic systems for

particle propulsion described in Section 1.3.2, can be enhanced with steering capabilities by the addition of a magnetic component, such as nickel, in the particle composition.^{97, 98} These guided nanomotors have been shown to perform functions such as loading and unloading cargo.^{147, 176}

For many of these manipulation processes, the transition to an industrial setting is not straightforward, especially as there are, in some cases, established alternate technologies that can achieve similar outcomes. For example, for applications that require 2D micro- and nano-structures, mature lithographic techniques, such as photolithography, are appealing alternatives to less established processes such as the controlled sedimentation of particles, where defects are more likely to occur.

1.7 References

1. Stanway, R. *Mat. Sci. Tech.* **2004**, 20, 931-939.
2. Comiskey, B.; Albert, J. D.; Yoshizawa, H.; Jacobson, J. *Nature* **1998**, 394, 253-255.
3. Wood, V.; Panzer, M. J.; Chen, J.; Bradley, M. S.; Halpert, J. E.; Bawendi, M. G.; Bulovic, V. *Adv. Mater.* **2009**, 21, 2151-2155.
4. Patel, H.; Somani, R.; Bajaj, H.; Jasra, R. *Bull. Mater. Sci.* **2006**, 29, 133-145.
5. Glotzer, S. C.; Solomon, M. J. *Nat. Mater.* **2007**, 6, 557-562.
6. Merkel, T.; Herlihy, K.; Nunes, J.; Orgel, R.; DeSimone, J. M. *Langmuir* **2009**, in press.
7. Xia, Y.; Xiong, Y.; Lim, B.; Skrabalak, Sara E. *Angew. Chem. Int. Ed.* **2009**, 48, 60-103.
8. Yang, S. M.; Kim, S. H.; Lim, J. M.; Yi, G. R. *J. Mater. Chem.* **2008**, 18, 2177-2190.
9. Xia, Y.; Gates, B.; Yin, Y.; Lu, Y. *Adv. Mater.* **2000**, 12, 693-713.
10. Manoharan, V. N.; Elsesser, M. T.; Pine, D. J. *Science* **2003**, 301, 483-487.
11. Lu, Y.; Yin, Y.; Xia, Y. *Adv. Mater.* **2001**, 13, 415-420.
12. Xia, Y.; Yin, Y.; Lu, Y.; McLellan, J. *Adv. Funct. Mater.* **2003**, 13, 907-918.
13. Champion, J. A.; Katare, Y. K.; Mitragotri, S. *Proc. Natl. Acad. Sci. U.S.A.* **2007**, 104, 11901-11904.
14. Lu, Y.; Yin, Y.; Xia, Y. *Adv. Mater.* **2001**, 13, 271-274.
15. Suter, S. P.; Boylan, C. W. *J. Colloid Interface Sci.* **1980**, 73, 295-297.
16. Sun, Y.; Mayers, B.; Xia, Y. *Adv. Mater.* **2003**, 15, 641-646.
17. Sun, Y.; Xia, Y. *Nano Lett.* **2003**, 3, 1569-1572.
18. Talapin, D. V.; Nelson, J. H.; Shevchenko, E. V.; Aloni, S.; Sadtler, B.; Alivisatos, A. P. *Nano Lett.* **2007**, 7, 2951-2959.
19. Jana, N. R.; Gearheart, L.; Murphy, C. J. *J. Phys. Chem. B* **2001**, 105, 4065-4067.
20. Sun, Y.; Mayers, B.; Xia, Y. *Nano Lett.* **2003**, 3, 675-679.
21. Wiley, B.; Sun, Y.; Xia, Y. *Langmuir* **2005**, 21, 8077-8080.
22. Cai, Z.; Martin, C. R. *J. Am. Chem. Soc.* **1989**, 111, 4138-4139.
23. Hurst, S., J.; Payne, E. K.; Qin, L.; Mirkin, C., A. *Angew. Chem., Int. Ed.* **2006**, 45, 2672-2692.
24. Martin, C. R. *Chem. Mater.* **1996**, 8, 1739-1746.

25. Geng, Y.; Ahmed, F.; Bhasin, N.; Discher, D. E. *J. Phys. Chem. B* **2005**, 109, 3772-3779.
26. Zhu, J.; Hayward, R. C. *J. Am. Chem. Soc.* **2008**, 130, 7496-7502.
27. Dendukuri, D.; Gu, S. S.; Pregibon, D. C.; Hatton, T. A.; Doyle, P. S. *Lab Chip* **2007**, 7, 818-828.
28. Hernandez, C. J.; Mason, T. G. *J. Phys. Chem. C* **2007**, 111, 4477-4480.
29. Gratton, S. E. A.; Williams, S. S.; Napier, M. E.; Pohlhaus, P. D.; Zhou, Z.; Wiles, K. B.; Maynor, B. W.; Shen, C.; Olafsen, T.; Samulski, E. T.; DeSimone, J. M. *Acc. Chem. Res.* **2008**, 41, 1685-1695.
30. Han, M.; Lee, W.; Lee, S.-K.; Lee, S. S. *Sen. Actuators, A* **2004**, 111, 14-20.
31. Dendukuri, D.; Doyle, P. S. *Adv. Mater.* **2009**, 21, 4071-4086.
32. Rolland, J. P.; Maynor, B. W.; Euliss, L. E.; Exner, A. E.; Denison, G. M.; DeSimone, J. M. *J. Am. Chem. Soc.* **2005**, 127, 10096-10100.
33. Dinsmore, A. D.; Hsu, M. F.; Nikolaidis, M. G.; Marquez, M.; Bausch, A. R.; Weitz, D. A. *Science* **2002**, 298, 1006-1009.
34. Badaire, S.; Cottin-Bizonne, C.; Stroock, A. D. *Langmuir* **2008**, 24, 11451-11463.
35. Zhao, K.; Mason, T. G. *Phys. Rev. Lett.* **2007**, 99, 268301.
36. Nunes, J.; Herlihy, K. P.; Mair, L.; Superfine, R.; DeSimone, J. M. *Nano Lett.* **2010**, 10, 1113-1119.
37. Herlihy, K. P.; Nunes, J.; DeSimone, J. M. *Langmuir* **2008**, 24, 8421-8426.
38. Dendukuri, D.; Pregibon, D. C.; Collins, J.; Hatton, T. A.; Doyle, P. S. *Nat. Mater.* **2006**, 5, 365-369.
39. Park, S.; Lim, J.-H.; Chung, S.-W.; Mirkin, C. A. *Science* **2004**, 303, 348-351.
40. Zhang, H.; Nunes, J. K.; Gratton, S. E. A.; Herlihy, K. P.; Pohlhaus, P. D.; DeSimone, J. M. *New J. Phys.* **2009**, 11, 075018.
41. Kim, J.-W.; Larsen, R. J.; Weitz, D. A. *J. Am. Chem. Soc.* **2006**, 128, 14374-14377.
42. Higuchi, T.; Tajima, A.; Motoyoshi, K.; Yabu, H.; Shimomura, M. *Angew. Chem. Int. Ed.* **2009**, 48, 5125-5128.
43. Higuchi, T.; Tajima, A.; Yabu, H.; Shimomura, M. *Soft Matter* **2008**, 4, 1302-1305.
44. Jeon, S.-J.; Yi, G.-R.; Koo, C. M.; Yang, S.-M. *Macromolecules* **2007**, 40, 8430-8439.
45. Yabu, H.; Higuchi, T.; Ijio, K.; Shimomura, M. *Chaos* **2005**, 15, 047505-7.
46. Yabu, H.; Higuchi, T.; Shimomura, M. *Adv. Mater.* **2005**, 17, 2062-2065.
47. Caruso, F.; Susha, A., S.; Giersig, M.; Möhwald, H. *Adv. Mater.* **1999**, 11, 950-953.

48. Ge, J.; Lee, H.; He, L.; Kim, J.; Lu, Z.; Kim, H.; Goebel, J.; Kwon, S.; Yin, Y. *J. Am. Chem. Soc.* **2009**, 131, 15687-15694.
49. Dyab, A. K. F.; Ozmen, M.; Ersoz, M.; Paunov, V. N. *J. Mater. Chem.* **2009**, 19, 3475-3481.
50. Ge, J.; Hu, Y.; Zhang, T.; Yin, Y. *J. Am. Chem. Soc.* **2007**, 129, 8974-8975.
51. Isojima, T.; Suh, S. K.; Vander Sande, J. B.; Hatton, T. A. *Langmuir* **2009**, 25, 8292-8298.
52. Zhao, N.; Gao, M. *Adv. Mater.* **2009**, 21, 184-187.
53. Cayre, O.; Paunov, V. N.; Velev, O. D. *Chem. Comm.* **2003**, 2296-2297.
54. Cayre, O.; Paunov, V. N.; Velev, O. D. *J. Mater. Chem.* **2003**, 13, 2445-2450.
55. Cui, J.-Q.; Kretzschmar, I. *Langmuir* **2006**, 22, 8281-8284.
56. Pawar, A. B.; Kretzschmar, I. *Langmuir* **2008**, 24, 355-358.
57. Kim, S.-H.; Yi, G.-R.; Kim, K. H.; Yang, S.-M. *Langmuir* **2008**, 24, 2365-2371.
58. Jackson, A. M.; Myerson, J. W.; Stellacci, F. *Nat. Mater.* **2004**, 3, 330-336.
59. Percec, V.; Wilson, D. A.; Leowanawat, P.; Wilson, C. J.; Hughes, A. D.; Kaucher, M. S.; Hammer, D. A.; Levine, D. H.; Kim, A. J.; Bates, F. S.; Davis, K. P.; Lodge, T. P.; Klein, M. L.; DeVane, R. H.; Aqad, E.; Rosen, B. M.; Argintaru, A. O.; Sienkowska, M. J.; Rissanen, K.; Nummelin, S.; Ropponen, J. *Science* **2010**, 328, 1009-1014.
60. Pena, D. J.; Mbindyo, J. K. N.; Carado, A. J.; Mallouk, T. E.; Keating, C. D.; Razavi, B.; Mayer, T. S. *J. Phys. Chem. B* **2002**, 106, 7458-7462.
61. Nisisako, T.; Torii, T.; Takahashi, T.; Takizawa, Y. *Adv. Mater.* **2006**, 18, 1152-1156.
62. Bong, Ki W.; Bong, Ki T.; Pregibon, D. C.; Doyle, P. S. *Angew. Chem. Int. Ed.* **2010**, 49, 87-90.
63. Jiang, S.; Schultz, M. J.; Chen, Q.; Moore, J. S.; Granick, S. *Langmuir* **2008**, 24, 10073-10077.
64. Anderson, V. J.; Lekkerkerker, H. N. W. *Nature* **2002**, 416, 811-815.
65. Islam, A. M.; Chowdhry, B. Z.; Snowden, M. J. *Adv. Colloid Interface Sci.* **1995**, 62, 109-136.
66. Velev, O. D.; Gupta, S. *Adv. Mater.* **2009**, 21, 1897-1905.
67. Bishop, K. J. M.; Wilmer, C. E.; Soh, S.; Grzybowski, B. A. *Small* **2009**, 5, 1600-1630.
68. Badaire, S.; Cottin-Bizonne, C.; Woody, J. W.; Yang, A.; Stroock, A. D. *J. Am. Chem. Soc.* **2007**, 129, 40-41.

69. Zhao, K.; Mason, T. G. *Phys. Rev. Lett.* **2007**, 99, 268301.
70. Leunissen, M. E.; Christova, C. G.; Hynninen, A.-P.; Royall, C. P.; Campbell, A. I.; Imhof, A.; Dijkstra, M.; van Roij, R.; van Blaaderen, A. *Nature* **2005**, 437, 235-240.
71. Srivastava, S.; Kotov, N. A. *Acc. Chem. Res.* **2008**, 41, 1831-1841.
72. Podsiadlo, P.; Kaushik, A. K.; Arruda, E. M.; Waas, A. M.; Shim, B. S.; Xu, J.; Nandivada, H.; Pumplun, B. G.; Lahann, J.; Ramamoorthy, A.; Kotov, N. A. *Science* **2007**, 318, 80-83.
73. Dierking, I.; Biddulph, G.; Matthews, K. *Phys. Rev. E* **2006**, 73, 011702.
74. Lapointe, C. P.; Mason, T. G.; Smalyukh, I. I. *Science* **2009**, 326, 1083-1086.
75. Liu, Q.; Cui, Y.; Gardner, D.; Li, X.; He, S.; Smalyukh, I. I. *Nano Lett.* **2010**, 10, 1347-1353.
76. Musevic, I.; Skarabot, M.; Tkalec, U.; Ravnik, M.; Zumer, S. *Science* **2006**, 313, 954-958.
77. Smalyukh, I. I.; Lavrentovich, O. D.; Kuzmin, A. N.; Kachynski, A. V.; Prasad, P. N. *Phys. Rev. Lett.* **2005**, 95, 157801.
78. Tkalec, U.; Skarabot, M.; Musevic, I. *Soft Matter* **2008**, 4, 2402-2409.
79. Pickering, S. U. *J. Chem. Soc., Trans.* **1907**, 91, 2001-2025.
80. Bowden, N.; Terfort, A.; Carbeck, J.; Whitesides, G. M. *Science* **1997**, 276, 233-235.
81. Brown, A. B. D.; Smith, C. G.; Rennie, A. R. *Phys. Rev. E* **2000**, 62, 951.
82. Bowden, N.; Choi, I. S.; Grzybowski, B. A.; Whitesides, G. M. *J. Am. Chem. Soc.* **1999**, 121, 5373-5391.
83. Kim, J.-W.; Lee, D.; Shum, H. C.; Weitz, D. A. *Adv. Mater.* **2008**, 20, 3239-3243.
84. Glaser, N.; Adams, D. J.; Boker, A.; Krausch, G. *Langmuir* **2006**, 22, 5227-5229.
85. Dendukuri, D.; Hatton, T. A.; Doyle, P. S. *Langmuir* **2006**, 23, 4669-4674.
86. Lin, K.-h.; Crocker, J. C.; Prasad, V.; Schofield, A.; Weitz, D. A.; Lubensky, T. C.; Yodh, A. G. *Phys. Rev. Lett.* **2000**, 85, 1770.
87. van Blaaderen, A.; Ruel, R.; Wiltzius, P. *Nature* **1997**, 385, 321-324.
88. Cui, Y.; Bjork, M. T.; Liddle, J. A.; Sonnichsen, C.; Boussert, B.; Alivisatos, A. P. *Nano Lett.* **2004**, 4, 1093-1098.
89. Liu, S.; Maoz, R.; Sagiv, J. *Nano Lett.* **2004**, 4, 845-851.
90. Rao, S. G.; Huang, L.; Setyawan, W.; Hong, S. *Nature* **2003**, 425, 36-37.
91. Wang, Y.; Maspoch, D.; Zou, S.; Schatz, G. C.; Smalley, R. E.; Mirkin, C. A. *Proc. Natl. Acad. Sci. U.S.A.* **2006**, 103, 2026-2031.

92. Tien, J.; Terfort, A.; Whitesides, G. M. *Langmuir* **1997**, 13, 5349-5355.
93. Piner, R. D.; Zhu, J.; Xu, F.; Hong, S.; Mirkin, C. A. *Science* **1999**, 283, 661-663.
94. Wilbur, J. L.; Kumar, A.; Biebuyck, H. A.; Kim, E.; Whitesides, G. M. *Nanotechnology* **1996**, 7, 452.
95. Jacobs, H. O.; Whitesides, G. M. *Science* **2001**, 291, 1763-1766.
96. Gibbs, J. G.; Zhao, Y. P. *Appl. Phys. Lett.* **2009**, 94, 163104.
97. Solovev, A. A.; Mei, Y.; Ureña, E. B.; Huang, G.; Schmidt, O., G. *Small* **2009**, 5, 1688-1692.
98. Paxton, W. F.; Sundararajan, S.; Mallouk, T. E.; Sen, A. *Angew. Chem. Int. Ed.* **2006**, 45, 5420-5429.
99. Laocharoensuk, R.; Burdick, J.; Wang, J. *ACS Nano* **2008**, 2, 1069-1075.
100. Catchmark, Jeffrey M.; Subramanian, S.; Sen, A. *Small* **2005**, 1, 202-206.
101. Qin, L.; Banholzer, M. J.; Xu, X.; Huang, L.; Mirkin, C. A. *J. Am. Chem. Soc.* **2007**, 129, 14870-14871.
102. Soong, R. K.; Bachand, G. D.; Neves, H. P.; Olkhovets, A. G.; Craighead, H. G.; Montemagno, C. D. *Science* **2000**, 290, 1555-1558.
103. Wang, Y.; Hernandez, R. M.; Bartlett, D. J.; Bingham, J. M.; Kline, T. R.; Sen, A.; Mallouk, T. E. *Langmuir* **2006**, 22, 10451-10456.
104. Cameron, L. A.; Footer, M. J.; van Oudenaarden, A.; Theriot, J. A. *Proc. Natl Acad. Sci. U. S. A.* **1999**, 96, 4908-4913.
105. Ng, C. P.; Goodman, T. T.; Park, I.-K.; Pun, S. H. *Biomaterials* **2009**, 30, 951-958.
106. Mastrangeli, M.; Abbasi, S.; Varel, C.; Van Hoof, C.; Celis, J.-P.; Bohringer, K. F. *J. Micromech. Microeng.* **2009**, 19, 083001.
107. Stauth, S. A.; Parviz, B. A. *Proc. Natl. Acad. Sci. U.S.A.* **2006**, 103, 13922-13927.
108. Park, W.; Lee, H.; Park, H.; Kwon, S. *Lab Chip* **2009**, 9, 2169-2175.
109. Yeh, S.-R.; Seul, M.; Shraiman, B. I. *Nature* **1997**, 386, 57-59.
110. Bohmer, M. *Langmuir* **1996**, 12, 5747-5750.
111. Trau, M.; Saville, D. A.; Aksay, I. A. *Science* **1996**, 272, 706-709.
112. Trau, M.; Saville, D. A.; Aksay, I. A. *Langmuir* **1997**, 13, 6375-6381.
113. Gangwal, S.; Cayre, O. J.; Bazant, M. Z.; Veleev, O. D. *Phys. Rev. Lett.* **2008**, 100, 058302.
114. Calvo-Marzal, P.; Sattayasamitsathit, S.; Balasubramanian, S.; Windmiller, J. R.; Dao, C.; Wang, J. *Chem. Comm.* **2010**, 46, 1623-1624.

115. Fan, C. Z.; Huang, J. P.; Yu, K. W. *J. Phys. Chem. B* **2006**, 110, 25665-25670.
116. Jones, T. B., *Electromechanics of Particles*. Cambridge University Press: New York, 1995; p 265.
117. Radu, M.; Ionescu, M.; Irimescu, N.; Iliescu, K.; Pologea-Moraru, R.; Kovacs, E. *Biophys. J.* **2005**, 89, 3548-3554.
118. Dong, L.; Huang, J. P.; Yu, K. W. *J. Appl. Phys.* **2004**, 95, 8321-8326.
119. Lumsdon, S. O.; Kaler, E. W.; Velev, O. D. *Langmuir* **2004**, 20, 2108-2116.
120. Velev, O. D.; Bhatt, K. H. *Soft Matter* **2006**, 2, 738-750.
121. Park, C.; Robertson, R. E. *J. Mater. Sci.* **1998**, 33, 3541-3553.
122. Park, C.; Wilkinson, J.; Banda, S.; Ounaies, Z.; Wise, K.; Sauti, G.; Lillehei, P. T.; Harrison, J. J. *Polym. Sci.: B: Polym. Phys.* **2006**, 44, 1751-1762.
123. Tomer, V.; Randall, C. A.; Polizos, G.; Kostelnick, J.; Manias, E. *J. Appl. Phys.* **2008**, 103, 034115.
124. Wilson, S. A.; Maistros, G. M.; Whatmore, R. W. *J. Phys. D: Appl. Phys.* **2005**, 38, 175-182.
125. Gangwal, S.; Cayre, O. J.; Velev, O. D. *Langmuir* **2008**, 24, 13312-13320.
126. Velev, O. D. *Science* **2006**, 312, 376-377.
127. Asencor, F. J.; Santamaria, C.; Iglesias, F. J.; Dominguez, A. *Biophys. J.* **1993**, 64, 1626-1631.
128. Morgan, H.; Green, N. G. *J. Electrostat.* **1997**, 42, 279-293.
129. Poortinga, A. T.; Bos, R.; Busscher, H. J. *Biotechnol. Bioeng.* **2000**, 67, 117-120.
130. Yang, M.; Chew Lim, C.; Liao, R.; Zhang, X. *J. Microelectromech. Sys.* **2006**, 15, 1483-1491.
131. Yang, C. Y.; Lei, U. *J. Appl. Phys.* **2007**, 102, 094702.
132. Saito, M.; Schwan, H. P.; Schwarz, G. *Biophys. J.* **1966**, 6, 313-327.
133. Gupta, A. K.; Gupta, M. *Biomaterials* **2005**, 26, 3995-4021.
134. Pankhurst, Q. A.; Connolly, J.; Jones, S. K.; Dobson, J. *J. Phys. D: Appl. Phys.* **2003**, 36, R167-R181.
135. Weller, D.; Doerner, M. F. *Annu. Rev. Mat. Sci.* **2000**, 30, 611.
136. Niu, H.; Chen, Q.; Zhu, H.; Lin, Y.; Zhang, X. *J. Mater. Chem.* **2003**, 13, 1803-1805.
137. Tripp, S. L.; Dunin-Borkowski, R. E.; Wei, A. *Angew. Chem. Int. Ed.* **2003**, 42, 5591-5593.
138. Hwang, D. K.; Dendukuri, D.; Doyle, P. S. *Lab Chip* **2008**, 8, 1640-1647.

139. Ding, T.; Song, K.; Clays, K.; Tung, C.-H. *Adv. Mater.* **2009**, 21, 1936-1940.
140. Bangar, M. A.; Hangarter, C. M.; Yoo, B.; Rheem, Y.; Chen, W.; Mulchandani, A.; Myung, N. V. *Electroanalysis* **2009**, 21, 61-67.
141. Hangarter, C. M.; Myung, N. V. *Chem. Mater.* **2005**, 17, 1320-1324.
142. Tanase, M.; Silevitch, D. M.; Hultgren, A.; Bauer, L. A.; Searson, P. C.; Meyer, G. J.; Reich, D. H. *J. Appl. Phys.* **2002**, 91, 8549-8551.
143. Biswal, S. L.; Gast, A. P. *Anal. Chem.* **2004**, 76, 6448-6455.
144. Kavcic, B.; Babic, D.; Osterman, N.; Podobnik, B.; Poberaj, I. *Appl. Phys. Lett.* **2009**, 95, 023504-3.
145. Ng, J. M. K.; Gitlin, I.; Stroock, A., D.; Whitesides, G., M. *Electrophoresis* **2002**, 23, 3461-3473.
146. Sawetzki, T.; Rahmouni, S.; Bechinger, C.; Marr, D. W. M. *Proc. Natl. Acad. Sci. U.S.A.* **2008**, 105, 20141-20145.
147. Burdick, J.; Laocharoensuk, R.; Wheat, P. M.; Posner, J. D.; Wang, J. *J. Am. Chem. Soc.* **2008**, 130, 8164-8165.
148. Dreyfus, R.; Baudry, J.; Roper, M. L.; Fermigier, M.; Stone, H. A.; Bibette, J. *Nature* **2005**, 437, 862-865.
149. Ghosh, A.; Fischer, P. *Nano Letters* **2009**, 9, 2243-2245.
150. Tierno, P.; Golestanian, R.; Pagonabarraga, I.; Sagues, F. *Phys. Rev. Lett.* **2008**, 101, 218304.
151. Ashkin, A. *Phys. Rev. Lett.* **1970**, 24, 156.
152. Ashkin, A.; Dziedzic, J. M.; Bjorkholm, J. E.; Chu, S. *Opt. Lett.* **1986**, 11, 288-290.
153. Grier, D. G. *Nature* **2003**, 424, 810-816.
154. Burns, M. M.; Fournier, J.-M.; Golovchenko, J. A. *Science* **1990**, 249, 749-754.
155. Chowdhury, A.; Ackerson, B. J.; Clark, N. A. *Phys. Rev. Lett.* **1985**, 55, 833.
156. Vaia, R. A.; Dennis, C. L.; Natarajan, L. V.; Tondiglia, V. P.; Tomlin, D. W.; Bunning, T. J. *Adv. Mater.* **2001**, 13, 1570-1574.
157. Velev, O. D.; Gangwal, S.; Petsev, D. N. *Annu. Rep. Prog. Chem., Sect. C* **2009**, 105, 213-246.
158. Halsey, T. C. *Science* **1992**, 258, 761-766.
159. Polman, A.; Wiltzius, P. *MRS Bull.* **2001**, 26, 608-610.
160. Stewart, M. E.; Anderton, C. R.; Thompson, L. B.; Maria, J.; Gray, S. K.; Rogers, J. A.; Nuzzo, R. G. *Chem. Rev.* **2008**, 108, 494-521.
161. De La Rue, R. *Nat. Mater.* **2003**, 2, 74-76.

162. *Alien Technologies, www.alientechnology.com.*
163. Terray, A.; Oakey, J.; Marr, D. W. M. *Science* **2002**, 296, 1841-1844.
164. Ashby, N. P.; Binks, B. P. *Phys. Chem. Chem. Phys.* **2000**, 2, 5640-5646.
165. Cha, Y.; Chen, L.; Askew, T.; Veal, B.; Hull, J. *J. Magn. Magn. Mater.* **2007**, 311, 312-317.
166. Buerli, T.; Pellegrino, C.; Baer, K.; Lardi-Studler, B.; Chudotvorova, I.; Fritschy, J.-M.; Medina, I.; Fuhrer, C. *Nat. Protocols* **2007**, 2, 3090-3101.
167. Eljarrat-Binstock, E.; Orucov, F.; Aldouby, Y.; Frucht-Pery, J.; Domb, A. J. *J. Controlled Release* **2008**, 126, 156-161.
168. Ruoslahti, E.; Bhatia, S. N.; Sailor, M. J. *J. Cell Biol.* **2010**, 188, 759-768.
169. Doshi, N.; Zahr, A. S.; Bhaskar, S.; Lahann, J.; Mitragotri, S. *Proc. Natl. Acad. Sci. U.S.A.* **2009**, 106, 21495-21499.
170. Oh, S. W.; Kim, C. W.; Cha, H. J.; Pal, U.; Kang, Y. S. *Adv. Mater.* **2009**, 21, 4987-4991.
171. Kim, C. A.; Joung, M. J.; Ahn, S. D.; Kim, G. H.; Kang, S.-Y.; You, I.-K.; Oh, J.; Myoung, H. J.; Baek, K. H.; Suh, K. S. *Synth. Met.* **2005**, 151, 181-185.
172. *E-Ink Corporation, www.eink.com.*
173. Velegol, D.; Jerri, H. A.; McDermott, J. J.; Chaturvedi, N. *AIChE J.* **2010**, 56, 564-569.
174. *Sigma-Aldrich, www.sigmaaldrich.com.*
175. *Liquidia Technologies, www.liquidia.com.*
176. Sundararajan, S.; Lammert, P. E.; Zudans, A. W.; Crespi, V. H.; Sen, A. *Nano Lett.* **2008**, 8, 1271-1276.

Chapter 2

PRINT[®] Technology and PFPE Characterization

2.1 Introduction

2.1.1 PRINT[®] Technology

The Particle Replication in Non-Wetting Templates (PRINT) technology has emerged as a remarkable particle fabrication tool for the generation of highly tailored micro- and nanoparticles. Developed by the DeSimone research group, the process utilizes perfluoropolyether (PFPE) elastomeric molds to generate ordered arrays of micro- and nanoparticles of varying composition, shape, size, mechanical properties and surface chemistry.^{1,2} These PFPE elastomers exhibit high gas permeability, extremely low surface energies, excellent solvent resistance, excellent release properties, and high thermal stability.³ Furthermore, the molecular weight between crosslinks can be systematically varied, and as a result, the PFPE elastomers can accurately mold to within 1 nm resolution.⁴ The PRINT process is such a versatile and general technology that it is compatible with a broad range of particle compositions, from sensitive biologically active materials requiring extremely mild conditions to the relatively harsh chemistries of ceramics.^{5,6}

The major steps in the PRINT process include (1) mold fabrication, (2) mold filling and particle formation and (3) particle harvesting. To make the mold, master templates with the features of interest are required. Templates are fabricated by etching features into a silicon wafer using standard lithographic techniques common to the electronics industry. A small amount of the PFPE precursor, containing a photoinitiator, is applied to the template where it spreads to wet each feature. A poly(ethylene terephthalate) (PET) film is placed over the PFPE precursor and then it is cured when exposed to UV radiation. The resulting mold, when peeled away from the master, has inverse features to that on the master. The particle precursor liquid is then dropped onto the patterned mold surface. The precursor is

spread over the mold surface using a high surface energy polymeric sheet (usually PET) and roller as shown in Figure 2.1 A-B. The precursor fills the mold cavities via capillary forces and the excess liquid is pulled away by the higher surface energy polymeric sheet. Once the sheet is completely removed, the mold cavities are left full with liquid, with no liquid on the land area between cavities. The particle precursor in the mold cavities is then solidified via a suitable process, such as polymerization, solvent evaporation, phase change, etc. There are different options for the particle harvesting step, depending on the composition and size of the particles. One approach is to laminate the mold onto a sacrificial adhesive, such as polycyanoacrylate, poly(vinyl alcohol) or poly(vinyl pyrrolidone). The mold can be pulled away, leaving an array of particles on the adhesive layer. The particles can be released into solution by dissolving the adhesive. All of these steps are shown schematically in Figure 2.1.

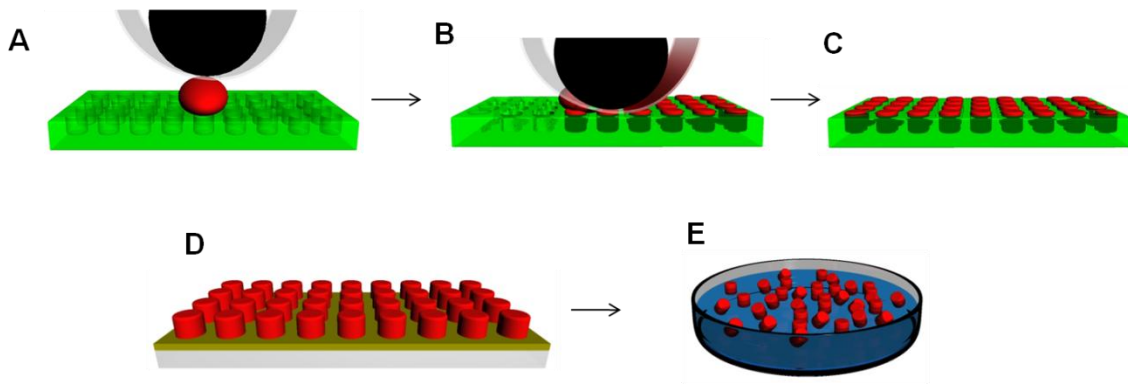


Figure 2.1. Schematic representation of the PRINT process. A) Roller is brought into contact with the particle precursor and the mold; B) Roller evenly distributes the precursor into cavities of mold. Excess liquid is pulled away by the high surface energy polymer sheet; C) Liquid is solidified in the mold to form particles; D) Particles are removed from the mold; E) Particles are collected in solution.

2.1.2 Solid Surface Energy Measurements

The PRINT process relies extensively on the surface properties of the PFPE elastomeric mold, thus a fundamental understanding of the surface energies of PFPE elastomers is desired. These elastomers are prepared by photocuring the precursor polymer, perfluoropolyether dimethacrylate, PFPE-DMA (Figure 2.2). Previous Zisman analyses determined that the critical surface tension, γ_c , of the PFPE elastomer (molecular weight between crosslinks = 4000 g/mol) is 8.6 mN/m.⁷ The Zisman analysis entails plotting the cosines of the contact angles (θ) of several liquids as a function of their surface tensions and extrapolating to $\cos \theta = 1$.⁸

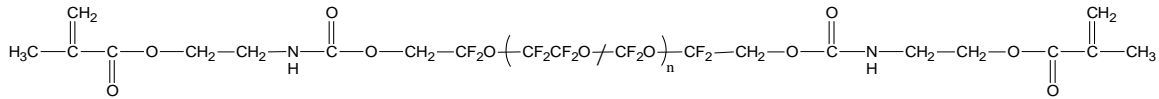


Figure 2.2. Chemical structure of PFPE-DMA

The critical surface tension, γ_c , is a measure of the surface free energy of the solid, γ_{sv} , but it does not necessarily equal γ_{sv} . The relationship between γ_c and γ_{sv} is shown in Equation 2.1. For nonpolar solids, however, γ_c equals γ_{sv} to a first approximation. Zisman and collaborators estimated surface energies for different functional groups.⁹ For surfaces characteristic of the groups: -CH₂-, -CH₃-, -CF₂- and -CF₃-, the critical surface tensions were found to be 31, 22, 18, and 6 mN/m, respectively. Based on this evidence, γ_c of PFPE should be close to 18 mN/m. As a first step in understanding the huge disparity between the expected and experimental values, the solid surface free energy of PFPE elastomers was measured using a contact mechanics method that complements the contact angle measurements used in the Zisman analysis. The method is known as the JKR test.

$$\gamma_c = \gamma_{sv} + \gamma_{sl} \quad \text{Equation 2.1}$$

where γ_{sl} is the surface energy of the solid-liquid interface.

In 1971, Johnson, Kendall and Roberts developed the JKR theory,¹⁰ which is a technique that has been routinely used to determine surface energies, γ_{sv} , of relatively low modulus materials such as polydimethylsiloxane, PDMS.⁹ Moreover the JKR test is one of the few methods available for the direct determination of the surface free energy and work of adhesion between solids.^{11, 12} The test consists of bringing two elastomeric surfaces into contact and measuring the deformation that results due to adhesion forces. For contact between two spherical elastomeric objects, the JKR model predicts the following relationship between the radius of contact deformation, a , and the surface and external forces:

$$a^3 = \left(\frac{R}{K}\right) \left\{ P + 3\pi WR + \left[6\pi WRP + (3\pi WR)^2 \right]^{0.5} \right\} \quad \text{Equation 2.2}$$

$$\frac{1}{K} = \left(\frac{3}{4}\right) \left\{ \frac{(1-\nu_1^2)^2}{E_1} + \frac{(1-\nu_2^2)^2}{E_2} \right\} \quad \text{Equation 2.3}$$

$$\frac{1}{R} = \frac{1}{R_1} + \frac{1}{R_2} \quad \text{Equation 2.4}$$

where P is the external load, W is the work of adhesion, R_1 and R_2 are the radii of curvature of the two spheres, K is the elastic modulus, E_1 and E_2 are the Young's moduli of the two objects, and ν_1 and ν_2 are the Poisson ratios. The most common geometry for this experiment however, is the contact of a sphere with a flat surface as indicated by Figure 2.3. In this case, the radius of curvature of the surface is infinity and R becomes the radius of curvature of the sphere.

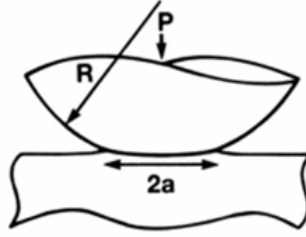


Figure 2.3. Contact interaction of a semi-sphere and planar surface, where the radius of deformation, a , is a function of the load, P .⁹

2.1.3 Capillary Flow

The phenomenon of capillary flow is utilized in the PRINT process in the important mold filling step. Washburn was one of the earliest physicists to study the dynamics of capillary flow.¹³ He derived equations to describe the spontaneous motion of a liquid-gas interface in an open-ended capillary, concluding that the distance traveled by the interface was proportional to the square root of time. Other researchers have since studied capillary flow in closed-end microchannels and have noted that the ability of a liquid to penetrate a cavity depends on such factors as the contact angle (θ) and the size and shape of the cavity.¹⁴⁻
¹⁶ Furthermore, whether the liquid entraps gas in the cavity or completely fills it depends on the permeability of the gas into the surrounding media. For most cases studied, the channel material was not gas-permeable, so diffusion of the entrapped gas into the liquid significantly affected the filling of the closed-end capillary. The general observations were that for a given cross-section, deeper micro-channels take longer to fill, the time taken to flood the micro-channel increased slightly with increasing cross-section, and increasing the contact angle increased the filling time for fixed channel dimensions.

Capillary flow has been used in other molding processes.¹⁷⁻¹⁹ In particular, the procedure referred to as MIMIC (**MicroMolding In Capillaries**) developed by Whitesides and coworkers employed capillary flow to fill PDMS channels with different liquids to be

molded.¹⁹ It was found that if the cavity mouth angle is 90° , which is the case with most PRINT molds, capillary filling will only occur if the liquid to be molded has a contact angle less than 90° , meaning that the liquid is at least partially wetting the PFPE surface. If the contact angle is greater than 90° (non-wetting), additional forces are required to fill the cavity with the liquid.

2.2 Research Objectives

Given the importance of the PRINT process for the fabrication of engineered colloidal particles and particle arrays, it is necessary to have a clear understanding of the surface properties of the PFPE elastomer used as the molding material. As a result, the PFPE elastomer was characterized using contact mechanics, specifically the JKR test, to determine the solid surface free energy. The PFPE surface energy was measured as a function of PFPE molecular weight between crosslinks. Additionally, the effect of solvent extractions was determined. Modulus and water contact angle data were also obtained to complete the analysis.

One integral step in the PRINT process is the scum-free filling of the PFPE molds. The PRINT process utilizes the phenomenon of capillary flow to fill the PFPE molds, which is possible because of PFPE's extremely low surface energy and high gas permeability. Consequently, the phenomenon of capillary flow in PFPE channels was investigated with microscopy. Dead-end PFPE microchannels of varying lengths were studied and compared to polydimethylsiloxane and glass microchannels.

2.3 Experimental

2.3.1 PFPE Synthesis

For this study, different molecular weight PFPE-DMA_s were synthesized; $M_n \approx 1000$ (1K), 4000 (4K), 2×4000 (2×4K) and 3×4000 (3×4K) g/mol. The PFPE diol (either 1K or 4K g/mol), obtained from Solvay Solexis, was converted to the dimethacrylate by treating with isocyanatoethyl methacrylate (Sigma-Aldrich) in the presence of the catalyst, diazabicycloundecene (Sigma-Aldrich) (Figure 2.4). To double or triple the length of the PFPE, a chain extension reaction was performed using isophorone diisocyanate (Sigma-Aldrich) as a linker group (Figure 2.5). The extended diol could then be converted to the dimethacrylate as shown in Figure 2.4. All reactions were carried out in the solvent, 1,1,1-3,3-pentafluorobutane (solkane).

To crosslink PFPE-DMA, 0.1 wt % 2,2-diethoxyacetophenone (Sigma-Aldrich) was added and UV-cured under nitrogen purge (Figure 2.4). Rectangular PFPE samples (1 mm thick) were prepared by curing the PFPE-DMA on silicon wafers. The samples were extracted in solkane to remove any sol fraction from the samples. To achieve this, soxhlet extractions were carried out on the samples for 18 hours followed by vacuum drying the samples at room temperature for 4 hours.

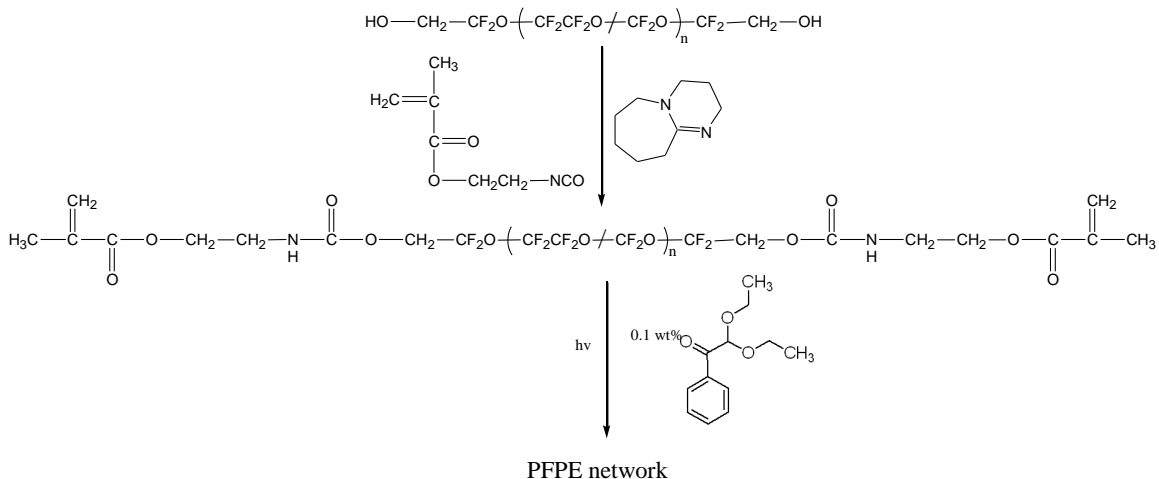


Figure 2.4. Reaction scheme for PFPE-DMA from the PFPE diol

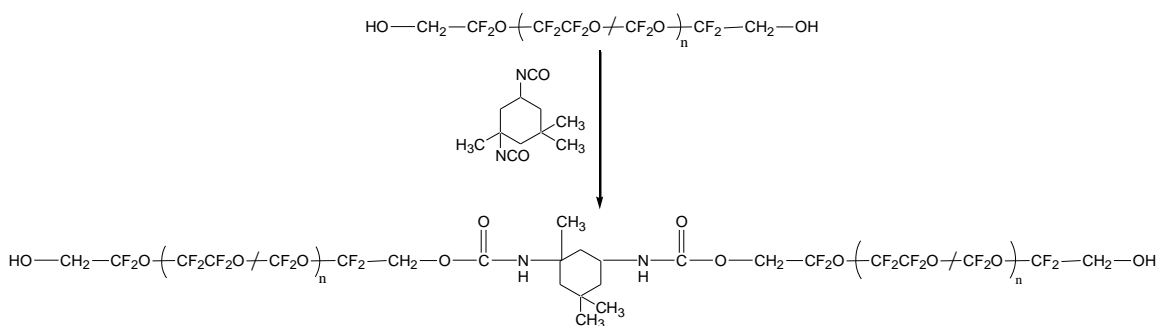


Figure 2.5. Chain extension reaction to form 2× PFPE diol

2.3.2 Contact Angle and Mechanical Characterization of PFPE Elastomers

All elastomers were characterized by mechanical testing and contact angle measurements. The Instron was used to determine the tensile modulus of the elastomers. Rectangular samples were stretched at a constant extension rate of 10 mm/min until break. The data obtained in the first 2% strain was used to calculate the tensile modulus. A contact angle goniometer was used to measure advancing and receding water contact angles on PFPE

by the sessile drop method. The measurements were conducted on both surfaces of the PFPE: nitrogen-exposed surface and silicon-exposed surface.

Water contact angle data is shown in Table 2.1. It is evident that the advancing contact angles on the N₂-exposed surfaces are significantly higher than on the silicon-exposed surface. Priola *et al.* observed similar differences in contact angles in PFPE elastomeric surfaces exposed to glass and air.²⁰ They concluded, based on XPS analyses, that there was a slight surface composition asymmetry between the two surfaces with the air side having higher fluorine content. They determined that this was the major cause for the contact angle differences.

Table 2.1 Water contact angle data

PFPE DMA (solvent extracted)	N ₂ -exposed surface		Si-exposed surface	
	Advancing	Receding	Advancing	Receding
1K/4K Blend (1:1)	119.7 ± 1.9	52.2 ± 2.3	104.1 ± 2.5	59.7 ± 2.7
4K	127.9 ± 1.0	44.7 ± 4.0	114.9 ± 2.3	68.4 ± 3.3
2×4K	131.0 ± 2.3	34.9 ± 4.0	114.5 ± 0.7	66.8 ± 1.1
3×4K	127.8 ± 1.1	40.2 ± 4.7	115.7 ± 2.1	46.1 ± 0.9

2.3.3 JKR Studies

2.3.3.1 Experimental Procedure

PFPE planar sheets and lenses were prepared for the JKR experiments. The planar sheets (2 mm thick) were prepared by UV curing the precursor liquids on a silicon wafer for 2 minutes while purging with N₂. To fabricate PFPE lenses, PDMS lenses were first prepared using the Sylgard[®] 184 Silicone Elastomer Kit (Dow Corning), which contains two

components: a base and a curing agent. The two components were combined in a 10:1 weight ratio (base : curing agent), then degassed in a vacuum oven for two hours. Small drops of the mixture were placed on glass slides treated with trichloro(1H,1H,2H,2H-perfluorooctyl)silane, then polymerized at 110 °C for one hour. The slides were fluorinated to ensure that the PDMS had a finite contact angle on the glass to form the lenses. The radii of curvature of the lenses ranged from 1 mm – 1.5 mm. The PFPE precursor was poured over the elastomeric lenses to make a mold of the lenses. After photopolymerization, the PDMS lenses were removed from the PFPE mold. The PFPE mold was then filled with more of the PFPE precursor liquid and UV cured in N₂. This preparation is described schematically in Figure 2.6. The samples were handled as little as possible to reduce the amount of debris on the surfaces. Some of the lenses and surfaces were extracted in solkane to remove any sol fraction from the samples.

Step 1: Preparation of PDMS lenses



Step 2: Preparation of PFPE mold



Step 3: Preparation of PFPE lenses



Figure 2.6. Preparation of PFPE lenses

To determine the radius of curvature of the prepared lenses, Equation 2.5 was used where R is the radius of curvature and d and h are horizontal and vertical distances respectively as indicated in Figure 2.7.

$$R = \frac{h}{2} + \frac{d^2}{8h} \quad \text{Equation 2.5}$$

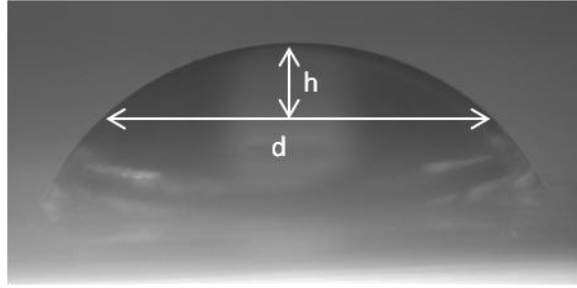


Figure 2.7. Optical side view image of the PFPE lens

Figure 2.8 is a simplified representation of the JKR experimental apparatus. The planar sheets were placed on the balance, and the lens was placed on the PDMS coated glass slide. Before the experiment, the lens was brought into contact with the sheet in order to find and focus on the contact area. Once in focus, the lens was raised just above the surface and the balance was tared. As soon as the stage was lowered, the video capture and the mass data collection were started simultaneously. When the maximum specified load was achieved, the stage motion was immediately reversed, and stopped only when the lens had pulled-off the surface. The contact radius was measured at specific time intervals from the video images to correspond with the collected mass data.

For some extracted samples, both surfaces of the planar elastomeric sheet were tested. For each elastomer, parameters such as motor speed (for the translating stage), and maximum load were varied in order to obtain the most reproducible results. Measurements were taken

during loading and unloading. For all samples except 1K, the maximum load was approximately 0.002 N. For 1K, the maximum load was approximately 0.005 N, as the 1K PFPE modulus was much higher than the other PFPE samples. For each elastomer, the test was repeated a minimum of three times to ensure reproducibility.

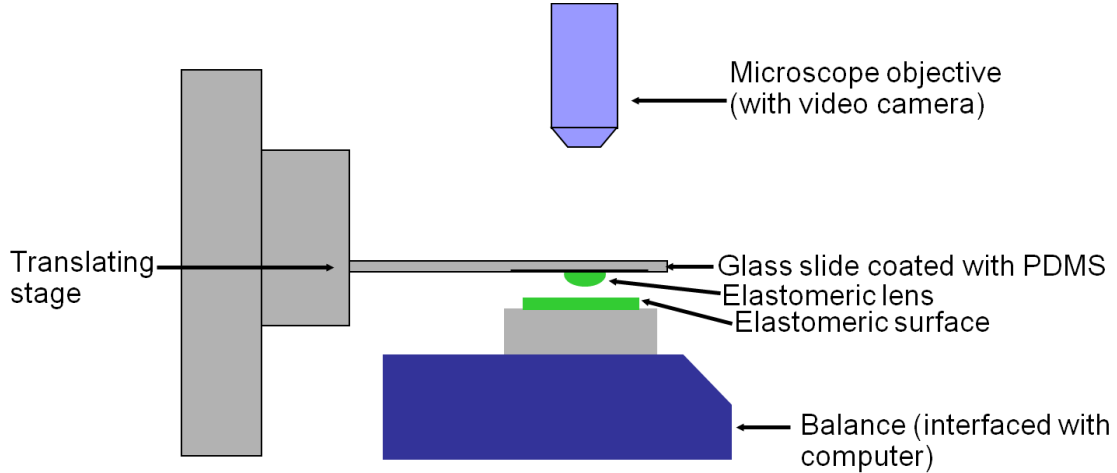


Figure 2.8. Schematic representation of the JKR experimental apparatus

To analyze the data, the linear form of the JKR Equation²¹ was used:

$$\frac{a^{\frac{3}{2}}}{R} = \frac{P}{Ka^{\frac{3}{2}}} + \left(\frac{6\pi W}{K} \right)^{\frac{1}{2}} \quad \text{Equation 2.6}$$

A plot of $a^{3/2}/R$ versus $P/a^{3/2}$ is a straight line. K was determined from the reciprocal of the slope and W was determined using Equation 2.6. The solid surface energy, γ_{sv} , of the elastomer is half the work of adhesion, i.e.

$$\gamma_{sv} = \frac{W}{2} \quad \text{Equation 2.7}$$

Young's modulus was also calculated from the JKR data using Equation 2.3. In the case of an incompressible solid where there is no change in volume upon deformation, $\nu \cong 1/2$, and so the relationship between E and K simplifies to:

$$E = \frac{9}{8}K \quad \text{Equation 2.8}$$

2.3.3.2 Results and Discussion

Figure 2.9 is a typical example of the JKR plots generated for the different elastomers. It displays the loading and unloading curves for the 3×4K PFPE elastomer. Most samples exhibited the adhesion hysteresis observed in Figure 2.9. The JKR theory does not predict hysteresis. This hysteresis has been attributed to numerous factors including chemical reactions between surface molecular groups, specific interactions between functional groups, the formation of entanglements across the interface, and the action of capillary forces due to ambient humidity.¹² As the unloading curves did not strictly follow JKR behavior, only the loading curves were used to estimate W and K.

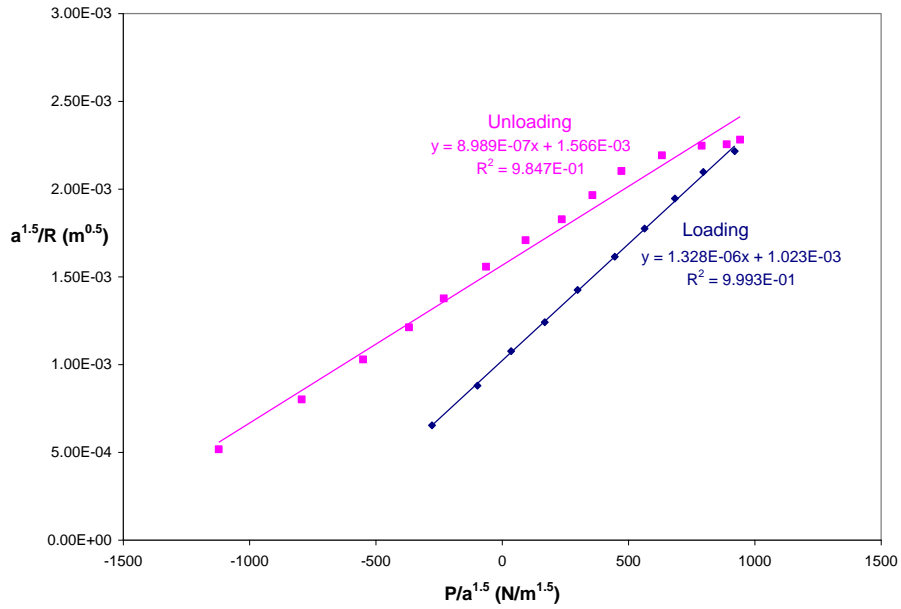


Figure 2.9. Plot of $a^{3/2}/R$ versus $P/a^{3/2}$ for 3x4K PFPE

The only samples that did not exhibit the adhesion hysteresis were the 4K PFPE samples extracted in solkane. Figure 2.10 shows that the loading and unloading curves superimposed for extracted 4K PFPE.

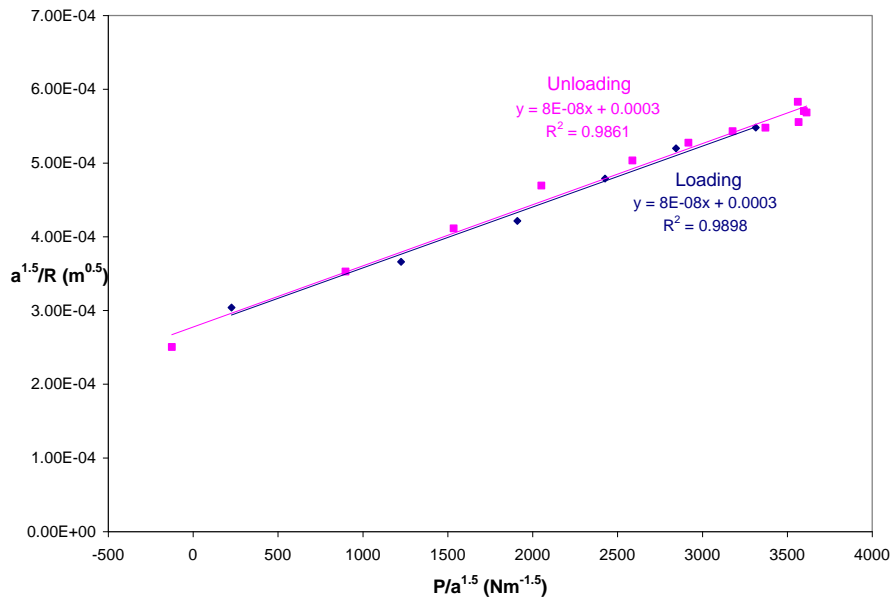


Figure 2.10. Plot of $a^{3/2}/R$ versus $P/a^{3/2}$ for extracted 4K PFPE

From the raw JKR data, E and γ_{sv} values were calculated using Equations 2.6-2.8. Table 2.2 shows the calculated results from samples tested without solvent extraction. Also shown in the table are tensile modulus values determined from Instron measurements and γ_c values determined previously using a Zisman analysis. Tensile moduli data are included to verify the accuracy of the JKR test. For most samples, the moduli were comparable from both techniques.

Table 2.2. Results for unextracted PFPE samples

PFPE DMA	Tensile Modulus (MPa) ^a	Young's Modulus, E (MPa) (JKR test)	Critical Surface Tension, γ_c , mNm ⁻¹ (Zisman analysis) ^b	Surface energy, γ_{sv} , mNm ⁻¹ (JKR test)
1K	99.9 ± 8.7	105.2 ± 6.4	14.6	10.1 ± 0.9
4K	7.7 ± 0.6	11.8 ± 0.9	8.1	13.1 ± 2.3
1K/ 4K Blend	33.6 ± 3.0	29.3 ± 1.8	10.3	7.5 ± 1.5
2×4K	2.0 ± 0.1	2.9 ± 0.1	15.1	18.4 ± 0.4
3×4K	0.8 ± 0.03	0.84 ± 0.02	16.3	19.5 ± 1.3

^a Instron measurements

^b γ_c data reproduced from reference ⁷

Table 2.3 displays the E and γ_{sv} values calculated for samples extracted in solkane. It is important to note that the values of E determined when both surfaces of the same material tested are in very good agreement, as the modulus is a bulk property and should be independent of the surface tested. There was, however, a general increase in the Young's modulus, E, for extracted samples when compared to Table 2.2. A small increase in E was

expected because the sol fraction can act as a diluent, weakening the elastomer.¹² However, Instron measurements of extracted PFPE samples did not correlate with the values obtained by the JKR tests. This could indicate a systematic error for this set of experiments. The surface energies of the two surfaces (nitrogen exposed and silicon exposed) were, however, significantly different, where the silicon-exposed surface had the higher surface energy. This was anticipated based on previously collected contact angle data. The N₂-exposed surface energies were not as low as indicated in Table 2.2 for unextracted samples. This could be a systematic error, though these surface energies for the N₂-exposed surface can be more easily explained in terms of the presence of CF₂ groups in the elastomer.

Table 2.3. Results for PFPE samples extracted in solkane

PFPE DMA (extracted)	Tensile Modulus (MPa) ^a	N ₂ -exposed surface		Si-exposed surface	
		E (MPa)	γ_{sv} , mNm ⁻¹	E (MPa)	γ_{sv} , mNm ⁻¹
1K/ 4K Blend (1:1)	39	49.6 ± 0.5	14.7 ± 1.1	51.8 ± 1.8	18.8 ± 2.3
4K	8.4	12.9 ± 0.4	17.0 ± 1.0	14.0 ± 0.7	21.9 ± 2.7
2×4K	2.4	3.4 ± 0.08	22.9 ± 0.5	3.5 ± 0.1	29.3 ± 3.9
3×4K	0.86	1.2 ± 0.1	17.6 ± 0.9	1.2 ± 0.04	23.1 ± 1.9

^a Instron measurements

For extracted 4K PFPE, no adhesion hysteresis was observed (Figure 2.10). This is not a common result reported in the literature for extracted samples. In many reported cases, there is an increase in adhesion hysteresis after extraction.^{12, 22, 23} Mason and collaborators studied the adhesion hysteresis in PDMS elastomers and noted that only lenses that had been

extracted in toluene displayed the hysteresis.¹² Based on their experiments, they concluded that extraction produces hysteresis by removing the free chains, which normally lubricate the interface, inhibiting the adhesion mechanism. In this case, there must be a different mechanism occurring for the PFPE elastomers.

The JKR test confirmed the low surface energies of the PFPE DMA elastomers, however for more accurate results, there needed to be an improvement in the preparation of the lenses. Recall from contact angle measurements that the surface the PFPE is cured against affects the surface properties. Since the PFPE lenses were cured in a PFPE mold, the surface properties were different from curing in N₂. As a result, the simple JKR equations employed to determine the surface energies would not have sufficed, since the two surfaces were different. An alternative in preparing the lenses would be to coat glass lenses with PFPE, ensuring that the PFPE is directly exposed to N₂ during curing.

Also, the effect of the dangling ends on the surface properties of the PFPE network is not well understood. One proposed study is to systematically incorporate known amounts of monofunctional PFPE chains to the PFPE precursor solution and study the effects on the surface energy and modulus. A similar study was carried out with PDMS elastomers; Amouroux *et al.* observed that the adhesion hysteresis increased with the amount of dangling chains supporting the conclusion that PDMS adhesion hysteresis is caused by bridging of the interface by pendant chains in the network.²⁴

2.3.4 Capillary Flow Experiments

2.3.4.1 Experimental Procedure

Masters were fabricated with the inverse channel pattern in the photoresist, SU-8 50. Each master contained 4 micro-channels with reservoirs of the following lengths: 2 mm, 5 mm, 10 mm and 20 mm. The cross-section of these channels was $25\ \mu\text{m} \times 25\ \mu\text{m}$. These masters were used to mold PFPE and PDMS channels. Once removed from the masters, inlet reservoirs (diameter = 0.6 cm) were punched out using a metal pipe. The channels were covered with another layer of the elastomer, and sealed using the physical adhesion between the two layers of PFPE (or PDMS). The glass micro-channels were isotropically etched, and as a result were not rectangular but had a trapezoidal cross-section (height $13.3\ \mu\text{m} \times 60\ \mu\text{m}$ top width $\times 35.9\ \mu\text{m}$ base width).

A test solution of polyethylene glycol dimethacrylate (PEG-DMA) containing 0.25 wt% rhodamine B dye was prepared. This monomer solution was used to closely reflect mold filling with polymerizable monomers. The PEG-DMA was used directly (containing 100 ppm MEHQ). The solution was dropped into the reservoirs of the dead-end channels (Figure 2.11). The start time, $t = 0$, was defined as the moment the solution came into contact with the channel inlet. The filling of the channel was monitored by fluorescence and optical microscopy. Distance versus time curves were generated for the different channel lengths and compositions.

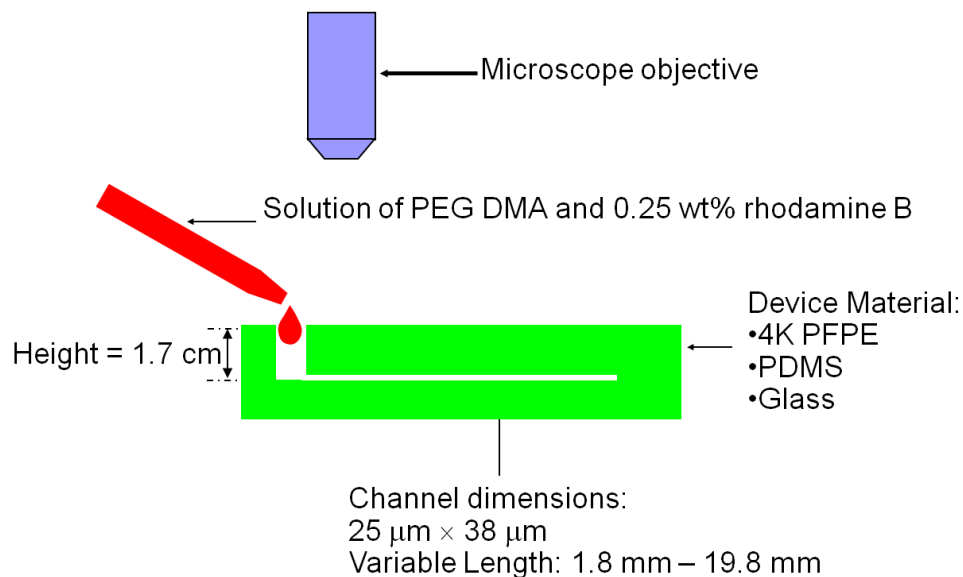


Figure 2.11. Experimental set-up for capillary flow experiment

2.3.4.2 Results and Discussion

Figure 2.12 shows the flow profile for capillary filling of dead-end PFPE microchannels. For all channel lengths, there was initially a high entrance velocity, which decreased as the interface traveled further into the channel. Also, it was observed that the longer the channel, the longer the time required to fill the channel. The filling occurred only from the open end of the channel meaning there was no bilateral filling as observed by others.^{15, 16}

Capillary flow in PFPE was compared to that in PDMS. For channels of the same dimensions ($25\mu\text{m} \times 25\mu\text{m} \times 6\text{ mm}$), the PEG solution filled the PDMS channel faster (Figure 2.12a). The PEG advancing contact angles were found to be $83.6^\circ \pm 2.0^\circ$ for PFPE and $80.5^\circ \pm 3.2^\circ$ for PDMS. PEG has a slightly higher advancing contact angle on PFPE, but the two values are within statistical error. In Table 2.4, gas permeabilities for PFPE and PDMS are presented. PDMS was slightly more gas permeable, but again the difference was

not very significant. Over time, it was observed that the rhodamine dye from the PEG solution slowly partitioned into the PDMS walls of the channel. The leaching of the dye may have affected the flow profile since it would have decreased the viscosity of the PEG solution.

The capillary filling of glass microchannels was also observed. The data was not included in Figure 2.12b because for a glass channel of similar dimensions (recall that the shape of glass channels were different), it took over two weeks to fill. In fact, it took days for the liquid to even begin to penetrate the channel. This experiment however, confirms that the permeability of the channel material is a very important factor in the rate of capillary filling.

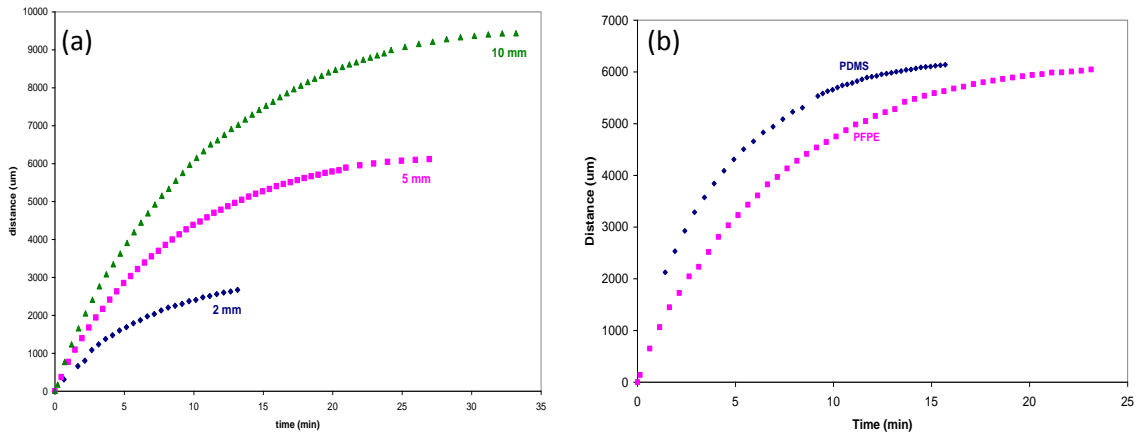


Figure 2.12. (a) Advancing liquid-air interface in dead-end PFPE micro-channels of different lengths and (b) Advancing liquid-air interface in dead-end PFPE and PDMS microchannels ($25 \mu\text{m} \times 38 \mu\text{m} \times 6 \text{mm}$)

Table 2.4. Permeability of PFPE compared with PDMS²⁵

Permeant	Permeability [cm ³ (STP).cm]/[(cm ²).s.cmHg]	
	PFPE	PDMS
N ₂	260	253
O ₂	486	549
CO ₂	1630	2700

It should be noted that there were numerous problems with reproducibility during the course of these experiments. Initially, deionized PEG solutions were used but under the microscope objective, the solutions began to polymerize while filling the channel, changing the viscosity and thus the flow profile. Even after changing to inhibited solutions, flow profiles were not reproducible from experiment to experiment. One of the possible reasons for this is that the region under the microscope got progressively hotter with each experiment, thus changing the temperature which will affect both the gas permeability and solution viscosity. Another factor not monitored during the experiments was the humidity, which can potentially affect the permeability.

The spontaneous filling of PFPE and PDMS dead-end micro-channels has been confirmed by optical and fluorescence microscopy. Difficulties with reproducibility prevented the data from being used to predict flow behavior.

2.4 Conclusion

Fundamental studies on the properties of perfluoropolyether elastomers were conducted. Even though JKR studies have previously been used to study different elastomers, such as PDMS, these are the first JKR studies on the PFPE elastomers. The

studies confirmed the low surface energy of PFPE. Furthermore, it was found that the surface properties were dependent on molecular weight between crosslinks and solvent extraction. Issues with PFPE lens preparation likely led to some of the error observed in the measurements. The use of glass beads as supports for the PFPE lenses would likely improve reproducibility. The capillary flow behavior in PFPE dead-end microchannels was also studied. For a PEG monomer liquid, both PFPE and PDMS exhibited similar capillary flow properties, however as many organic compounds partition into PDMS it is not as suitable as PFPE with all solvent systems.

2.5 References

1. Gratton, S. E. A.; Williams, S. S.; Napier, M. E.; Pohlhaus, P. D.; Zhou, Z.; Wiles, K. B.; Maynor, B. W.; Shen, C.; Olafsen, T.; Samulski, E. T.; DeSimone, J. M. *Acc. Chem. Res.* **2008**, 41, 1685-1695.
2. Merkel, T.; Herlihy, K.; Nunes, J.; Orgel, R.; DeSimone, J. M. *Langmuir* **2009**, in press.
3. Rolland, J. P.; Maynor, B. W.; Euliss, L. E.; Exner, A. E.; Denison, G. M.; DeSimone, J. M. *J. Am. Chem. Soc.* **2005**, 127, 10096-10100.
4. Maynor, B. W.; LaRue, I.; Hu, Z.; Rolland, J. P.; Pandya, A.; Fu, Q.; Liu, J.; Spontak, R. J.; Sheiko, S. S.; Samulski, R. J.; Samulski, E. T.; DeSimone, J. M. *Small* **2007**, 3, 845-849.
5. Hampton, M. J.; Williams, S. S.; Zhou, Z.; Nunes, J.; Ko, D.-H.; Templeton, J. L.; Samulski, E. T.; DeSimone, J. M. *Adv. Mater.* **2008**, 20, 2667-2673.
6. Kelly, J.; DeSimone, J. M. *J. Am. Chem. Soc.* **2008**, 130, 5438-5439.
7. Hu, Z. Novel perfluoropolyethers as fouling-release coatings. PhD, The University of North Carolina, Chapel Hill, 2009.
8. Fox, H. W.; Zisman, W. A. *J. Colloid Sci.* **1950**, 5, 514-531.
9. Chaudhury, M. K.; Whitesides, G. M. *Langmuir* **1991**, 7, 1013-1025.
10. Johnson, K. L.; Kendall, K.; Roberts, A. D. *Proc. R. Soc. London A* **1971**, 324, 301-313.
11. de Gennes, P.-G.; Brochard-Wyart, F.; Quere, D., *Capillarity and Wetting Phenomena: Drops, Bubbles, Pearls, Waves*. Springer: New York, 2004; p 63.
12. Mason, R.; Emerson, J.; Koberstein, J. T. *J. Adhesion* **2004**, 80, 119-143.
13. Washburn, E. W. *Phys. Rev. Lett.* **1921**, 17, 273.
14. Bankoff, S. G. *AIChE J.* **1958**, 4, 24-26.
15. Dovgyallo, G. I.; Migun, N. P.; Prokhorenko, P. P. *J. Eng. Phys. Thermophys.* **1989**, 56, 395-397.
16. Pesse, A. V.; Warriar, G. R.; Dhir, V. K. *Int. J. Heat Mass Transfer* **2005**, 48, 5150-5165.
17. Heule, M.; Schell, J.; Gauckler, L. J. *J. Am. Ceram. Soc.* **2003**, 86, 407-12.
18. Kim, E.; Xia, Y.; Whitesides, G. M. *Nature* **1995**, 376, 581-584.
19. Kim, E.; Xia, Y.; Whitesides, G. M. *J. Am. Chem. Soc.* **1996**, 118, 5722-5731.
20. Priola, A.; Bongiovanni, R.; Malucelli, G.; Pollicino, A.; Tonelli, C.; Simeone, G. *Macromol. Chem. Phys.* **1997**, 198, 1893-1907.

21. Vorvolakos, K.; Chaudhury, M. K. *Langmuir* **2003**, 19, 6778-6787.
22. Perutz, S.; Kramer, E. J.; Baney, J.; Hui, C. Y.; Cohen, C. J. *J. Polym. Sci., Part B: Polym. Phys.* **1998**, 36, 2129-2139.
23. Silberzan, P.; Perutz, S.; Kramer, E. J.; Chaudhury, M. K. *Langmuir* **1994**, 10, 2466-2470.
24. Amouroux, N.; Leger, L. *Langmuir* **2003**, 19, 1396-1401.
25. Rolland, J. P. Functional perfluoropolyethers for Novel Applications. PhD, The University of North Carolina, Chapel Hill, 2005.

Chapter 3

Electrical Manipulation of PRINT particles

3.1 Specific research objectives

Electric (E) field manipulation of micron-sized particles was investigated in this research to assemble and drive particle motion using two approaches: dielectrophoresis and electrophoresis. As described in Chapter 1, E fields represent a valuable tool for the external manipulation of colloids. Given the particle fabrication control of the PRINT process, uniquely designed particles can be studied and manipulated by such fields. With the exception of a few biological systems, such as cells, virus particles and bacteria,¹⁻⁵ the effect of particle shape has not been well-studied in E fields. Thus, the E-field induced assembly and motion of highly shape-specific and anisotropic polymeric particles were studied.

Dielectrophoretic studies were conducted on micron-sized monodisperse anisotropic polymer particles, with disc, rod, hexnut and boomerang shapes. Investigations were focused on aqueous suspensions of these PRINT particles when subjected to alternating current (AC) E fields. A coplanar electrode configuration, similar to that used by Velev *et al.*, was employed.⁶⁻⁸ Particle assemblies were monitored with fluorescence microscopy. Particle motion in DC E fields was also investigated. Both rigid rod and deformable disk particles were driven in confined geometries due to electroosmosis.

3.2 Dielectrophoretic Assembly of PRINT Particles

3.2.1 Particle Fabrication and Characterization

Unless otherwise stated, the following reagents were purchased from Sigma-Aldrich and used as received: 2,2-diethoxyacetophenone (DEAP), 2-aminoethyl methacrylate hydrochloride (AEM), fluorescein *o*-acrylate, dimethyl sulfoxide (DMSO), hexadecyltrimethylammonium bromide (CTAB). Trimethylolpropane ethoxylate (14/3

EO/OH) triacrylate ($M_n = 912$ g/mol) was de-inhibited using adsorption alumina (Fisher). 1-vinyl-2-pyrrolidinone (VP) was distilled prior to use. 2-propanol (Fisher) and acetone (Fisher) were both filtered with a 0.2 μm nylon filter (Millipore) prior to use. Cyanoacrylate adhesive (Zap CA PT-08, Pacer Technologies) was used as received. The perfluoropolyether (PFPE) prepolymer resin (Fluorocur[®], Liquidia Technologies, Inc.) was mixed with 0.1% (w/v) DEAP photoinitiator before use. Double-sided adhesive slide separators (SS1X9, Grace BioLabs) were used with standard 1x3" glass slides (Fisher Scientific) for preparation of the dielectrophoresis (DEP) cell. The untreated side of poly(ethylene terephthalate) (PET) sheets (Melinex 453, DuPont) was used for mold support and for monomer distribution and removal.

Monomer composition: Particles were designed to have a cross-linked architecture with minimal swelling in aqueous solutions, and miscible with the other functional monomers. The trifunctional monomer, trimethylolpropane ethoxylate triacrylate, was selected because of the amphiphilic nature of the ethylene oxide repeat unit and its high functionality. Fluorescein *o*-acrylate was incorporated into the hydrogel matrix for fluorescence analysis. AEM was added to provide the particle with a positive zeta potential, and also to impart reactive moieties for further chemical functionalization if necessary. The photoinitiator, DEAP, was used to initiate the photopolymerization in the presence of UV radiation. The PFPE molds were filled as described in Chapter 2 and elsewhere⁹⁻¹¹ and the monomer solution was converted to the hydrogel upon UV curing in the presence of nitrogen. Particle arrays were harvested onto polycyanoacrylate.

Particle purification: After harvesting, particles were purified to remove residual polycyanoacrylate and other unwanted debris by repeatedly rinsing with acetone. Initially,

particles were pelleted out of solution by centrifugation (5 minutes, 137G). The supernatant was then decanted and the particles were resuspended by vortexing gently for 1 minute. This process was repeated at least 5 times. Particles were then gravimetrically filtered to remove any debris. Finally a 100 μ L aliquot of the particle slurry in acetone was placed in a preweighed eppendorf tube and was dried *in vacuo* to determine the concentration of particles.

Sample preparation: In order to avoid particle aggregation, particles were never completely dried. Instead, particle samples were prepared by combining 1.0% (w/v) CTAB solutions with particle/acetone slurries. The solutions were then placed under vacuum to remove the excess acetone. Final particle concentrations were as follows: hexnuts were 5 mg/mL, rods were 10 mg/mL, disks were 20 mg/mL, and the boomerangs were 10 mg/mL. For DEP experiments, aliquots of 11 mL were placed in the sample cell. Sample pH was between 5.5-6.5. No buffer was added.

The resulting PRINT particles were uniform in size and shape and were relatively stable in aqueous solution containing CTAB. The tops of the particles were flat while the bottoms of the particles were slightly concave due to a meniscus that was formed during the mold filling process. Scanning electron microscopy (SEM) images of the particles are shown in Figure 3.1 with corresponding optical fluorescence images. Particle sizes were calculated using PCI software with SEM images.

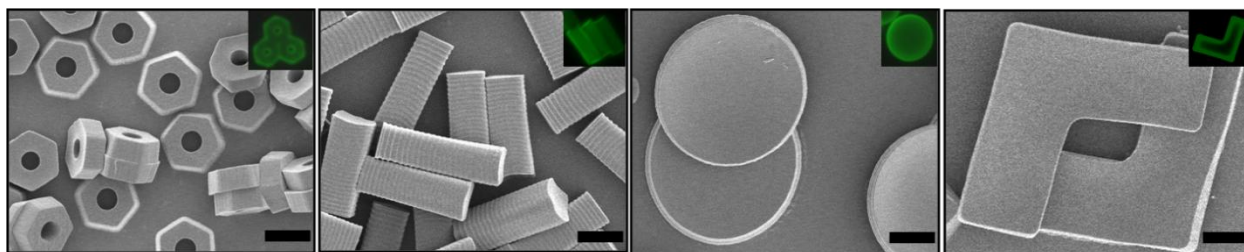


Figure 3.1. Representative scanning electron micrograph and fluorescent images of (from left to right) $2.5 \times 1 \mu\text{m}$ hexnut particles with $1 \mu\text{m}$ hole, $1.6 \times 1.6 \times 5 \mu\text{m}$ trapezoidal particles, $6.5 \times 0.8 \mu\text{m}$ disk-shaped particles and $9.6 \times 3.4 \times 1 \mu\text{m}$ boomerang-shaped particles. Scale bars represent $2 \mu\text{m}$.

3.2.2 Experimental Design and Set-up

The electrodes were fabricated following various procedures described elsewhere.⁶⁻⁸ Briefly, glass slides fit with a 1-2 mm wide adhesive mask were coated with 70-90 nm Pd/Au using a sputter coater (Model 108 Auto Sputter Coater, Cressington Scientific Instruments) to form two planar electrodes. An adhesive circular spacer was placed over the electrodes. A 10-11 μL aliquot of colloidal particle solution was placed on the surface of the slide and was sealed in place using a cover slip (1.5 Gold Seal). The alternating electric field was produced by a wave function generator (Model 180 Function Generator, Wavetek) and then amplified (6824A DC Power Supply Amplifier, Hewlett Packard). Field intensities ranged from 10-50 V with square wave frequencies between 500-5000 Hz. Experiments were typically run at 40 – 50 V and 500 Hz. The dielectrophoretic cell is illustrated in Figure 3.2.

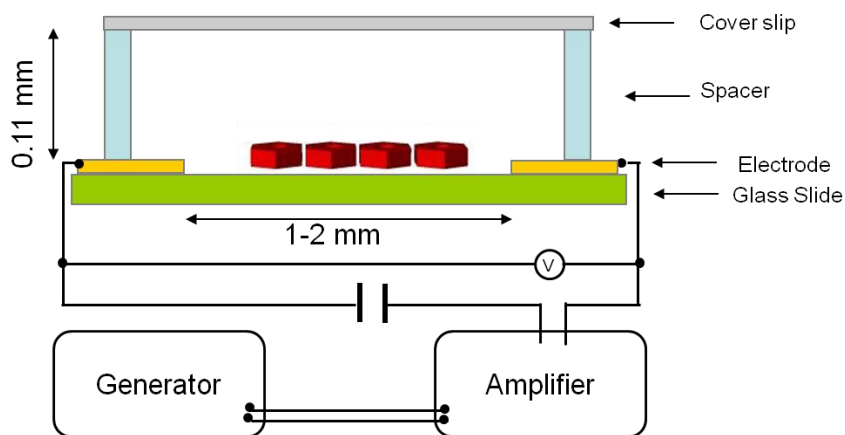


Figure 3.2. Illustration of the dielectrophoretic cell

Imaging: Individual particles were imaged using a Hitachi S-4700 scanning electron microscope. The samples were dried from acetone slurry at room temperature in air and then coated with Pd/Au (3-5 nm) in the sputter coater. Particle alignment, packing, and crystallization were observed using a Zeiss Axioskop 2 MAT incident light microscope fitted with an AxioCam MR digital camera.

Turbidity experiments: Particle samples (5-20 mg/mL) were prepared in 0.2, 1.0, and 5.0% (w/v) aqueous CTAB solution. A cuvette (100 μ L, QS), with a path length of 1 cm, containing the particle sample was then vortexed and placed in a plate reader (Spectra Max M5, Molecular Devices). A kinetic experiment was performed at 490 nm, reading absorbance every 30 s for 1 hour at 22 $^{\circ}$ C. All experiments were repeated three times to establish reproducibility. The turbidity, τ , defined as the attenuation of the light beam by scattering when passing through a sample, was determined from Equation 3.1 below, where I_o is the incident intensity of light, I_t the transmitted intensity, and l the optical path length.

$$\tau = l^{-1} \ln(I_o/I_t) \quad \text{Equation 3.1}$$

3.2.3 Results and Discussion

In colloidal systems, unless strategies are employed to stabilize the particles either electrostatically or sterically, there is a tendency for particles to aggregate due to attractive van der Waals forces. This was observed when the PRINT particles were suspended in water, as they aggregated rapidly in the absence of stabilizer. In order to hinder aggregation, increasing amounts of CTAB were added to the particle suspension. Generally, as CTAB concentration increased, particle stability increased (Figure 3.3). In this manner, we were able to determine conditions for colloidal stability within the timeframe of the dielectrophoretic experiments. Turbidity experiments showed that 1.0% (w/v) CTAB was adequate to slow particle aggregation and sedimentation of all the particle sizes studied sufficiently for our purposes (~5-10 minutes) (Figure 3.4).

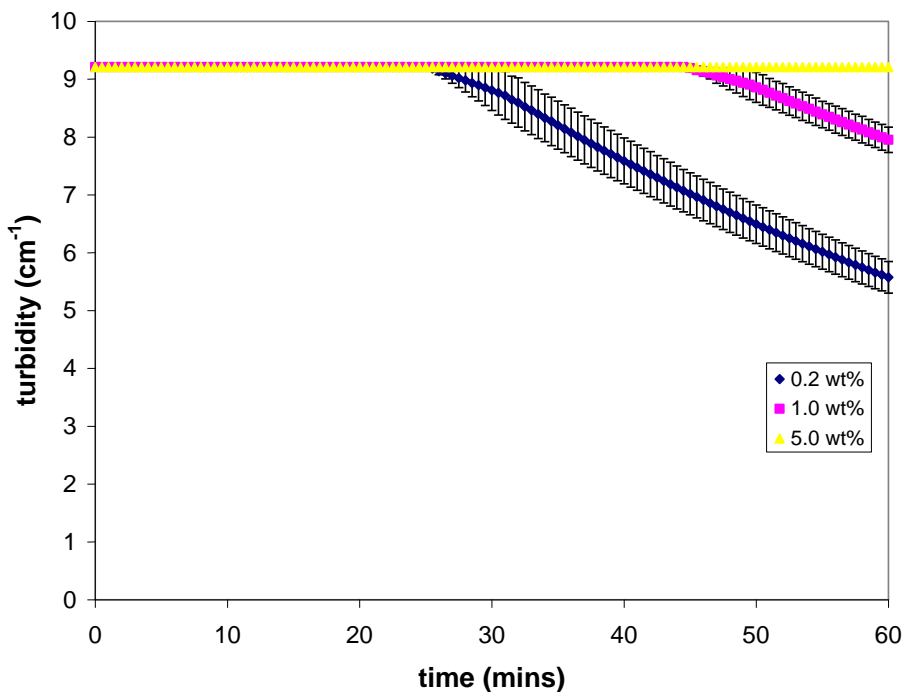


Figure 3.3. Turbidity measurements on 5 mg/mL hexnut suspensions at three CTAB concentrations: 0.2 wt%, 1.0 wt% and 5.0 wt%.

Observation by fluorescence microscopy revealed individually suspended particles, however, a small number of aggregates were observed in solution. In these aggregates, the rods, hexnuts, and disks packed with their major axes parallel to one another. These aggregates typically settled out of solution much faster than individual particles. The trimethylolpropane ethoxylate triacrylate polymer used to synthesize the particles is denser than water with an estimated specific gravity of 1.2-1.3 at 25 °C, and, in general, the sedimentation rate for the particles depended on their size and shape: 40-50 minutes for the rods and hexnuts, 10-30 minutes for the boomerangs and disks. In addition, the limited mobility of the aggregates affected their response to the applied AC field; this was especially prevalent for the larger particles. Particle properties, including the estimated aggregation threshold times, are presented in Table 3.1.

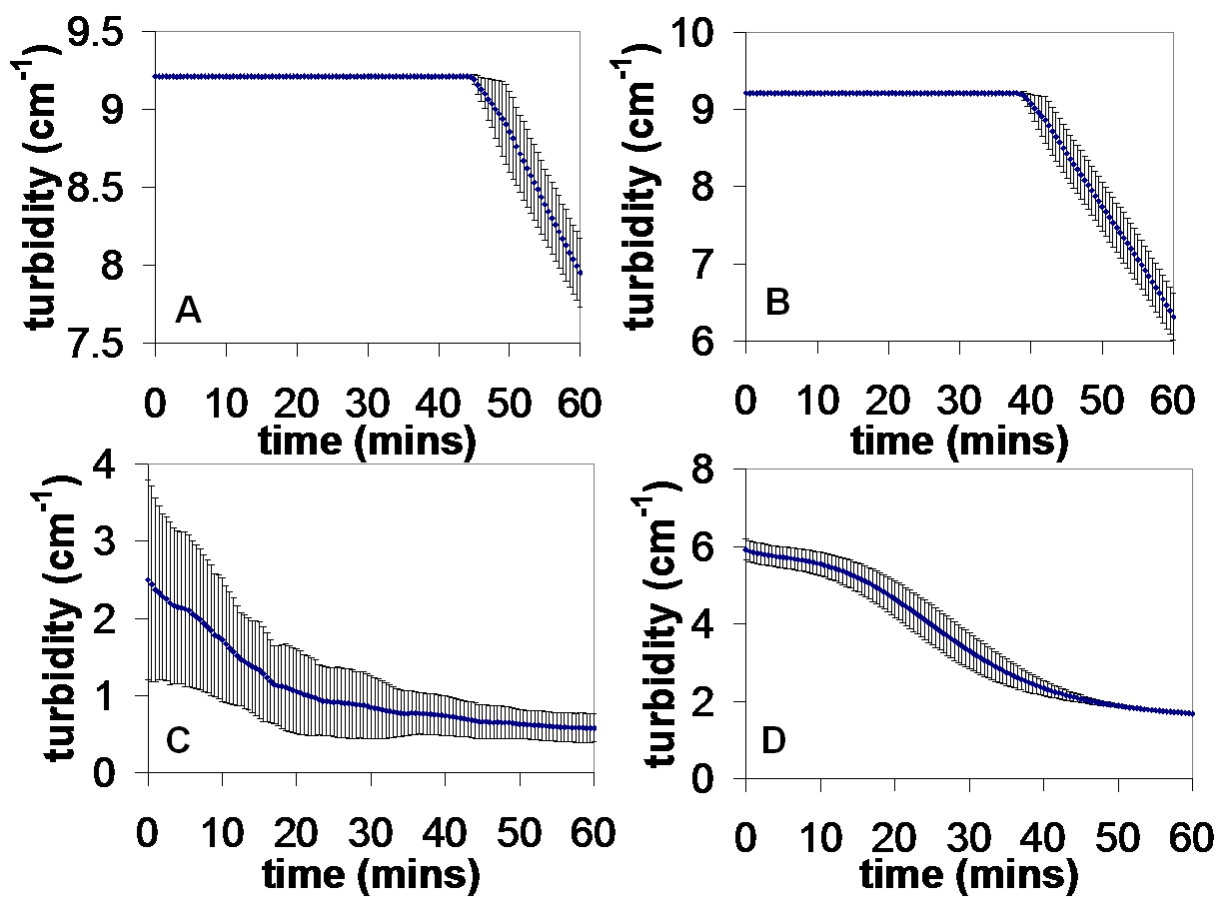


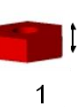

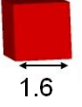
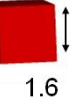
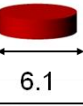
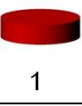

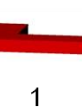


Figure 3.4. Turbidity curves for aqueous particle suspensions containing 1.0 wt% CTAB where A) 5 mg/mL hexnut suspension, B) 10 mg/mL rod suspension, C) 20 mg/mL disk suspension and D) 10 mg/mL boomerang suspension

Table 3.1. Particle properties

Particle	Primary Axis (μm)	Secondary Axis (μm)	Tertiary Axis (μm)	Surface Area (μm^2)	Volume (μm^3)	S/V	Aggregation Threshold (minutes)
Hexnut	 2.9	 2.5	 1	21	4.6	4.56	44.5
Rod	 5	 1.6	 1.6	37.1	12.8	2.89	39
Disk	 6.1	 1	-	82.7	26.5	3.12	-
Boomerang	 -	 1	-	146	53.7	2.71	14

Dielectrophoretic alignment of particles in solution occurred when a nonuniform AC field was applied across two planar electrodes (Figure 3.2). As expected for positive dielectrophoresis, when the field is turned on, the particles become polarized and are directed towards the region with the highest field intensity – the glass region between the electrodes. During this step, particles experienced a torque and were observed to reorient to a new stable position from their initial random orientation relative to the field. This electroorientation results in the alignment of particles with their longest axis parallel to the applied field ($\theta = 0^\circ$), consistent with observations made by others.^{5, 12} Additionally, in the majority of cases, the particles' second major axis (if there was one) was perpendicular to the normal of the plane of the electrode ($\phi = 90^\circ$), or in other words, the particles laid flat on the surface of the glass electrode. Once the particles aligned with the field, they began to link together forming

chains. This phenomenon is thought to be due to the interactions between the dipoles induced in the particles.¹³ Figure 3.5 shows the response of each of the particle shapes to the nonuniform AC field. In each case, there was a definite change as the particle suspension changed from random to an ordered arrangement.

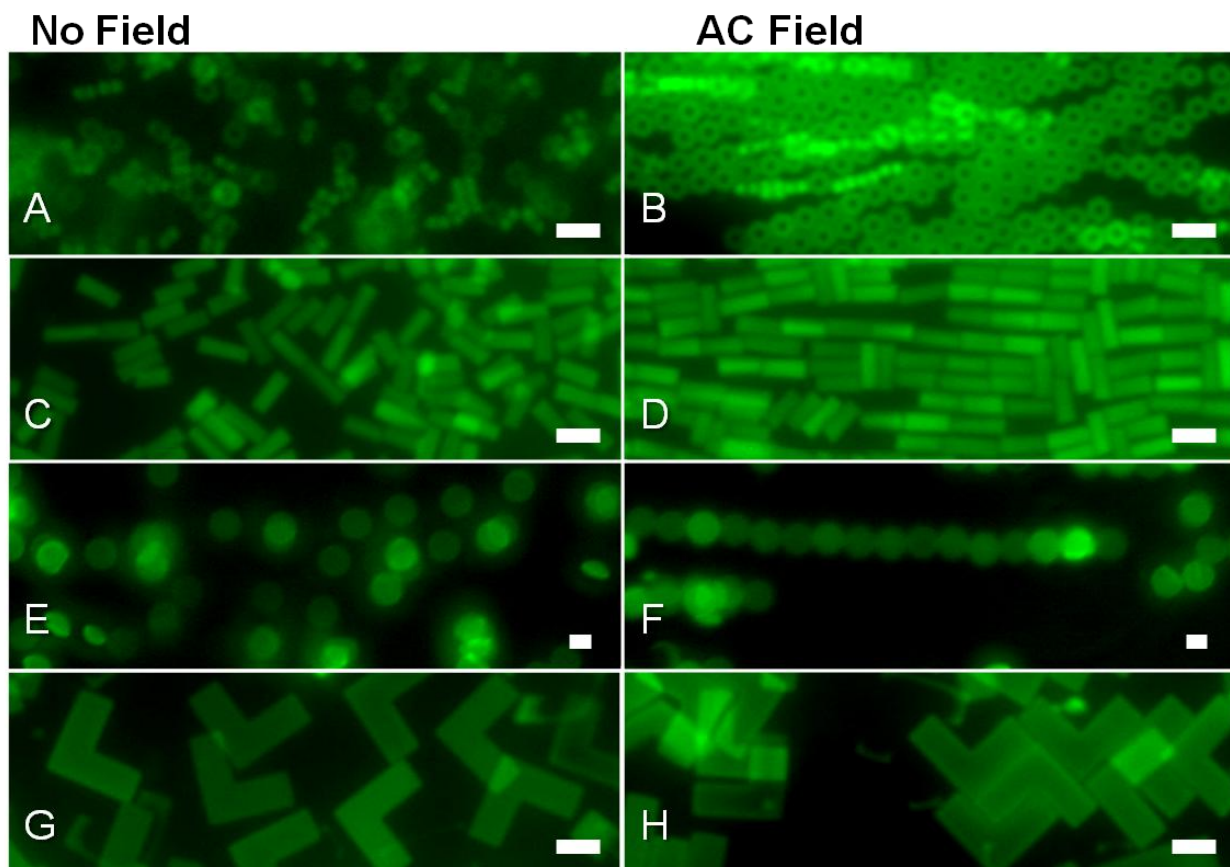


Figure 3.5. Representative fluorescence images of randomly dispersed (A, C, E, G) and electrically aligned (B, D, F, H) particles with a 5 μm scale bar. Particles shown were aligned at 40-50 V and 500 Hz.

Particle chains formed rapidly (10-20 seconds) and continued to grow as long as the field was on. The initial chaining event for the rod particles is shown in Figure 3.6. The speed of chaining appeared to be a function of the size of the particle with the smaller particles (hexnuts and rods) forming chains the fastest while the disks formed chains much

slower and the boomerangs formed no discernable chains. Large chains of particles then moved slowly towards each other and formed large crystalline structures. If the AC field was removed after being applied for only a short period (10-20 seconds), particles returned to a random state. However, if the field was applied for a longer period of time, aggregation and sedimentation of the particles began to take place. This trapped some particles in permanent chains while bound to the surface of the glass cell.

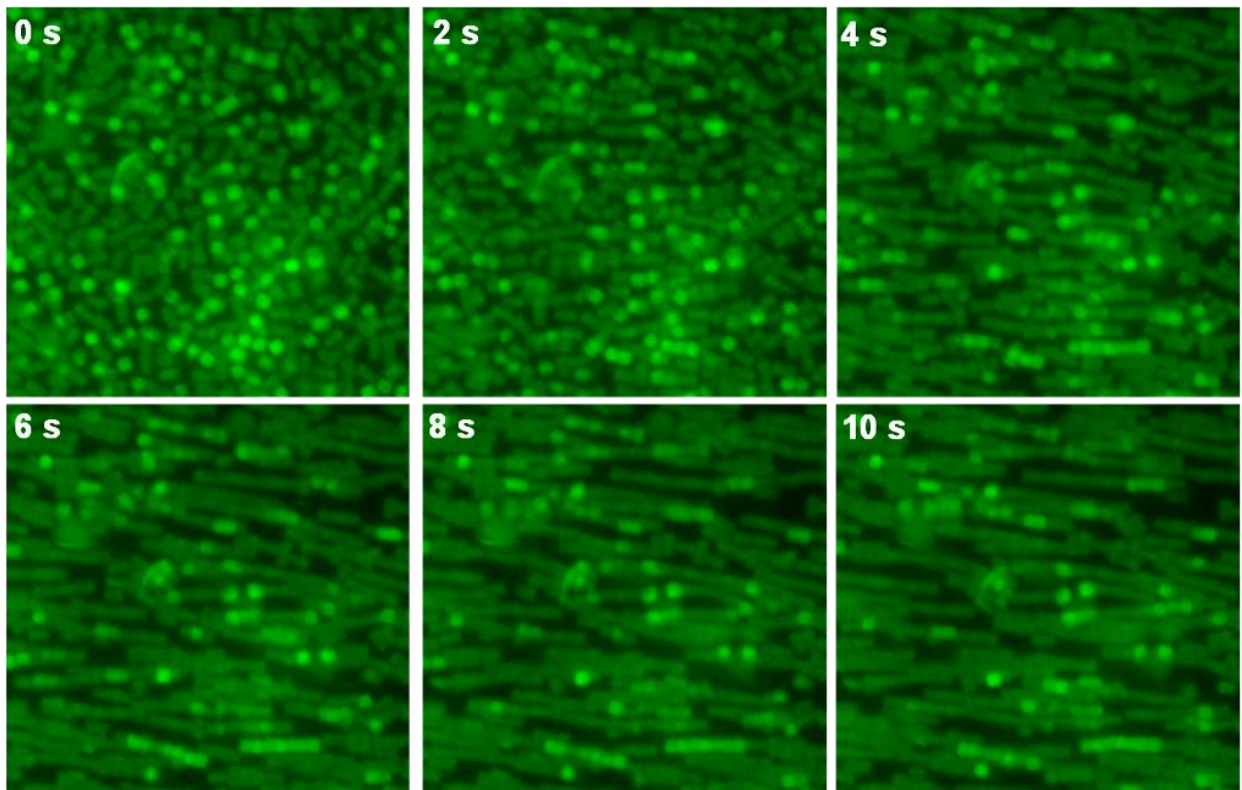


Figure 3.6. Evolution of chains as a function of time for rod particles, where each frame was taken every 2 seconds after application of the E field.

Hexnut shaped particles, the smallest of the four particles shapes, aligned rapidly with the applied field. The principle axis of the hexnut particle was $2.9 \mu\text{m}$ from point-to-point (Table 3.1). The particles initially formed chains in this fashion. It was interesting, however,

to observe that the majority of hexnut chaining took on a slightly different conformation with the flat edges of the particles touching one another rather than just the tips, thus the second axis of the hexnuts (2.5 μm) was found to be aligned parallel to the applied field. This effect is most likely driven by the need to maximize surface interactions. That is, it is more energetically favorable for the chains to undergo a slight modification from the most dielectrophoretically stable conformation to one that is slightly less favorable because of the stability gained from the dramatic increase in surface interactions. Chains of hexnuts had two orientations. The primary orientation was with the particles parallel to the AC field ($\theta = 0^\circ$ for secondary axis) and perpendicular to the normal of the electrode plane ($\phi = 90^\circ$). The second, and less common orientation was with particle chains parallel to the AC field and parallel to the normal of the electrode ($\phi = 0^\circ$). While this chain orientation was regularly observed, the chains typically collapsed back into the plane of the electrode. Over time, chains of hexnut particles moved towards each other and came into contact. This process eventually formed large crystals of particles in a hexagonal close-packed pattern.

Rod shaped particles, like the hexnut particles, responded rapidly to the dielectrophoretic force and aligned with their primary axis parallel to the AC field (Table 3.1). As particles began to move through solution, some particles ($9\% \pm 1\%$) were trapped perpendicular to the AC field ($\theta = 90^\circ$, $\phi = 90^\circ$). Very few particles were observed with the long axis parallel to the normal of the electrode plane. Long chains of the rods formed almost immediately parallel to the AC field. As with the hexnuts, the chains of rods came together to form crystals. Unlike the hexnuts, the rods formed a rectangular lattice (Figure 3.7B). It is interesting to note that in the absence of any defects (perpendicular particles) individual particles within adjacent chains came into registry with one another in a smectic-

like manner. This effect may be driven by the areas of high field intensity at the corners of the particles.

The disk shaped particles rapidly settled out of solution and sat with their face flat on the glass surface in the absence of an AC field. Once settled, the particles became difficult to move even at higher voltages. The circular nature of the disk shaped particles gives them only one major axis (Table 3.1). This is different from the particles mentioned above which both have at least two major axes that aligned with the applied field. Alignment of the disc shaped particles manifested itself with the particles laying flat on the surface of the glass ($\theta = 0^\circ$, $\phi = 90^\circ$). In comparison to the smaller particles the disks slowly (30-60 seconds) formed short chains. The chains had trouble moving and therefore crystallization was only observed a few times. The crystals that formed were hexagonal close-packed in nature (Figure 3.7C).

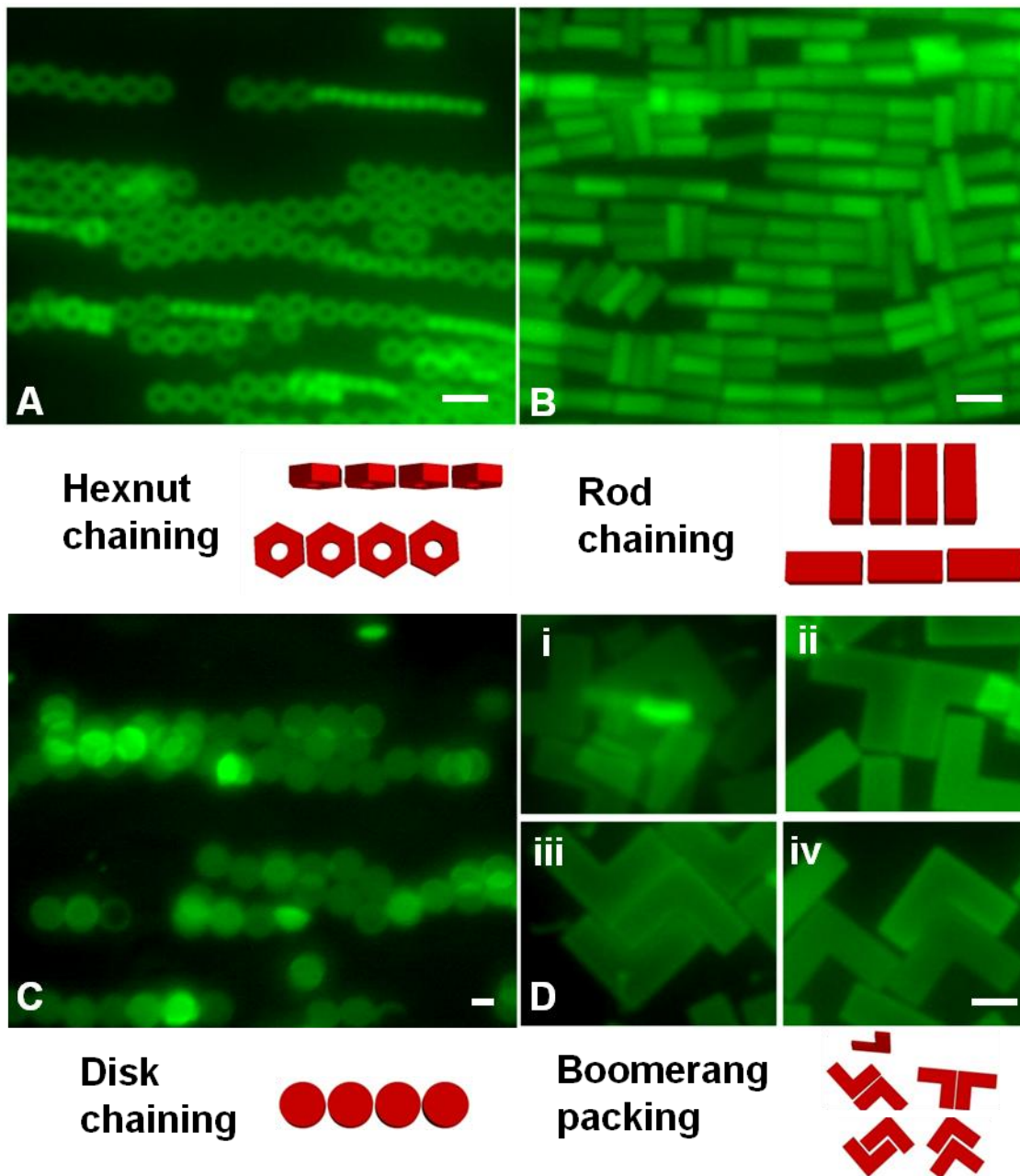


Figure 3.7. Fluorescence images of aligned particles with applied AC electric field. 5 μm scale bar. Particles shown were aligned in a 40-50 V field at 500 Hz.

Boomerang shaped particles exhibited unique behavior in comparison to the other particle shapes. Similar to the other shapes, boomerangs typically laid flat in the plane of the electrode ($\phi = 90^\circ$). But unlike the other shapes, the boomerangs had no preferential

orientation with respect to θ , which may be due to the symmetry in the particle shape (Table 3.1). Interestingly, the few boomerangs that did stand straight up aligned with the applied AC field ($\theta = 0^\circ$, $\phi = 45^\circ$). These particles eventually tipped and fell back into the plane of the electrode ($\phi = 90^\circ$). Although the boomerangs did not align in the presence of an applied AC field, they did adopt a number of interesting orientations in clusters (Figure 3.7 D i-iv). These clusters eventually grew large enough that some directionality was observed in which the clusters were aligned with the applied field. Rapid sedimentation coupled with the unique shape of the particles prevented large-scale crystallization.

All particle assemblies covered the entire glass surface between the electrodes. Low magnification images of particle assemblies are shown in Figure 3.8.

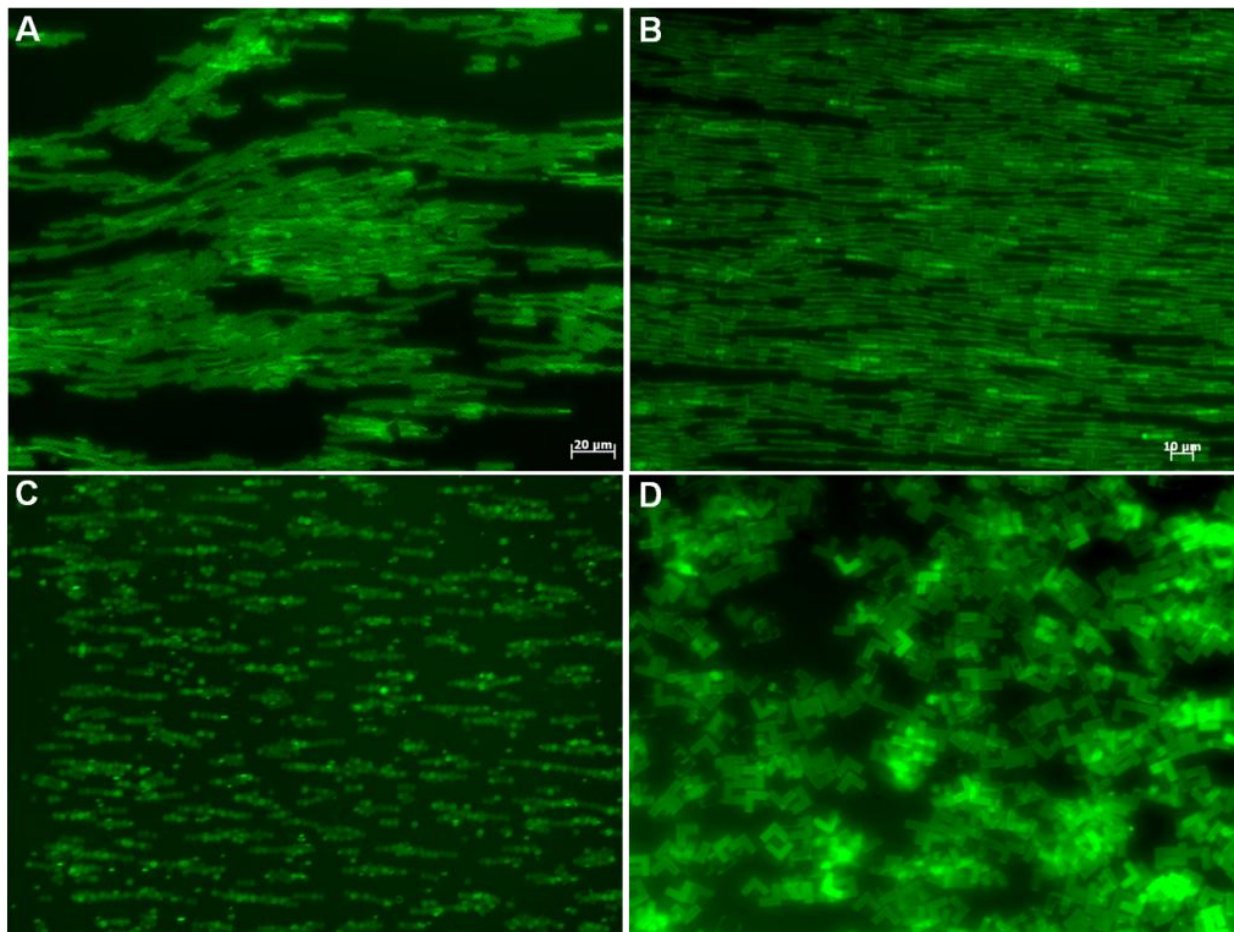


Figure 3.8. Low magnification fluorescence images of particle alignment in nonuniform AC electric field for (A) hexnut, (B) rod, (C) disk and (D) boomerang shaped particle suspensions.

While this study has focused primarily on crystallization of particles between the electrodes, crystallization on the electrodes was also observed. This type of crystallization was only observed for the hexnut shaped particles. These particles formed small hexagonal close-packed clusters that laid flat on the electrode surface (Figure 3.9A). A large portion of the individual hexnut particles found on the electrode were oriented perpendicular to the surface of the electrode but had no significant preference for orientation otherwise. The rod and disk shaped particles did not form crystals but did orient themselves perpendicular to the

plane of the electrode (Figure 3.9B). Boomerang shaped particles did not exhibit any preferential alignment or crystallization on the electrode.

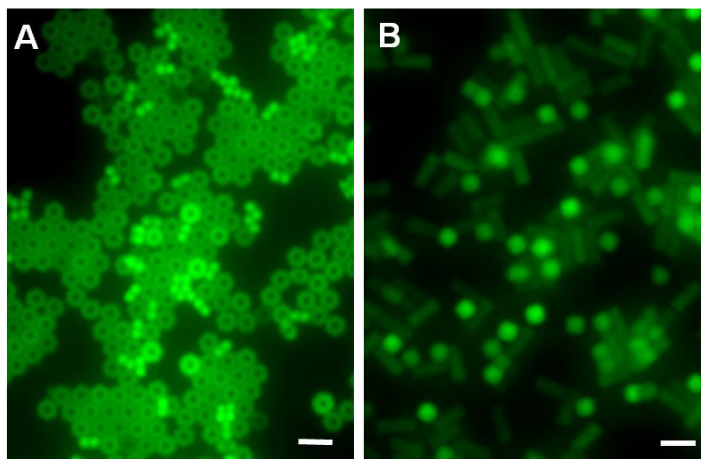


Figure 3.9. Fluorescence image of (A) hexnut and (B) rod shaped particles with applied AC electrical field on the electrode. Scale bars represent 5 μm .

One attempt was made to use the DEP cell to assemble particles in a non-aqueous solvent. Rod particles were suspended in 1-vinylpyrrolidone, VP (containing 1 wt% DEAP photoinitiator). The particles were allowed to chain and crystallize in the nonuniform AC field for at least 30 minutes. The cell was then placed in a UV chamber to polymerize the VP; the field was kept on during polymerization. Figure 3.10A is a fluorescence image of the composite. The particles did not initially disperse well in the VP, so a fairly large amount of random aggregates were present that disrupted the overall crystallization. The composite film was removed and sectioned. At the base of the film, the rod particles were found lying on their sides, as expected (Figure 3.10B).

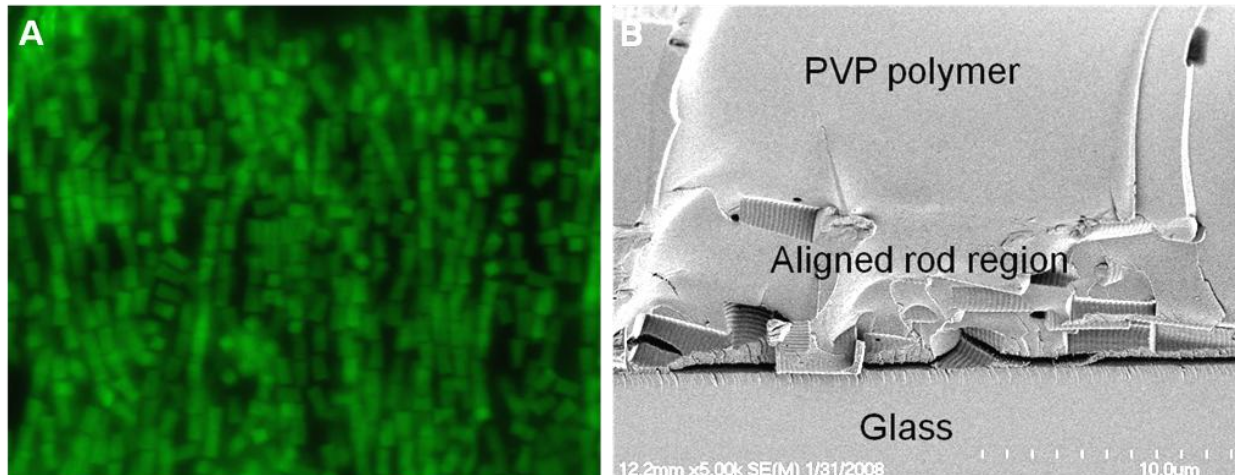


Figure 3.10. PVP/PEG composite formed in DEP cell

3.3 Particle Electrophoresis in Confined Geometries

3.3.1 Particle Fabrication and Characterization

Unless otherwise stated, the following reagents were purchased from Sigma-Aldrich and used as received. The photoinitiator was 2,2-diethoxyacetophenone (DEAP) and the charged monomers were 2-carboxyethyl acrylate (CEA) and 2-aminoethyl methacrylate hydrochloride (AEM). The surfactants used were hexadecyltrimethylammonium bromide (CTAB) and Pluronic (Pluronic F68). Trimethylolpropane ethoxylate (14/3 EO/OH) triacrylate (PEG₉₁₂TA; $M_n = 912$ g/mol) and poly(ethylene glycol) dimethacrylate (PEG₁₀₀₀DMA; $M_n = 1000$ g/mol) were de-inhibited using adsorption alumina (Fisher). Poly(vinyl alcohol) (PVOH, $M_n = 22,000$ g/mol) was used for deformable disk particle harvesting. Cyanoacrylate adhesive (Zap CA PT-08, Pacer Technologies) was used to harvest the rigid particles. The perfluoropolyether (PFPE) prepolymer resin (Fluorocur[®], Liquidia Technologies, Inc.) was mixed with 0.1% (w/v) DEAP photoinitiator before use.

The untreated side of poly(ethylene terephthalate) (PET) sheets (Melinex 453, DuPont) was used for mold support and for monomer distribution and removal.

Different particle compositions were used to control zeta potential, as well as mechanical properties. A series of rectangular rod particles (Figure 3.11) were fabricated with either a positively charged monomer composition: 79.5 wt% PEG₉₁₂TA, 20 wt% AEM, 0.5 wt% DEAP, or a negatively charged monomer composition: 79.5 wt% PEG₉₁₂TA, 20 wt% CEA, 0.5 wt% DEAP. The particles were imaged with SEM. The zeta potential measurements were also obtained using a Malvern Instruments Nano-ZS Zetasizer. The zeta potential measurements for the rod particles are shown in Table 3.2.

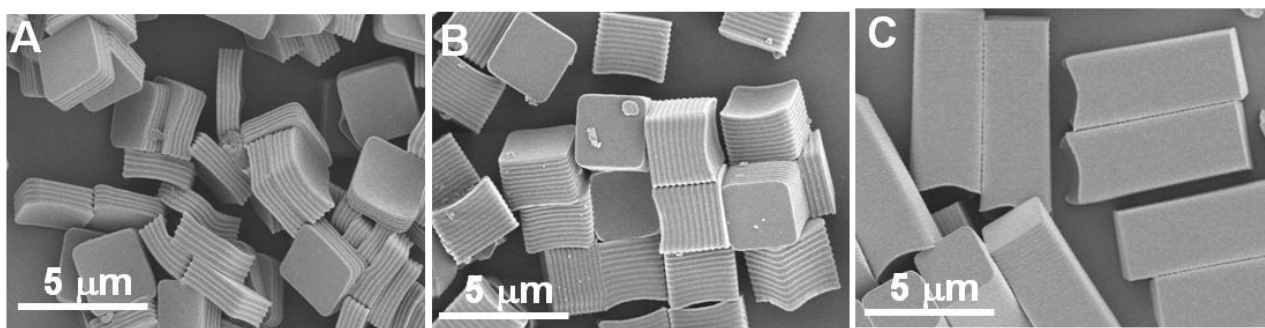


Figure 3.11. SEM images of the rigid particle series (A) $2.8 \times 2.8 \times 0.9 \mu\text{m}$ (AR = 0.3), (B) $2.8 \times 2.8 \times 2.2 \mu\text{m}$ (AR = 0.8) and (C) $2.8 \times 2.8 \times 6.5 \mu\text{m}$ (AR = 2.3).

Table 3.2. Zeta potential measurements of rod particles

Particle AR	Zeta Potential (mV)	
	AEM	CEA
0.3	$+32.9 \pm 1.8$	-56.9 ± 0.49
0.8	$+35.9 \pm 2.6$	-63.6 ± 1.7
2.3	$+44.4 \pm 1.5$	-68.0 ± 1.7

Deformable disk particles ($6 \times 1.5 \mu\text{m}$), shown in Figure 3.12, were fabricated with the following composition: 95 wt% CEA, 4.5 wt% PEG₁₀₀₀DMA and 0.5 wt% DEAP. The particles were imaged by optical microscopy and SEM. As only a small quantity of crosslinker was used in the monomer solution, the particles were deformable as can be observed in the SEM images in Figure 3.12.

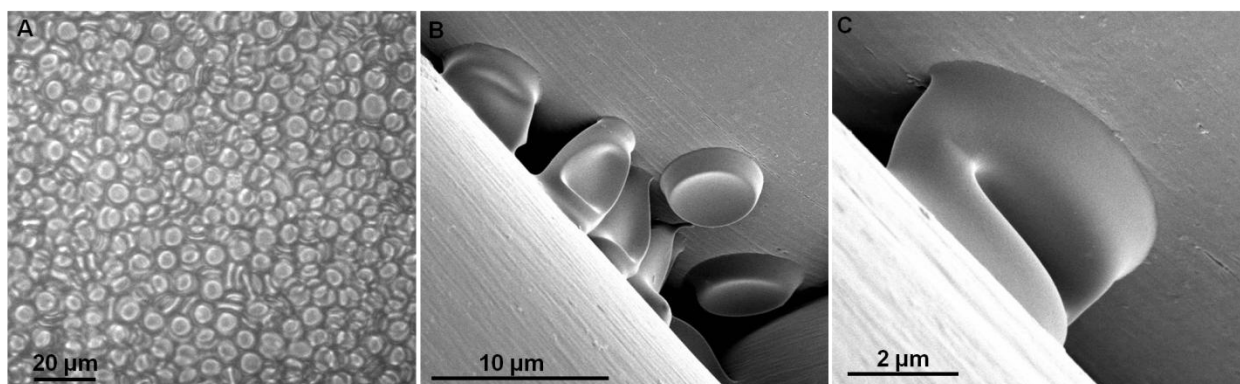


Figure 3.12. Deformable CEA particles image (A) DIC image of dried drop of particles, and (B, C) SEM images of particles dried on a woven fiber membrane.

3.3.2 Experimental Design and Set-up

Microchannel masters were first fabricated with the inverse channel pattern in photoresist. Masters were fabricated two types of microchannels: a straight clear channel (25 μm width) and straight channel with patterned blocks as shown in Figure 3.13, creating gaps with varying dimensions (3 – 8 μm). These masters were used to mold PDMS channels. Once removed from the masters, reservoirs (diameter = 0.6 cm) were punched out using a metal pipe. Both the PDMS channels and glass cover slides were treated with oxygen plasma then brought into contact to seal. Platinum wire inserted into both reservoirs served as the electrodes. A third type of microfluidic device was fabricated that simply consisted of an embossed PEG₉₁₂TA film on PET with $5 \times 5 \times 5 \mu\text{m}$ features (pitch = 10 μm) sandwiched

with a glass cover slip with deposited electrodes. The array was bonded to the glass with O₂ plasma treatment (Figure 3.14).

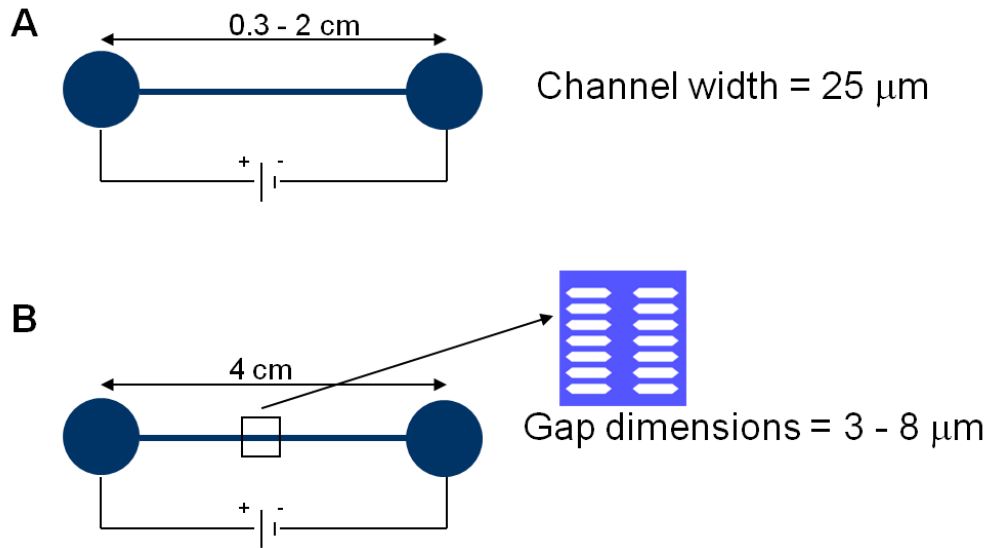


Figure 3.13. Two types of microfluidic channels where (A) is a straight channel design and (B) is a microchannel design with patterned gaps

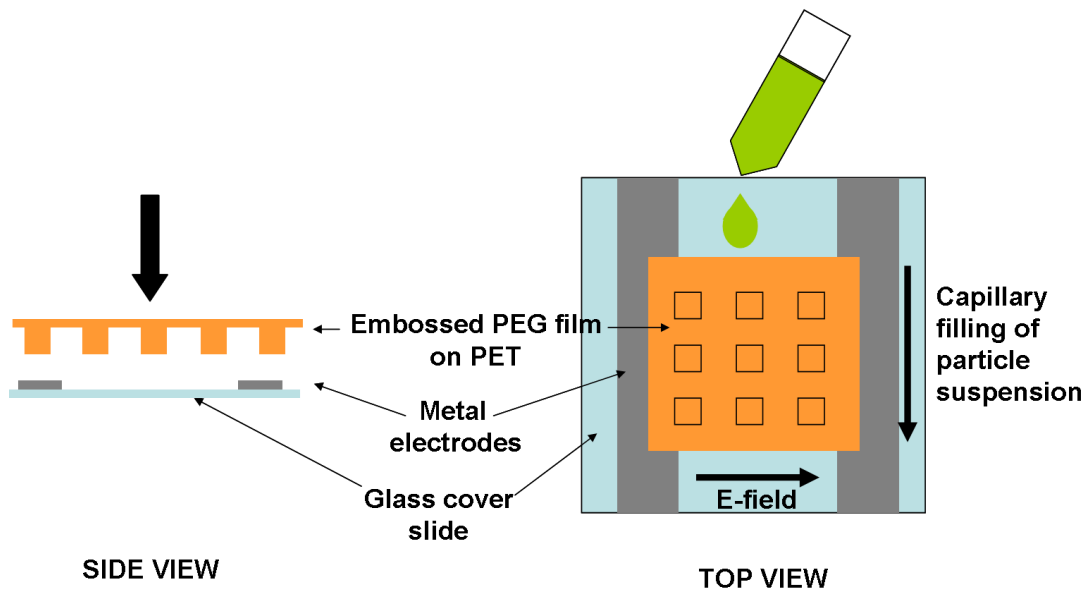


Figure 3.14. Third type of microfluidic device consisting of a cubic feature array

3.3.3 Results and Discussion

The motion of rigid particles was studied in the straight microchannel design shown in Figure 3.13A. Particle suspensions were prepared in deionized water, in 1 wt% CTAB and in 1% Pluronic. In deionized water, the particles were too aggregated to perform single particle tracking. Furthermore, the aggregates quickly clogged the channels preventing further use. Particles were well stabilized in the presence of surfactant, either CTAB or Pluronic. Upon the application of a DC electric field, particles were found to move through the microchannels. The negatively charged particles were found to move towards the negative electrode and the positively charged particles moved towards the positive electrode. This indicated that the particle motion was actually due to electroosmosis. As the positively charged particle counter-ions moved towards the negative electrode, it induced fluid flow in that direction. Particle speed was field strength dependent, and as the field strength increased, the speed also increased. The surfactant affected the particle speed, for example when positively charged $2.8 \times 2.8 \times 0.9 \mu\text{m}$ particles were suspended in CTAB, they moved approximately 5 times faster than in Pluronic (Figure 3.15). Additionally, changing the particle aspect ratio affected the speed of the particles. In Figure 3.16, the speeds of negatively charged particles with aspect ratios 0.8 and 2.3, suspended in 1 wt% Pluronic, are shown as a function of E field strength. The larger particles were observed to move faster as a function of E field strength. It is not clear why the larger particles have faster velocities. It should be noted that the particle motion was not always linear, particles were sometimes found to tumble and spin through solution.

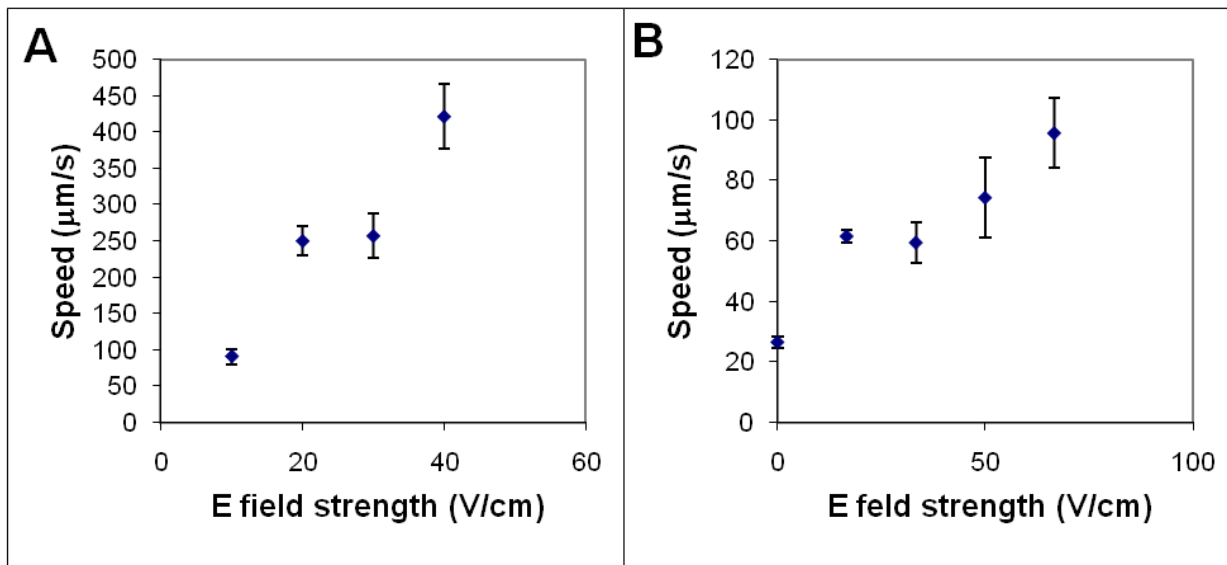


Figure 3.15. Particle speed as function of electric field strength for positively charged $2.8 \times 2.8 \times 0.9 \mu\text{m}$ particles suspended in (A) 1 wt% CTAB and (B) 1 wt% Pluronic.

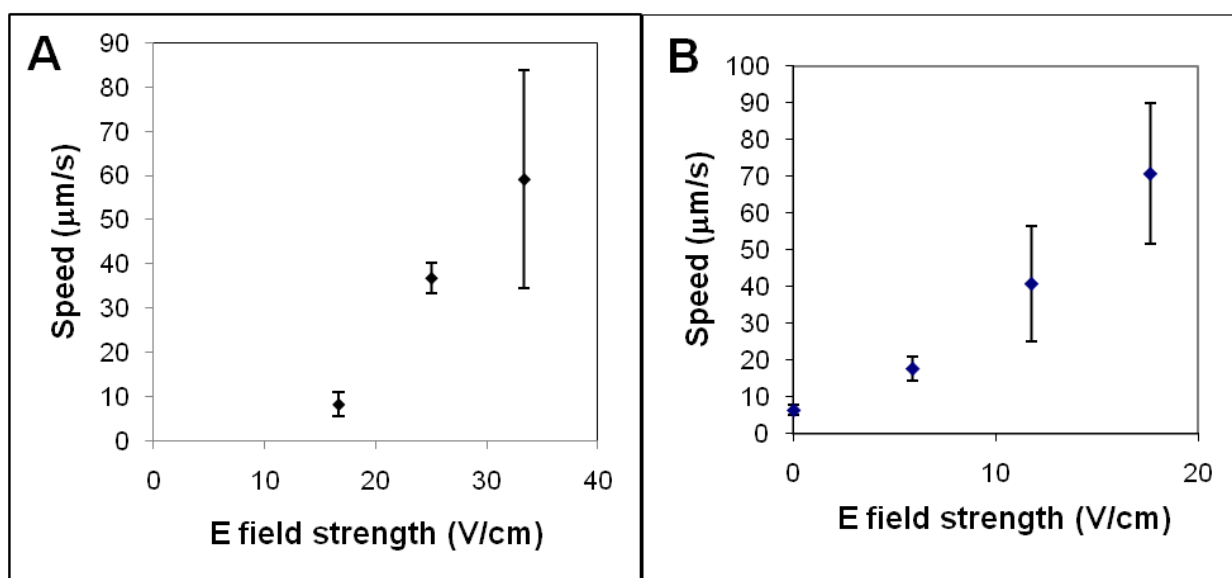


Figure 3.16. Particle speed as function of electric field strength for negatively charged particles suspended in 1 wt% Pluronic, where the particle sizes are (A) $2.8 \times 2.8 \times 2.2 \mu\text{m}$ (AR = 0.8) and (B) $2.8 \times 2.8 \times 6.5 \mu\text{m}$ (AR = 2.3).

The deformable particles were dispersed in deionized water and introduced to one of the reservoirs in the patterned microfluidic device shown in Figure 3.13B. The gap size was

6 μm . The 6 μm diameter deformable disk particles were found to pass through gaps that were of the same dimensions. Clogging would, however, occasionally occur (Figure 3.17). In addition to particle motion, it was found that the particles would assemble in the reservoirs near the electrodes (Figure 3.18).

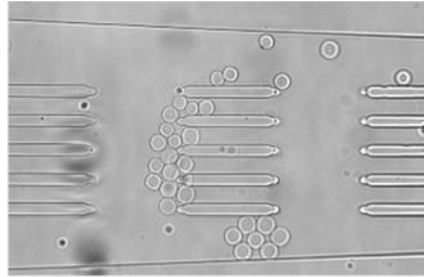


Figure 3.17. Optical image of a patterned microchannel with particles moving towards the negative electrode (E field strength = 1.25 V/cm). Clogging was present near some of the gaps.

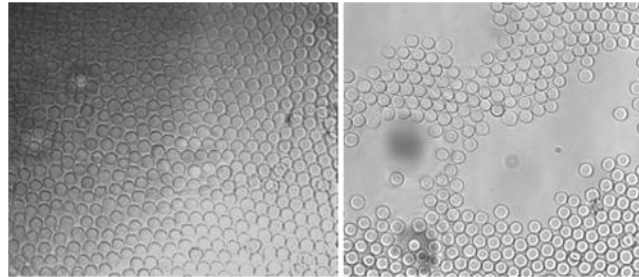


Figure 3.18. Bright field images of particle crystallization occurring near the negative electrode (Field strength = 2.5 V/cm).

For the third type of device, using an ordered array instead of a microchannel, the particle suspension was introduced near the edge of the array and it was quickly pulled into the device by capillary flow. An electric field was then applied orthogonal to the flow causing the particles to turn and move towards one of the electrodes; the change in direction was not exactly 90° as there was still a capillary force driving the fluid flow across the

device. Most of the particles turned up on their sides to move through the gaps, since the height of the device was $5\ \mu\text{m}$. Some particles however, deformed to move through the spaces. Figure 3.19 shows how the particles got stuck between the features.

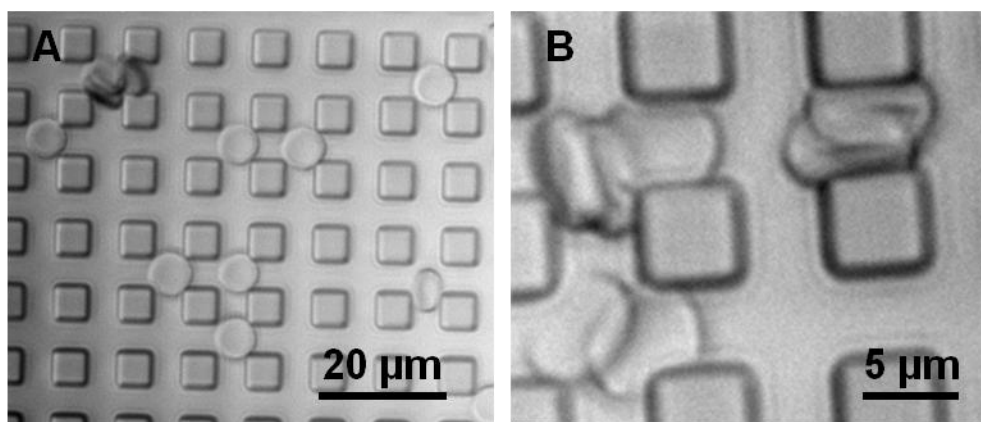


Figure 3.19. DIC images of deformable particles in $5\ \mu\text{m}$ square array

3.4 Summary and Future Outlook

The ability of the PRINT process to design and fabricate new particle shapes with tailored chemistries expands the possibilities for observing and characterizing novel particle assemblies, and for the design and synthesis of advanced composite materials with interesting nanostructures. In this work, novel organic particle geometries were introduced to the study of colloidal assemblies, demonstrating that these new shapes can influence interesting packing and crystallization behavior. With the exception of the boomerang shaped particles, all particle shapes studied exhibited chaining behavior in the presence of the nonuniform AC electric field. Moreover, the results are consistent with others, as the anisotropic particles preferentially align with their longest axes parallel to the field. Different crystal structures were observed when the chains assembled: hexagonal close packed for the

hexnuts and disks, and rectangular for the rods. Interestingly, even though the boomerangs did not align in chains in the field, regions of unique packing were observed. In addition to particle crystallization, particle motion was induced with DC fields. Using the phenomenon of electroosmosis, deformable particles were able to traverse confined geometries, smaller than the particle dimensions. This work holds promise for pursuing this concept further with more deformable particles and more complex microchannel geometries. The ability to force particles through constrictions using electric fields can be potentially useful in the field of drug delivery where driving drug delivery vectors through confined, complex spaces is important for tumor delivery.

3.5 References

1. Asencor, F. J.; Santamaria, C.; Iglesias, F. J.; Dominguez, A. *Biophys. J.* **1993**, 64, 1626-1631.
2. Morgan, H.; Green, N. G. *J. Electrostat.* **1997**, 42, 279-293.
3. Poortinga, A. T.; Bos, R.; Busscher, H. J. *Biotechnol. Bioeng.* **2000**, 67, 117-120.
4. Radu, M.; Ionescu, M.; Irimescu, N.; Iliescu, K.; Pologea-Moraru, R.; Kovacs, E. *Biophys. J.* **2005**, 89, 3548-3554.
5. Yang, M.; Chew Lim, C.; Liao, R.; Zhang, X. *J. Microelectromech. Sys.* **2006**, 15, 1483-1491.
6. Bhatt, K. H.; Velev, O. D. *Langmuir* **2004**, 20, 467-476.
7. Lumsdon, S. O.; Kaler, E. W.; Velev, O. D. *Langmuir* **2004**, 20, 2108-2116.
8. Lumsdon, S. O.; Kaler, E. W.; Williams, J. P.; Velev, O. D. *Appl. Phys. Lett.* **2003**, 82, 949-951.
9. Herlihy, K. P.; Nunes, J.; DeSimone, J. M. *Langmuir* **2008**, 24, 8421-8426.
10. Merkel, T.; Herlihy, K.; Nunes, J.; Orgel, R.; DeSimone, J. M. *Langmuir* **2009**, in press.
11. Rolland, J. P.; Maynor, B. W.; Euliss, L. E.; Exner, A. E.; Denison, G. M.; DeSimone, J. M. *J. Am. Chem. Soc.* **2005**, 127, 10096-10100.
12. Yang, C. Y.; Lei, U. *J. Appl. Phys.* **2007**, 102, 094702.
13. Velev, O. D.; Bhatt, K. H. *Soft Matter* **2006**, 2, 738-750.

Chapter 4

Magnetic Manipulation of PRINT Particles

4.1 Specific Research Objectives

The great interest in uniform multifunctional materials inspired this work on the fabrication and manipulation of composite magnetic particles. Here the fabrication of highly tailored nanoscale and microscale magnetic particles was demonstrated using the Particle Replication in Non-wetting Templates (PRINT) process. Magneto-polymer composite nanoparticles were fabricated in three distinct particle shape morphologies: filamentous (worm-like), rice-like (approximating an ellipsoidal shape) and cylindrical. These nanoparticle shapes, in particular the highly anisotropic filamentous worm-like nanoparticles, have great promise in the life science field as for example, drug delivery vectors.¹⁻³ Furthermore, this work represents the first examples of magneto-polymer composite nanoparticles fabricated using top-down technology. Magneto-polymer composite microparticles were also fabricated in different particle shape morphologies: boomerang-shaped and a series of rhombohedral (rectangular rod shaped) particles with varying aspect ratios.

One advantage of using the PRINT process to fabricate these microparticles is the ability to manipulate the magnetic cargo within the particle matrix prior to polymerization of the resin that constitutes the bulk of the particle matrix. Magnetic nanoparticle chains can be permanently aligned in desired directions relative to the composite particle axes; this configuration dictates the particle motion in response to external magnetic fields. Top down fabrication routes have previously fabricated magneto-polymer shape specific particles, where the shape defines the magnetic field derived motion,⁴ however, this is the first example, where the shape anisotropy contribution is dominated by the controlled nanostructuring of the magnetic nanoparticles within the particle. As a further demonstration

of the considerable capacity of the PRINT process to fabricate particles with precisely defined properties, the magneto-polymer composite microparticles were further functionalized anisotropically to yield microparticles with internally structured magnetic nanoparticles within the body of the particle and platinum metal functionalization on one end of the particle. These complex particles can serve as steerable micromotors when dispersed in hydrogen peroxide solution. Thus multifunctionality was achieved as the particles exhibit both catalytic propulsion capabilities, as well as the ability to be guided magnetically.

4.2 Experimental

4.2.1 Particle Fabrication and Characterization

Composite particles were fabricated with some minor modifications using the standard PRINT technique described in detail in Chapter 2 and elsewhere.⁵⁻⁹ All particle precursor solutions were poly(ethylene glycol)-based solutions that were reacted to form a crosslinked gel via UV free-radical polymerization. Different compositions were used for micron-sized and nano-sized particles. The microparticles were composed of 68 wt% poly(ethylene glycol) triacrylate (PEG-TA, Sartomer, $M_n = 1176$ g/mol), 10 wt% aminoethyl methacrylate hydrochloride (AEM, Sigma-Aldrich), 10 wt% 200 nm uncoated magnetite (Fe_3O_4 , Polysciences, Inc.), 10 wt% of a 1 wt% Pluronic solution (Pluronic F68, Sigma), 1 wt% fluorescein *o*-acrylate (Sigma-Aldrich) and 1 wt% 2,2'-diethoxyacetophenone, (DEAP, Sigma-Aldrich). The nanoparticles were composed of 78 wt% PEG-diacrylate ($M_n = 700$ g/mol, Sigma-Aldrich), 10 wt% N-aminopropyl methacrylamide (APMA, Polysciences, Inc.), 10 wt% dextran-stabilized (~20 nm) Fe_3O_4 nanocrystals (FluidMag DX, Chemicell

GmbH), 1 wt% fluorescein *o*-acrylate (Sigma-Aldrich) and 1 wt% 1-hydroxycyclohexylphenyl ketone (HCPK, Sigma-Aldrich).

The magnetite used for the PRINT micro- and nanoparticles were different because of the size constraints imposed by the mold features. For PRINT nanoparticles, the size of the magnetite nanocrystals had to be at least half the smallest dimension of the mold features. The magnetite sample used was dextran-coated, fairly uniform in shape, and approximately 20 nm in size (FluidMag DX, Chemicell GmbH). For the PRINT microparticles, larger magnetite nanoparticles were used to ensure a strong magnetic response. This magnetite sample (black iron oxide, Polysciences) was a polydisperse, mechanically milled sample with random non-uniform particle shapes. Figure 4.1 compares the two magnetite samples.

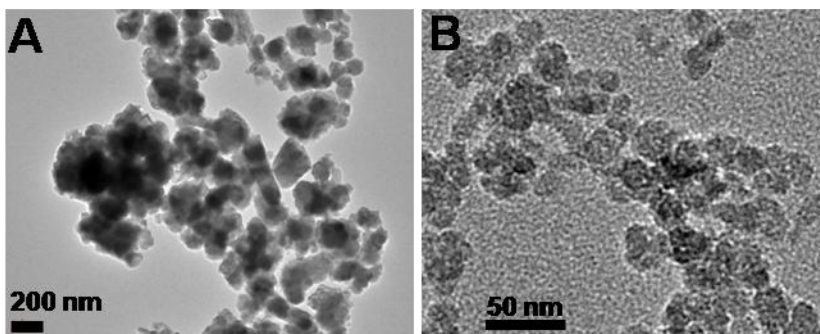


Figure 4.1. TEM images of the magnetite samples used in the PRINT composite (A) microparticles and (B) nanoparticles.

A range of molds were used to fabricate the micro- and nanoparticles. Three nanoparticle shapes were used, with the following approximate dimensions: 200×200 nm cylinders, 80×320 nm rice and 80×2000 nm worms. All nanoparticle molds were supplied by Liquidia Technologies. The microparticle shapes were boomerangs (arm length = $10 \mu\text{m}$, arm width = $4 \mu\text{m}$, thickness = $1 \mu\text{m}$) and a block series with a $2 \times 2 \mu\text{m}$ cross-section (B1

length = 1 μm , B2 length = 4 μm and B3 = 5 μm). Microparticle molds were fabricated in-house using a commercial PFPE precursor (Fluorocur[®], Liquidia Technologies); refer to Chapter 2 for mold fabrication details. Mold features have sharp angles on the micron scale but more rounded on the nanoscale as the limits of resolution are approached for silicon master fabrication.

For the nanoparticles, the preparticle suspension without Fe_3O_4 , was diluted with dimethylformamide (DMF, Fisher Scientific) after which an aliquot of dextran-stabilized Fe_3O_4 nanoparticles was added. No additional stabilization of these particles was necessary. A thin film (~ 2.5 μm) was cast over a sheet of poly(ethylene terephthalate) (PET, 5 mil Melinex 453, KRS Plastics) using a Mayer rod (2.5 μm feature size RD Specialties, Inc.). After a brief drying period to evaporate the DMF solvent, the thin film was laminated to, and immediately split from a patterned PFPE mold, thus filling the cavities of the mold with the pre-particle suspension. Next, a second sheet of PET was laminated to the surface of the filled mold that was then placed in a UV curing chamber. After curing (~ 12 J/cm^2 , 365 nm), the particles adhered to the PET sheet as the PET was split from the mold, allowing for easy particle removal from the mold. The particles were removed from the PET sheet by spreading 400 μL of distilled water over the surface and gently agitating the particles. The particles were then rinsed with Milli-Q water to remove any sol fraction and non-magnetic debris using a magnetic column (MiniMacs, Miltenyi Biotec).

For the microparticles, the particle precursor suspension was applied to the mold neat, and the particles were cured open face in the mold. For all experiments, the composite particles were charged with 10 wt% Fe_3O_4 , though it was possible with this process to vary the Fe_3O_4 content up to 50 wt%. If alignment of the Fe_3O_4 was desired, prior to curing, the

filled PFPE mold was placed between two neodymium magnets (14.8 kGauss each) separated by one inch for at least 2 minutes. During this time, the Fe_3O_4 nanocrystals formed linear aggregates parallel to the applied field. After curing, the particles were harvested using polycyanoacrylate (Zap CA PT-08, Pacer Technologies), and then centrifuged and washed first with acetone 5 times to remove residual adhesive then transferred to Milli-Q water for improved stability and handling.

The rhombohedral particles (B1, B2 and B3) were end-functionalized with both dye and metal. For dye functionalization, a 1 mg/mL aqueous solution of a reactive dye, Texas Red sulfonyl chloride (Invitrogen), was placed in a shallow crystallization dish. The full PFPE mold containing particles was immersed (particles side down) in the solution for approximately 1 minute. Texas Red sulfonyl chloride reacted rapidly with the primary amine groups on the exposed particle surface (from the AEM monomer) attaching the dye to the particle through stable sulfonamide bonds. The mold was then removed and rinsed with deionized water. The end-functionalized particles could then be harvested. To functionalize with metal, 3 nm titanium (Ti) followed by 20 nm platinum (Pt) were evaporated onto the full mold of particles using a CHA Industries Solution E-Beam Metal evaporator. The particles were then harvested from the mold using polycyanoacrylate. Following the harvesting step, the particles were washed multiple times in acetone and collected in distilled water. It was also possible to put the dye and the metal on opposite faces of the particles. To do so, the particles were polycyanoacrylate-harvested after reacting the dye to the exposed face of the particles and then the Ti and Pt were evaporated on the particles in the harvested array, where the opposite side of the particles were exposed. The particles were then washed

and collected as described above. Both approaches were equally effective at anisotropically surface functionalizing the particles.

4.2.2 Magnetite Chaining Experiments

To determine the effects of concentration, time and field strength on the magnetite chains that form prior to curing, studies were performed using the boomerang-shaped particles. The molds were filled with pre-polymer resin containing 1, 5, and 10 wt% iron oxide nanoparticles. The filled molds were subjected to low magnetic field (between two 6.9 kGauss magnets spaced one inch apart) or high magnetic field (between two 14.8 kGauss magnets spaced one inch apart) for up to 3 minutes (30, 60 and 180 s) after which the resin was cured by photopolymerization. Fifty particles in the mold were examined for each time point, field intensity, and nanoparticle loading. The molds were visualized using fluorescence microscopy (Zeiss Axioskop 2 MAT incident light microscope fitted with an AxioCam MR digital camera).

4.2.3 SQUID Experiments

Three samples (30 – 40 mg each) of the B3 ($2 \times 2 \times 5 \mu\text{m}$) particles containing 10 wt% Fe_3O_4 were prepared: one sample cured without a magnetic field, a second sample with the magnetic field perpendicular to the length of the particle, and a third sample with the magnetic field parallel to the length of the particle. After purification, the particles were dried and loaded into gelatin capsules. The measurements were performed at 298 K using a Quantum Design MPMS superconducting quantum interference device (SQUID) magnetometer. The samples were subjected to DC magnetic fields to ± 5 T.

4.2.4 Magnetic Stage Setup for Imaging Particle Rotation and Chaining in Water

An in-house rotating magnetic stage was constructed using a circular runner with a 4 inch void in the center for sample placement. Two neodymium (6.9 kGauss) magnets were placed on the runner with their magnetic poles facing in one direction. The runner was then equipped with a remotely controlled electronic motor that turned the magnets around the open center of the runner (Figure 4.2). This magnetic apparatus was placed on a microscope stage with a cell of magnetic particles directly in the center of the stage.

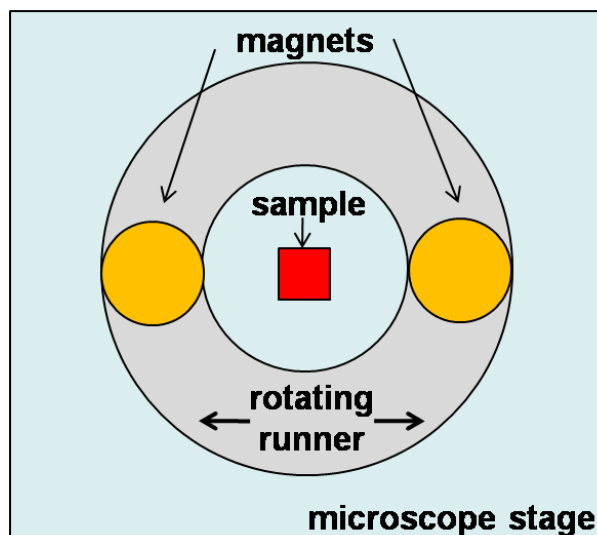


Figure 4.2. Schematic of an in-house magnetic stage for particle rotation and alignment experiments in water. The runner (gray) rotates in a circular fashion around the magnetic particle sample (red) in the center of the microscope stage (light blue). Magnets at opposite ends of the runner (orange) create a magnetic field across the particle sample that rotates with the runner.

4.2.5 Particle Polymerization Experiment

A particle “polymerization” experiment was conducted to analyze the growth of the composite particle chains in a constant magnetic field at a constant composite particle concentration over time. Optical images of the chaining events were taken, starting from the

introduction of the particle suspension to the magnetic field ($t = 0$ seconds), in 30 second intervals for 5 minutes. The lengths of 20 chains per image were measured, and the rate of chain growth, average chain length and chain length distribution (polydispersity index) were calculated.

4.2.6 Magnetic Stage Setup for Particle Tracking Experiments in H_2O_2

A Nikon Diaphot inverted microscope, operated in transmission mode, was used for this experiment. Particles were dosed into prefabricated sample wells (Grace Bio Labs) and imaged in solution. Magnetic forces were applied to these particles via a 25mm x 11mm x 5mm NdFeB (Grade N42, K&J Magnetics) located above the sample, positioned approximately 1 cm away from the sample center. Placing the magnet away from the center of the light path ensured that the magnet did not interfere with the transmitted light. The field at the surface of this magnet was 595 G. This magnet was attached to a Barber-Colman inline gearmotor which enabled us to rotate the magnet around a central axis for PRINT particle manipulation. The motor was controlled by a Pasco Scientific SF-9584A low voltage AC/DC power supply; typically, the motor was operated between 10 and 100 RPM (Figure 4.3).

The video data was collected at 30 frames per second using a 10X objective and a Pulnix PTM-6710CL camera. In-lab custom designed video tracking software (R.M. Taylor, Video Spot Tracker 8, 2009, http://cismm.cs.unc.edu/downloads/?dl_cat=3) was used for particle tracking and motion analysis.

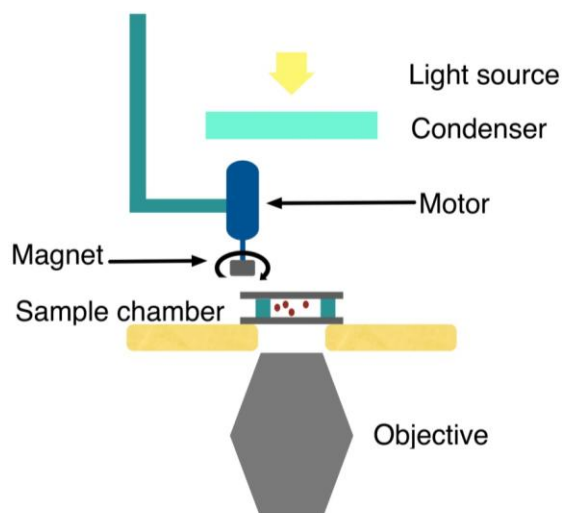


Figure 4.3. Schematic of the microscope and magnet setup for micromotor experiments. The magnet was mounted on a motor and was suspended above the sample, slightly off-center from the path of the transmitted light.

4.3 Results and Discussion

4.3.1 Magneto-Polymer PRINT Composite Particles

Magnetite-loaded PRINT nanoparticles were successfully fabricated in three shapes: worms, rice and cylinders, as shown in Figure 4.4. Both on the harvesting layer (Figure 4.4A-C) and after washing (Figure 4.4D-F), the particles appeared intact, with magnetite fairly uniformly distributed throughout the particles. While the composite nanoparticles were magnetic, their magnetic response in the sample cell using a pair of magnets (14.8 kGauss each) was slow. It was also difficult to visualize using fluorescence microscopy.

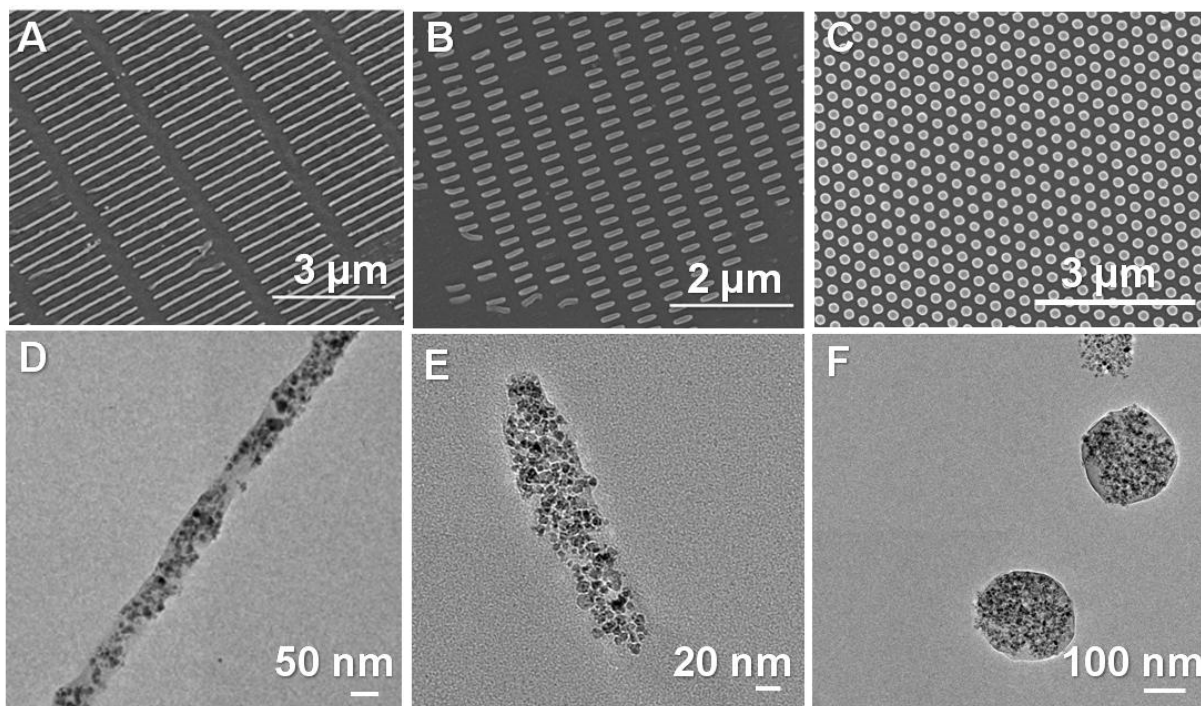


Figure 4.4. SEM (A-C) and TEM (D-F) images of PRINT magneto-polymer nanoparticles on the harvesting layer and collected from solution, respectively. (A,D) are 80×2000 nm worm particles, (B,E) are 80×320 nm rice particles, and (C,F) are 200×200 nm cylindrical particles.

Magnetite-loaded PRINT microparticles were also successfully fabricated. The magnetite loading capacity was determined by fabricating boomerang particles with three different magnetite concentrations: 1 wt%, 10 wt% and 50 wt%. Figure 4.5 shows these boomerang particles in the mold. Small magnetite aggregates were visible in the 1 wt% loaded particles (Figure 4.5A); these particles responded poorly to external magnetic fields. Larger aggregates were observed in the 10 wt% loaded particles (Figure 4.5B). Particles loaded with 50 wt% magnetite appeared almost completely black from the large concentration of magnetite present (Figure 4.5C); these particles were often difficult to fabricate due to the formation of an interconnected flash layer during mold filling. The 50 wt% loaded particles also had poor structural integrity. As such, all experiments were

conducted with particles containing 10 wt % magnetite, which responded rapidly to moderate magnetic fields and had very little embossed film formation during fabrication.

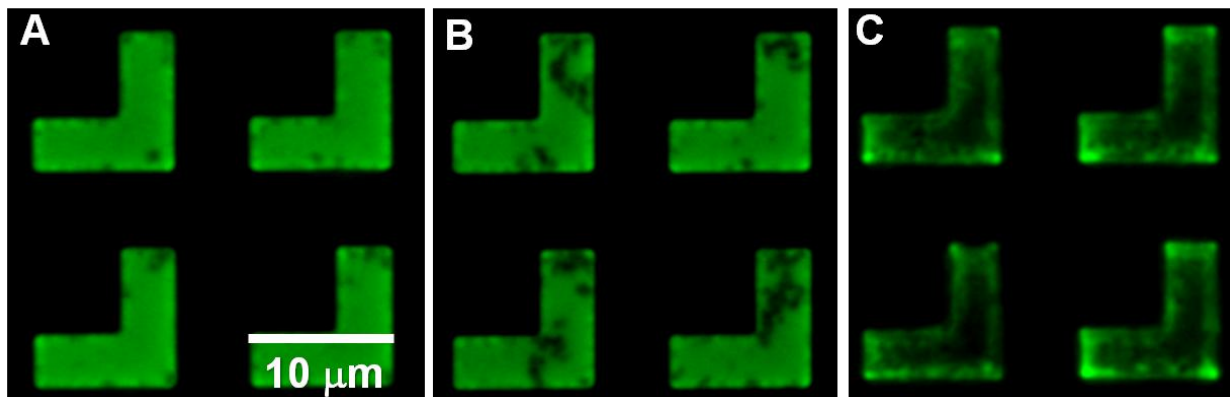


Figure 4.5. Fluorescent micrograph of particles in the mold containing (A) 1, (B) 10, and (C) 50 wt% magnetite particles. Aggregates of magnetite are visible in the particles as dark spots in the green fluorescent polymer background.

Overall particle shape has been shown to dictate the direction of the particle's magnetic moment.⁴ The particle shape directionality however can be overruled by controlling the organization of the nanoparticles within the microparticles. Using the PRINT process, the magnetic moment can be dictated by the net magnetic moment of the magnetite aggregates within the composite particle. Alignment of magnetite within the polymer-composite was possible due to the unique top-down approach to particle fabrication (Figure 4.6). Directionality of the Fe_3O_4 chains, with respect to the polymer composite particle, was controlled by changing the orientation of the mold in the magnetic field. After alignment, the chains were immobilized in the desired orientation by UV curing the monomer matrix. As such, a wide variety of magnetic configurations were possible, thus demonstrating the fact

that the orientation of the magnetic moment of the composite particles was independent of the overall particle shape.

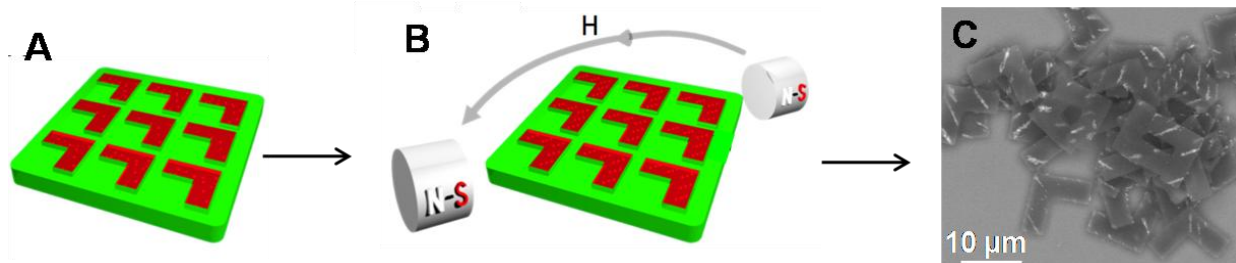


Figure 4.6. A schematic representation of the PRINT process where (A) is the PFPE mold (shown in green) and particle precursor solution (shown in red) containing randomly dispersed Fe_3O_4 , (B) shows the full mold placed in a magnetic field created by two permanent magnets and linear aggregates of Fe_3O_4 are formed prior to photopolymerization of the composite particle, and (C) ESEM image of harvested boomerang particles with linear aggregates of magnetite visible via the backscattered electron detector.

To demonstrate the directionality of the magnetite linear aggregates, boomerang particles were cured with no applied field (Figure 4.7A), parallel to one arm of the particle (Figure 4.7B), normal to the plane of the particles (Figure 4.7C), and at 45° to both arms of the boomerang (Figure 4.7D). In Figure 4.7, the dark regions void of fluorescence within the green polymer matrix clearly indicate the presence of Fe_3O_4 nanoparticles. It was found that when there was no applied magnetic field during curing, the composite particles were not homogeneous as the Fe_3O_4 nanoparticles formed small random aggregates within the particles (Figure 4.7A). This may be because, even though the non-ionic surfactant, Pluronic, was used in the monomer suspension, the nanoparticles were still not well-stabilized in the monomer suspension. The use of particles stabilized with a suitable organic coating would most likely improve the homogeneity of the composite particles, as was the cause for the PRINT composite nanoparticles. When the particles were cured in the presence of an applied field, linear aggregates of magnetite were trapped in specific directions within

the microparticles (Figure 4.7B-D). Occasionally linear aggregates of magnetite were partially adsorbed to the walls of the mold causing them to be slightly out of alignment with the magnetic field. Alignment of magnetite within the rice and worm-like particles proved difficult to obtain. We hypothesize that this is because highly defined linear aggregates were larger than the features of the rice and worm-like polymer composites themselves.

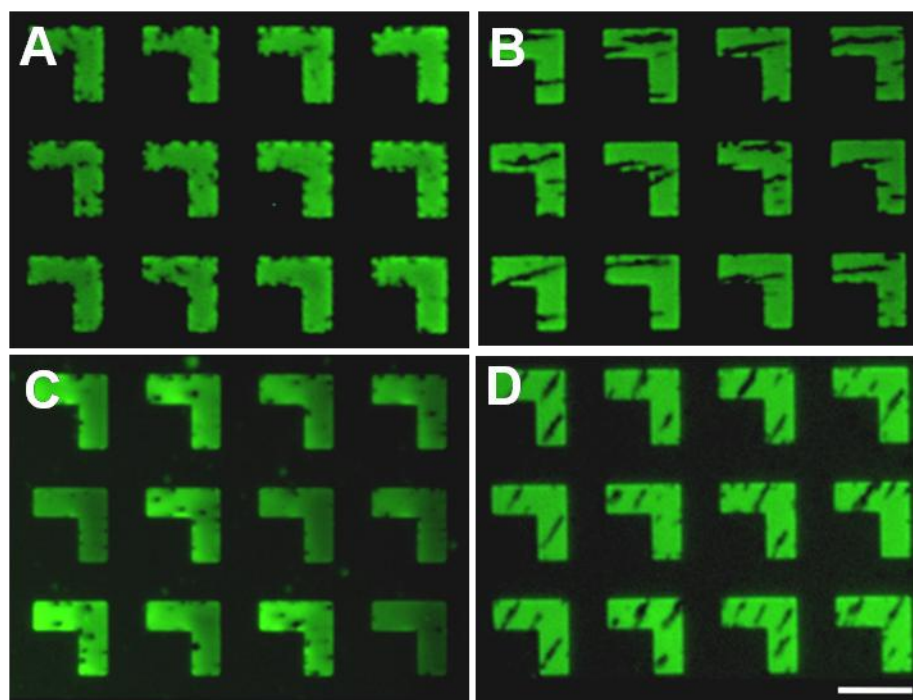


Figure 4.7. Fluorescence microscopy images of four samples of 10 μm boomerang-shaped particles in the PFPE mold with (A) no linear Fe_3O_4 aggregates, (B) aggregates in the plane and parallel to one arm of the boomerang, (C) aggregates normal to the plane of the particle, and (D) aggregates in the plane at a 45° angle to the arms of the boomerang. Scale bar is 10 μm .

The formation of linear aggregates in the boomerang microparticles was studied to determine the effect of iron oxide concentration, magnetic field strength, and time required to form linear aggregates. The results supported the use of relatively high magnetic fields and 10 wt% magnetite loading to form composite particles with multiple, long linear aggregates.

The number of magnetic linear aggregates plateaued for each iron oxide concentration after about 60 seconds (Figure 4.8). Moreover, the average length of the linear aggregates continued to grow until about 3 minutes after placing the filled molds in the field (Figure 4.9). Chains of magnetic particles cured in the strong field were typically longer than those cured in the weak field.

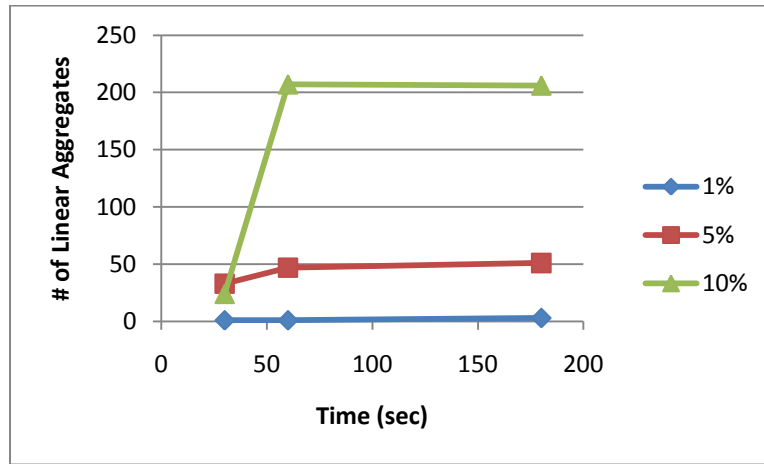


Figure 4.8. The number of magnetite chains observed in composite particles cured in a strong magnetic field as a function of the time held in the field prior to curing as well as the concentration of the magnetite nanoparticles within the composite resin.

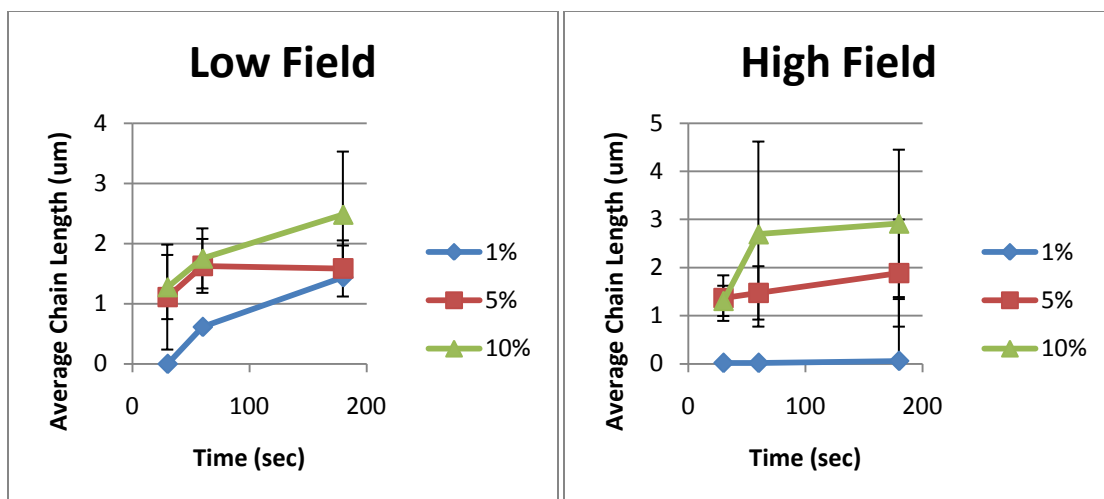


Figure 4.9. Magnetite nanoparticle chain length as a function of time, nanoparticle concentration and field strength

Rhombohedral particles were cured with no field, the field perpendicular to and parallel to the length of the particle (Figure 4.10). The magnetic properties of these particles were studied with superconducting quantum interference device (SQUID) magnetometer. Magnetization curves are presented in Figure 4.11, and the saturation magnetization results are shown in Table 4.1.

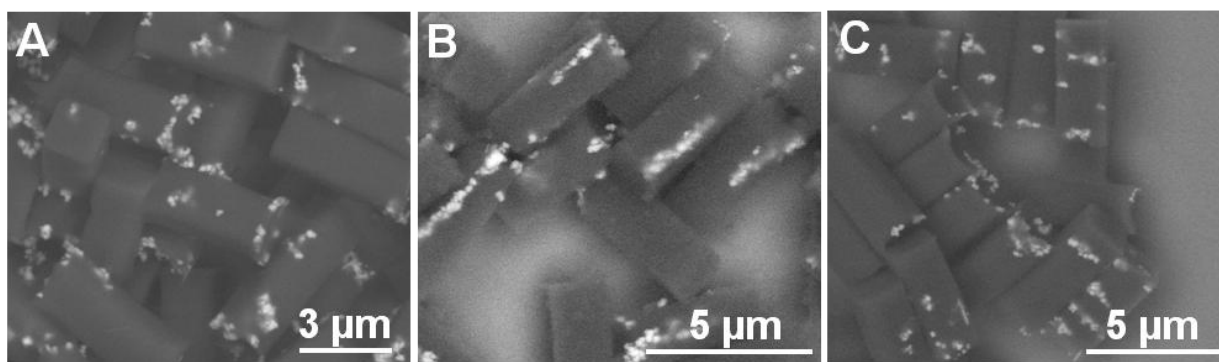


Figure 4.10. ESEM images of B3 particles ($2 \times 2 \times 5 \mu\text{m}$) with magnetite (A) randomly oriented, B3-R, (B) aligned along the long axis, B3-L, and (C) aligned along the short axis, B3-S.

Table 4.1. Saturation magnetization of B3 particles

Sample	Saturation Magnetization, M_s (emu/g)
No alignment	5.91
Perpendicular alignment	6.32
Parallel alignment	8.23

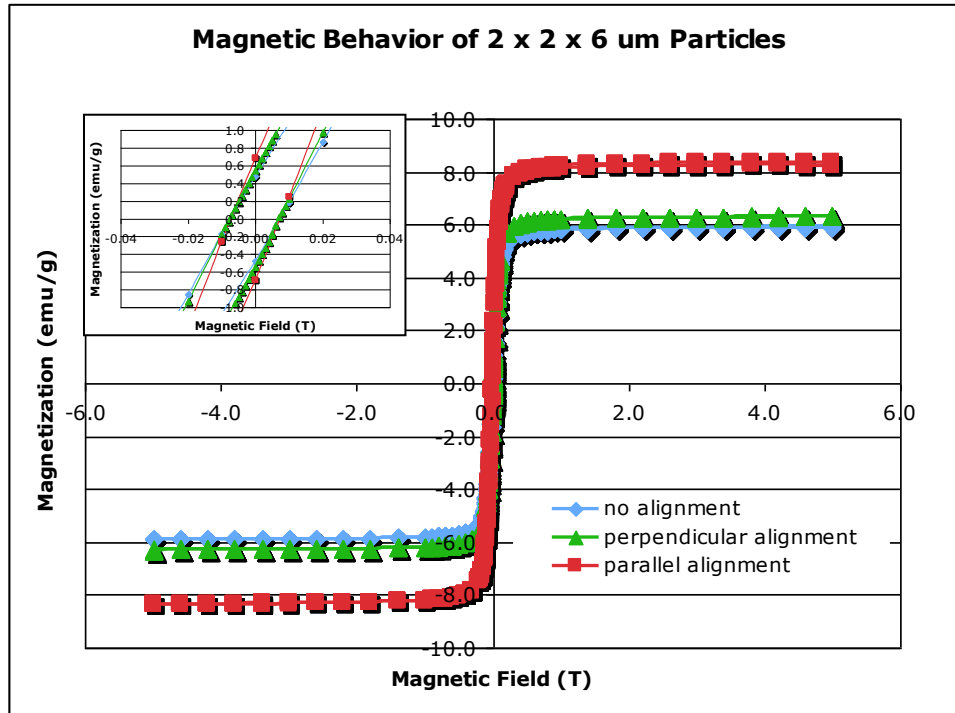


Figure 4.11. Magnetization curves for B3 particles with dispersed magnetite and linear aggregates of magnetite aligned perpendicular and parallel to the length of the particles. All magnetic orientations exhibit very low remnant magnetization, as shown in the inset curves near 0T.

An additional level of complexity was applied to the microparticle design through anisotropic surface functionalization. Both dye and metal end-functionalization were performed on the rhombohedral series of PRINT particles with square cross-sections. Three aspect ratios were used: 0.4, 2.1 and 2.5 (B1, B2 and B3, respectively), and all of the

particles contained 10 wt % Fe_3O_4 aligned parallel to the height of the particles (perpendicular to the plane of the mold). Figure 4.12 demonstrates the successful end-functionalization of a B2 particle ($2 \times 2 \times 4 \mu\text{m}$). The Energy Dispersive Spectroscopy (EDS) elemental line scan clearly indicates the relative locations of the platinum and iron present in the particle.

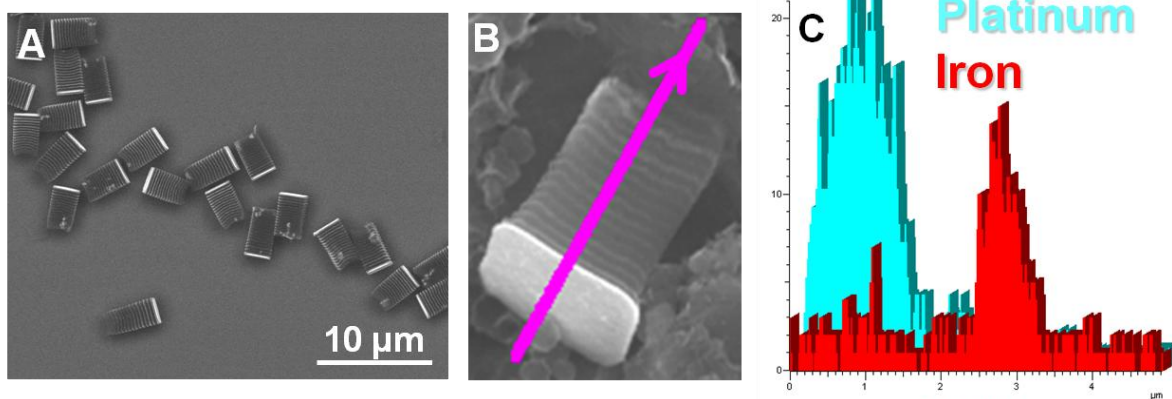


Figure 4.12. Anisotropic surface functionalization of PRINT particles, where (A) is an ESEM image of Pt-capped B2 particles containing linear aggregates of magnetite, (B) is an SEM image of a single-capped B2 particle on a graphite surface indicating the location of an energy dispersive X-ray elemental line scan (magenta), and (C) the line scan results displaying the location of the iron (red) and platinum (teal) in the particle. The Y axis of the elemental line scan is signal intensity (kcps).

4.3.2 Magnetic Manipulation of Microscale Composite Particles

Dilute aqueous suspensions of rhombohedral and boomerang-shaped composite particles were prepared, and in the absence of a magnetic field, the composite particles had no preferred orientation. Once placed in a magnetic field between two identical similarly oriented permanent magnets, the composite particles aligned with the field according to the direction of their highest magnetic moment. Composite particles with linear magnetite aggregates all aligned with the field in one orientation and followed changes in the magnetic

field as it was rotated around the microscope stage. Composite particles with randomly dispersed magnetite also changed orientation with the applied magnetic field but were not in registration with one another. Boomerang-shaped particles with linear magnetite aggregates parallel to the plane of the particle were found to rotate while laying flat (Figure 4.13). In comparison, particles with linear Fe_3O_4 aggregates normal to the plane of the particle were found to stand upright while rotating with the external magnetic field (Figure 4.14).

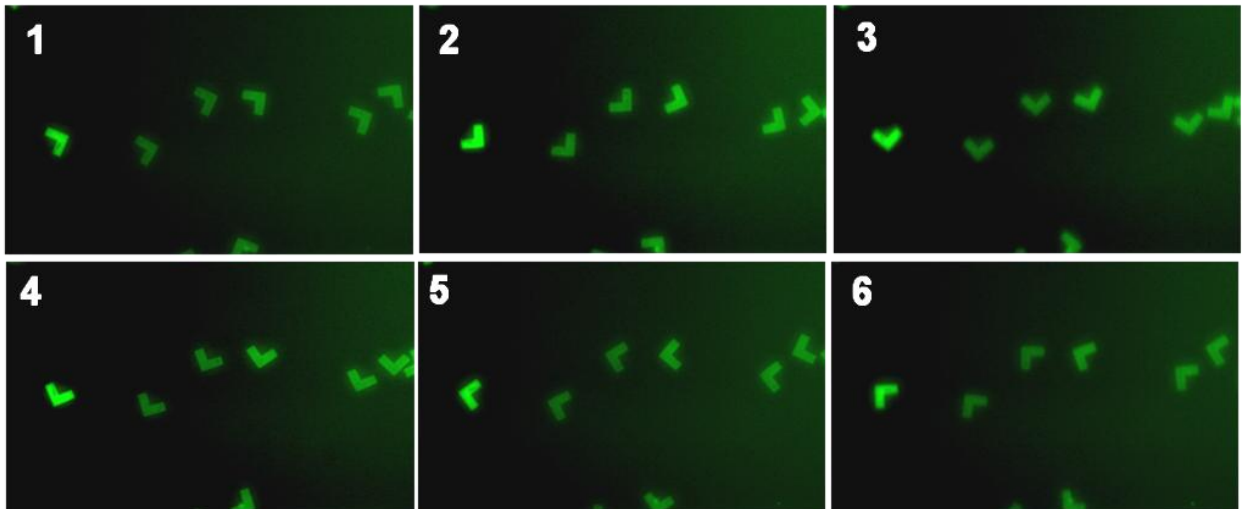


Figure 4.13. Clockwise rotation of boomerang-shaped particles, with magnetite aligned along one arm, in rotating magnetic field.

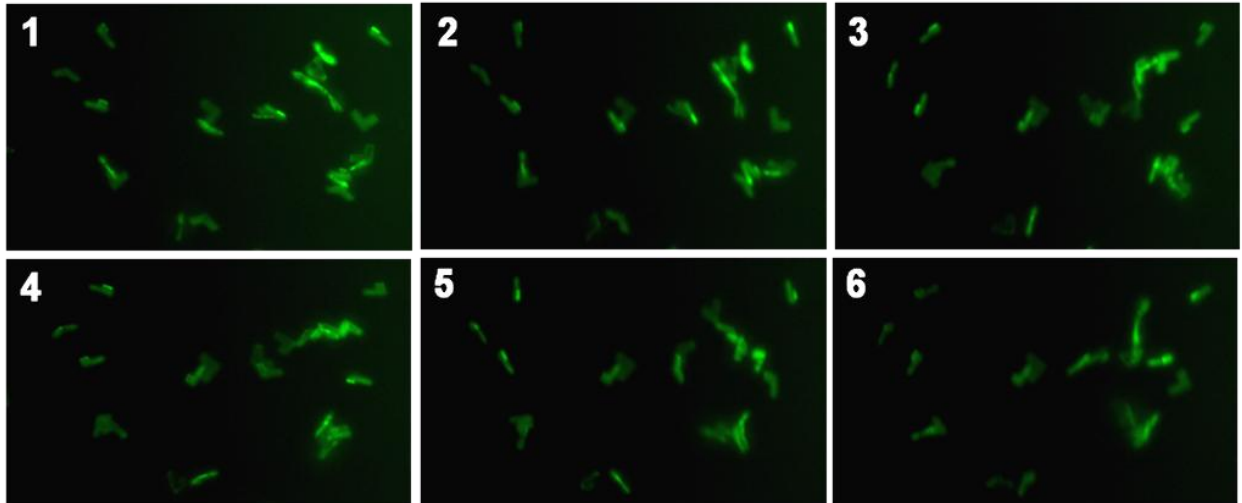


Figure 4.14. Clockwise rotation of boomerang-shaped particles, with magnetite aligned perpendicular to the plane of the particle, in rotating magnetic field.

When the concentration of composite microparticles was increased, chaining occurred. To study this, rhombohedral (B3) particles were fabricated with magnetite randomly dispersed (B3-R), aligned along the long axis (B3-L) and aligned along the short axis (B3-S); refer to Figure 4.10. Based on the directionality of the linear magnetite aggregates, chaining of B3 particles was observed in three distinct manifestations demonstrated in Figure 4.15. Samples with aggregates aligned with the long axis of the particle (B3-L) formed chains with all of the particles in line with the applied magnetic field. Samples with the linear magnetite aggregates aligned along the short axis of the particle (B3-S) formed chains of stacked composite particles. Finally, samples in which the magnetite was not aligned (B3-R) showed chaining with no specific orientation of the composite particles. It was found that the chain lengths grew to exceed the field of view after approximately 3 minutes. After two minutes B3-L composites formed the longest chains, B3-R formed shorter less ordered chains and B3-S formed the shortest chains. The chain length and number of particles/chain were plotted as a function of polymerization time for the

different magnetite aggregate orientations (Figure 4.16). For the three types of alignment, the increase in chain length was different and reflected the differences in the lengths of the linear magnetite aggregates (Figure 4.16A). This can be clearly observed when the rate of chain growth is reported in $\mu\text{m/s}$ (Table 4.2). The increase in the number of particles/chain, however, was approximately the same for all three orientations (Figure 4.16B). B3-S did not collapse onto the same graph as B3-L and B3-R did; this may be due to an experimental artifact. The similarities in the number of particles/chain is observed when the rate of chain growth is reported in particles/s (Table 4.2). In addition, for each type of magnetite alignment, the number of particles per chain (degree of polymerization) was approximately the same after two minutes. As is the case for typical step-growth polymerizations, there was a broad distribution of chain lengths for each type of alignment, as indicated by the relatively high polydispersity indices. Results are shown in Table 4.2. Once the field was removed, the chains of composite particles fell apart without the need for external agitation or de-Gaussing. SQUID confirmed that the particles had very low remnant magnetization (Figure 4.11) which probably allowed thermal energy to overcome magnetic forces that would otherwise irreversibly draw the particles together.

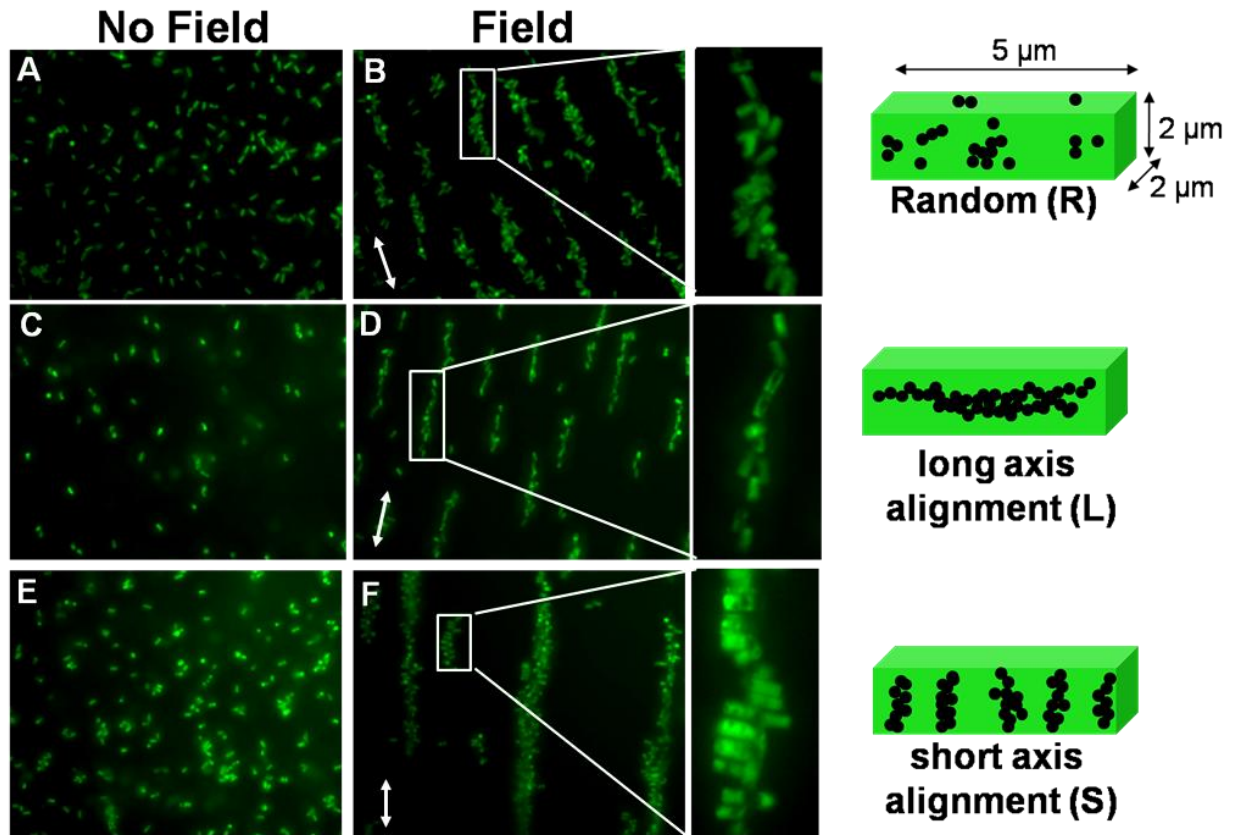


Figure 4.15. Fluorescence microscopy images of a dispersion of block-shaped B3 composite particles with different magnetite arrangements in the absence (A,C,E) and presence (B,D,F) of a magnetic field. (B) Particles without linear aggregates in an applied magnetic field formed disordered chains while (D) particles with linear aggregates parallel to the length of the composite particle formed somewhat organized chains stacking head-to-tail and (F) particles with linear aggregates perpendicular to the length of the composite particle formed somewhat organized chains stacking side-to-side respectively. Arrows indicate direction of applied magnetic field.

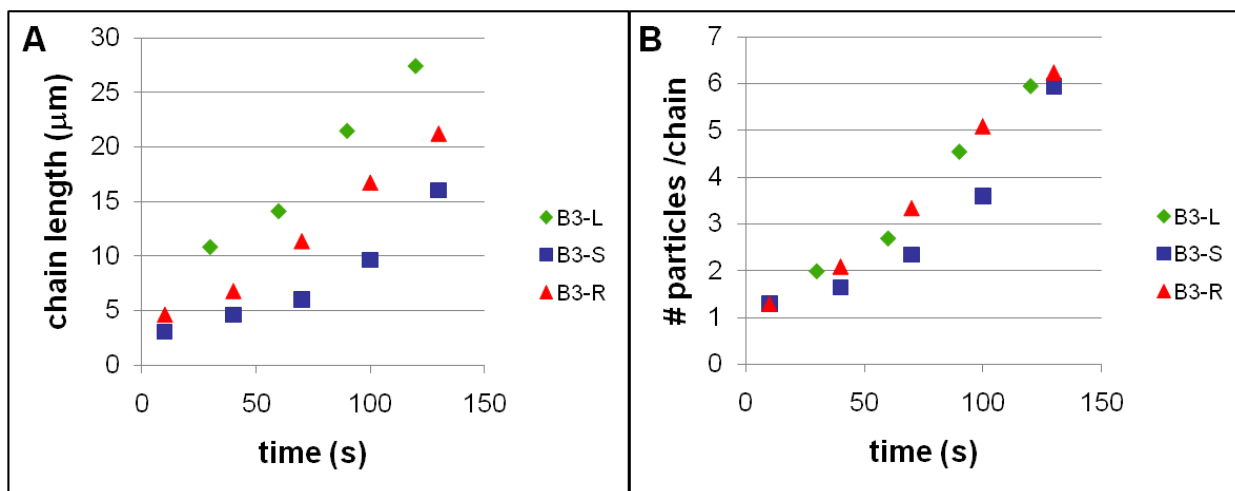


Figure 4.16. Particle polymerization experiment using B3 composite particles: (A) particle chain length as a function time and magnetite chain orientation, and (B) the number of particles per chain as a function of time and magnetite chain orientation.

Table 4.2. Composite particle polymerization experimental results.

Particle	Rate of Chain Growth ("Polymerization" Rate)		Ave. Chain Length/ μm (after 2 min.)	Ave. # of Particles/Chain "Degree of Polymerization" (at 2 min.)	Polydispersity Index (PDI)
	($\mu\text{m}/\text{sec}$)	(particle/sec)			
B3-L	0.20	0.045	27.6	6.2	2.48
B3-R	0.14	0.043	19.4	6.3	1.63
B3-S	0.10	0.038	13.0	6.0	1.76

4.3.3 End-labeling Composite Particles for Use as Micromotors

The series of rhombohedral PRINT particles were studied as potential engineered micromotors. Three aspect ratios were used: 0.4, 2.1 and 2.5 (B1, B2 and B3, respectively), and all of the particles contained 10 wt % magnetite aligned parallel to the height of the

particles (perpendicular to the plane of the mold). Catalytic micromotors require the asymmetric placement of a catalyst,¹⁰ so one end of the rhombohedral PRINT particles was functionalized with platinum, Pt. It is well-known that Pt catalyzes the decomposition of hydrogen peroxide (H_2O_2) to water and oxygen. This reaction has been exploited to power the motion of nano- and microobjects in solution, though there is some dispute as to the mechanism of motion, whether due to bubble formation¹¹ or self-diffusiophoresis.¹² It was observed that the Pt-capped, magneto-polymer PRINT particles were definitely motile in H_2O_2 solution. Moreover, it was found that the motion was linear and directed away from the Pt end of the particle. Similar to the boomerang-shaped particles described above, Fe_3O_4 present in the Pt end-capped particles provided a mechanism for changing the direction of the particles in solution. The direction of a B3 particle, containing magnetite chained along the long axis of the rod, was changed by moving a strong permanent magnet around the microscope stage. The particle responded immediately to the change in position of the magnet, and thus was able to be steered accurately. The dye was placed on the same end of the particle as the Pt to clearly illustrate that the motion is directed away from the Pt end (Figure 4.17).

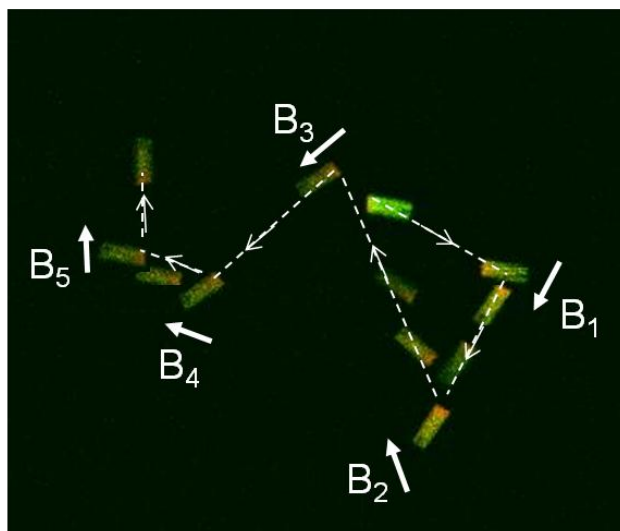


Figure 4.17. Overlaid image showing the path of a magnetically-guided micromotor in 30 % hydrogen peroxide solution. The motor, which exhibits linear translational motion, turns when the magnetic field changes direction. The platinum end of the particle was chemically functionalized with a red dye for ease of visualization.

Particle motion was observed as a function of the particle aspect ratio (0.4, 2.1, and 2.5) and H_2O_2 concentration (0%, 10%, 20%, 30%). The particles were tracked in the presence of a stationary or rotating magnet; due to the microscope configuration, the magnet was located off-center above the solution (Figure 4.3, Section 4.2.6). For the stationary magnet experiments, at 0% H_2O_2 , all of the particles exhibited small random movements due to Brownian motion. With increasing H_2O_2 concentration, the particles were propelled linearly through solution, and for each particle aspect ratio, the particle velocities were the same (within error, Table 4.3) with increasing H_2O_2 concentrations. It was expected that the smallest particle, the B1 blocks, would be the fastest, however, they appeared to move slower than the B2 blocks. This was because the motion of the lowest aspect ratio particles was somewhat irregular, and they tended to change direction rapidly, unlike the more elongated particles. The B3 blocks were the slowest, which was expected because they were the largest in the particle series.

For the rotating magnet experiments, at 0 % H₂O₂ the particles rotated at the same speed as the magnet about their axes with no lateral motion. In the presence of H₂O₂, all of the particles tended to travel a prolate cycloid path. The particle tracks for both the stationary and rotating magnet experiments are presented in Figure 4.18. This unique motion occurred because the particles were experiencing both a linear force due to H₂O₂ decomposition as well as the torque from the rotating magnet located off to one side of the solution. In addition, the particle velocities were found to be significantly slower than in the presence of the stationary magnet. Furthermore, as a comparison, traces of particles with a random magnetic moment are also shown in Figure 4.18. These particles did not respond as well to the rotating magnetic field and generally showed only a small perturbation. It is believed that this is due to a reduction in the net magnetic moment of the particles when compared to particles cured in a magnetic field.

Table 4.3 Particle translational velocities for all particle sizes under a stationary magnetic field (no field) with varying solutions of H₂O₂.

Particle Size (μm)	% H₂O₂	Average Translational Velocity (μm/s)
2 × 2 × 1	0	0.25 ± 0.07
2 × 2 × 1	10	28.49 ± 10.76
2 × 2 × 1	20	22.14 ± 7.83
2 × 2 × 1	30	27.29 ± 12.21
2 × 2 × 4	0	0.21 ± 0.06
2 × 2 × 4	10	54.88 ± 12.94
2 × 2 × 4	20	47.30 ± 21.15
2 × 2 × 4	30	56.97 ± 28.49
2 × 2 × 6	0	0.93 ± 0.19
2 × 2 × 6	10	22.62 ± 5.84
2 × 2 × 6	20	16.33 ± 8.17
2 × 2 × 6	30	22.96 ± 13.25

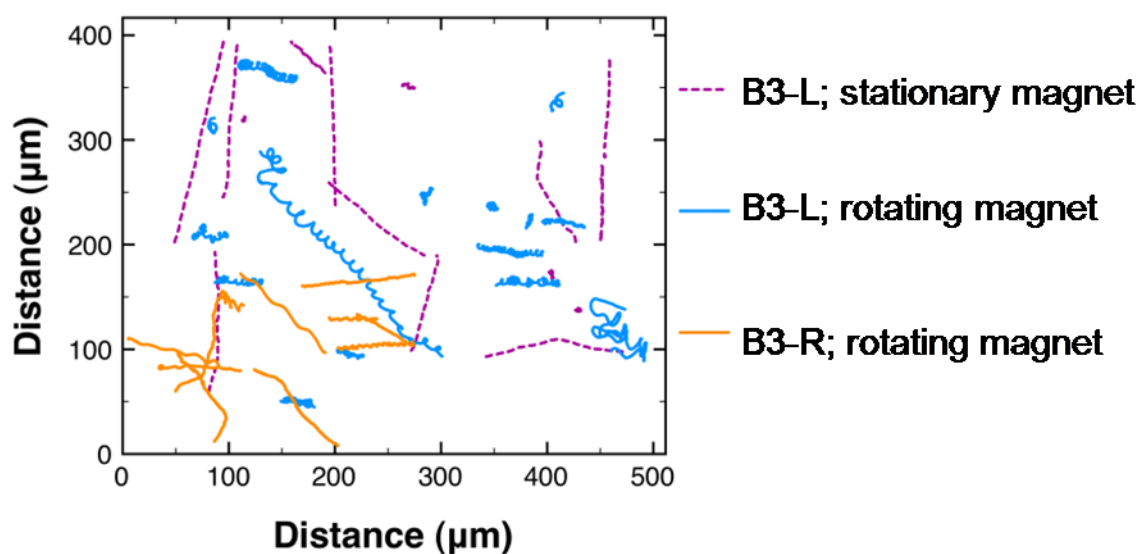


Figure 4.18. Traces of B3 particles with random magnetic moments (orange) in a rotating magnetic field overlaid with particles with magnetic moments parallel to the long particle axis in 30% H₂O₂ in a stationary (dotted) and rotating (solid) magnetic field.

4.4 Summary and Future Outlook

Using the PRINT process, precisely defined composite magnetic micro- and nanoparticles were fabricated, and manipulated magnetically. The magneto-polymer nanoparticles represent the only published examples of shape and size specific magneto-polymer composite nanoparticles fabricated by a top-down method.¹³ In the future, smaller and more highly magnetic PRINT nanocomposites should be examined for improved properties. Given the shape and size control, these composite nanoparticles are very promising candidates for different life science applications, for example as multifunctional delivery and imaging agents.

PRINT magneto-polymer composite microparticles were fabricated with both random and nanostructured magnetite within the particles. This level of shape control combined with internal nanostructural control has not been previously demonstrated for magnetic composite

particles.¹³ One important aspect of this work is the ability to take a polydisperse, non-uniform commercial magnetite sample and combine it with the PRINT process to create novel composite particles with magnetic properties distinct from the precursor nanoparticles, due to controlled aggregation and orientation strategies. The magnetic manipulation of these composite particles in solution has been demonstrated. The regiospecific functionalization of these particles with an amine reactive organic dye (for tracking purposes) and deposited platinum for use as self-propelled micromotors in H₂O₂ was also achieved. This work will potentially open the door to new, exciting applications in magnetic colloids and micro- and nanomotors and machines.

4.5 References

1. Geng, Y.; Ahmed, F.; Bhasin, N.; Discher, D. E. *J. Phys. Chem. B* **2005**, 109, 3772-3779.
2. Park, J.-H.; von Maltzahn, G.; Zhang, L.; Schwartz, M. P.; Ruoslahti, E.; Bhatia, S. N.; Sailor, M. J. *Adv. Mater.* **2008**, 20, 1630-1635.
3. Zhu, J.; Hayward, R. C. *J. Am. Chem. Soc.* **2008**, 130, 7496-7502.
4. Hwang, D. K.; Dendukuri, D.; Doyle, P. S. *Lab Chip* **2008**, 8, 1640-1647.
5. Gratton, S. E. A.; Williams, S. S.; Napier, M. E.; Pohlhaus, P. D.; Zhou, Z.; Wiles, K. B.; Maynor, B. W.; Shen, C.; Olafsen, T.; Samulski, E. T.; DeSimone, J. M. *Acc. Chem. Res.* **2008**, 41, 1685-1695.
6. Herlihy, K. P.; Nunes, J.; DeSimone, J. M. *Langmuir* **2008**, 24, 8421-8426.
7. Merkel, T.; Herlihy, K.; Nunes, J.; Orgel, R.; DeSimone, J. M. *Langmuir* **2009**, in press.
8. Rolland, J. P.; Maynor, B. W.; Euliss, L. E.; Exner, A. E.; Denison, G. M.; DeSimone, J. M. *J. Am. Chem. Soc.* **2005**, 127, 10096-10100.
9. Zhang, H.; Nunes, J. K.; Gratton, S. E. A.; Herlihy, K. P.; Pohlhaus, P. D.; DeSimone, J. M. *New J. Phys.* **2009**, 11, 075018.
10. Paxton, W. F.; Sundararajan, S.; Mallouk, T. E.; Sen, A. *Angew. Chem. Int. Ed.* **2006**, 45, 5420-5429.
11. Gibbs, J. G.; Zhao, Y. P. *Appl. Phys. Lett.* **2009**, 94, 163104.
12. Howse, J. R.; Jones, R. A. L.; Ryan, A. J.; Gough, T.; Vafabakhsh, R.; Golestanian, R. *Phys. Rev. Lett.* **2007**, 99, 048102.
13. Nunes, J.; Herlihy, K. P.; Mair, L.; Superfine, R.; DeSimone, J. M. *Nano Lett.* **2010**, 10, 1113-1119.

Chapter 5

Hierarchically-Controlled PRINT Composite Thin Films

5.1 Specific Research Objectives

One area in which the manipulation of colloidal particles is important as it relates to the strategic placement of particles is in the engineering of highly structured composite films. As described in Chapter 1, there are many routes towards controlling the placement of colloidal particles in a medium, from the more autonomous routes where the design of the particle determines assembly and organization to more externally directed routes, such as the use of electric, magnetic and optical fields. This work explored a novel and distinctive approach to the fabrication of polymer composite films. The fabrication utilized the precise particle array-generating capabilities of the PRINT[®] process to fabricate composite films where particle aggregation can be completely eliminated. In this study, the particles were meticulously designed to possess desired shape, size, composition and orientation properties. In addition, particle location in two dimensions was exactly defined by a template. Because of the extensive control of particle properties and location, it was possible to control the nanostructure of the composite film. This study explored the range of polymer composite film compositions that can be fabricated with this approach, including all-organic and polymer/ceramic composites.

All-organic composite films were fabricated in a range of compositions and particle sizes, and the process was optimized for both crosslinked and thermoplastic polymer matrices and particles. Polymer/ceramic ordered composite films were also fabricated with the PRINT process. These composite films are also of high interest in the materials science field, as the piezoelectric material in electromechanical transducers, gate insulators in organic field-effect transistors, high energy density capacitors, and other electronic devices.¹⁻⁴ A variety of inorganic oxide particle arrays were fabricated with the PRINT process, including tin oxide, zinc oxide, titanium dioxide and indium tin oxide,⁵ though in this work, specific emphasis was placed on the

polymer/barium titanate (BaTiO_3) composite film for its potential as the dielectric film in capacitors. Various methods for fabricating polymer/ BaTiO_3 composite films have been reported in the literature.⁶⁻⁸ One successful approach has been the surface functionalization of commercially available BaTiO_3 nanoparticles with tailored organic phosphonic acid ligands to uniformly disperse high volume fractions of the nanoparticles in different polymer matrices.⁷ The dielectric properties of these composite films strongly depend on the size and shape of the crystallites, as well as the volume fraction of the particles.^{9, 10}

A great qualitative tool for assessing the quality of film nanostructure is microscopy: optical, confocal and electron microscopy and so these techniques are used extensively in this work to study the micro- and nanostructure of the ordered composite films. Additionally, the films were characterized with Thermogravimetric Analysis (TGA). For the polymer/ BaTiO_3 composite films, dielectric properties were also assessed.

5.2 Experimental

5.2.1 Materials and Instrumentation

Unless otherwise stated, all reagents were purchased from Sigma-Aldrich and used as received. The PFPE mold precursor (Fluorocur[®]) was supplied by Liquidia Technologies. 2,2'-diethoxyacetophenone (DEAP) was used as photoinitiator for all UV polymerizations. The monomers: poly(ethylene glycol) dimethacrylate (PEG-DMA; $M_n = 550$ g/mol and 750 g/mol), trimethylolpropane ethoxylate triacrylate (TMPTA; $M_n = 912$ g/mol) and 1-vinyl-2 pyrrolidone were deinhibited with adsorption alumina prior to adding the photoinitiator (0.5 wt% DEAP). Poly[2-methoxy-5-(3',7'-dimethyloctyloxy)-1,4-phenylenevinylene] (MDMO-PPV) ($M_n = 23,000$ g/mol) was solution processed as a 2 wt% solution in chlorobenzene. Polystyrene (PS; $M_n = 10,000$ g/mol) was solution processed as a 35 wt% solution in

tetrahydrofuran. Polycarbonate (PC; $M_n = 45,000$ g/mol) was solution processed as a 6 wt% solution in chloroform (Fisher Scientific). Poly(vinylidene fluoride) (PVDF; $M_n = 107,000$ g/mol) was used as an 8 wt% solution in either dimethylformamide (DMF, Fisher Scientific) or methylethylketone (MEK, Fisher Scientific). The epoxy system used was a commercial 5-minute 2-part epoxy adhesive (Fisher Scientific). Barium titanate was synthesized using the following reagents: barium acetate, glacial acetic acid (Fisher Scientific), titanium^{IV} isopropoxide, acetylacetone and 2-methoxyethanol. Sodium chloride disks (25×4 mm NaCl) were purchased from Harrick Scientific. Single crystalline (100) magnesium oxide substrates (1"×1"×0.02" MgO) were purchased from Coating and Crystal Technology, Inc. Magnesium oxide was also sol-gel synthesized using magnesium nitrate hexahydrate ($Mg(NO_3)_2 \cdot 6H_2O$) and polyvinylpyrrolidone (PVP, Acros, $M_n = 58,000$ g/mol). Silicon wafers (Silicon quest) were cleaned using piranha solution, which was composed of 70 % concentrated sulfuric acid and 30 % hydrogen peroxide. Fluorinert FC40 was used as a high dielectric strength liquid for breakdown voltage measurements.

Scanning Electron Microscope (SEM) images were taken on a Hitachi S-4700 SEM and environmental SEM (ESEM) micrographs were taken on a FEI Quanta 200 FEG instrument using a backscattered electron detector. Fluorescence images were taken on a Zeiss Axioskop 2MAT incident light microscope fitted with an AxiCam MRM digital camera. Confocal images were taken on a Zeiss LSM5 Pascal Confocal Laser Scanning Microscope. Dynamic Mechanical Analyzer (DMA) measurements were performed using a Perkin Elmer Pyris Diamond DMA in tension mode at a frequency of 1 Hz. TGA measurements were performed on a Perkin Elmer Pyris I Thermogravimetric Analyzer, heating from 25 °C – 600 °C at a heating rate of 10 °C/min in a nitrogen atmosphere.

Capacitance measurements were made on an Agilent LCR meter sweeping frequencies from 1 kHz – 1 MHz. Thermoplastic samples were melt-pressed using a hydraulic press (PHI Manual Hydraulic Compression Press, 155 °C, 1100 psi). X-ray diffraction was done using a Powder X-ray Diffractometer (XRD, Rigaku) using Cu K α radiation. FTIR spectra were obtained from an Attenuated Total Reflectance Fourier Transform Infrared Microscopy (ATR FTIR, Bruker Tensor 27).

5.2.2 Ordered Composite Film Fabrication and Characterization

Numerous examples of composite films have been generated with this approach. There are four main composite film categories: crosslinked polymer/polymer, thermoplastic polymer/polymer, polymer/ceramic and polymer/metal systems. The fabrication and characterization of films from each of these categories are described separately in the following sections. Table 5.1 summarizes the composite films fabricated in this work.

Table 5.1. Summary of Ordered Composite Films

Continuous Polymer Phase	Discrete Particle Phase	Examples
crosslinked polymer	crosslinked polymer	poly(ethylene glycol)/poly(ethylene glycol) (PEG/PEG); PEG/ trimethylolpropane ethoxylate triacrylate (PEG/TMPTA); epoxy/TMPTA
crosslinked polymer	thermoplastic polymer	PEG/polyvinylpyrrolidone; PEG/ MDMO-PPV; PEG/ polystyrene; PEG/poly(methyl methacrylate)
thermoplastic polymer	crosslinked polymer	polycarbonate/PEG (PC/PEG), poly(vinylidene fluoride)/PEG (PVDF/PEG)
thermoplastic polymer	ceramic	PC/BaTiO ₃ ; PVDF/BaTiO ₃
crosslinked polymer	ceramic	PFPE/BaTiO ₃
thermoplastic polymer	metal	PC/silver

5.2.2.1 Crosslinked Polymer/Polymer Systems:

5.2.2.1.1 Fabrication

The PFPE molds were fabricated and filled with particle monomer solutions using capillary filling and film splitting techniques described in Chapter 2 and elsewhere.¹¹⁻¹³ For the crosslinked matrix systems, a thin film of the continuous phase pre-polymer, for example a poly(ethylene glycol) dimethacrylate (PEG-DMA), was used as the adhesive to remove the particles from the mold. Additional continuous phase polymer was cast onto the array to cover the particles, and acted as the adhesive for a second layer of particles. This simple step was performed repeatedly to increase the composite thickness. The thickness of each layer, which was easily tuned by adjusting the spin coating parameters, dictated the vertical spacing between particles. Adjusting the layer thickness was one method used to control the particle volume fraction, where for example a minimum film thickness equal to the height of the particles in that layer would result in the maximum possible particle volume fraction for a given 2-D array and desired overall film thickness. Other film casting methods, such as the use of a Meyer rod, have also been successfully applied to control the layer thickness. This process was used to fabricate a variety of polymer/polymer composite films, and is described schematically in Figure 5.1.

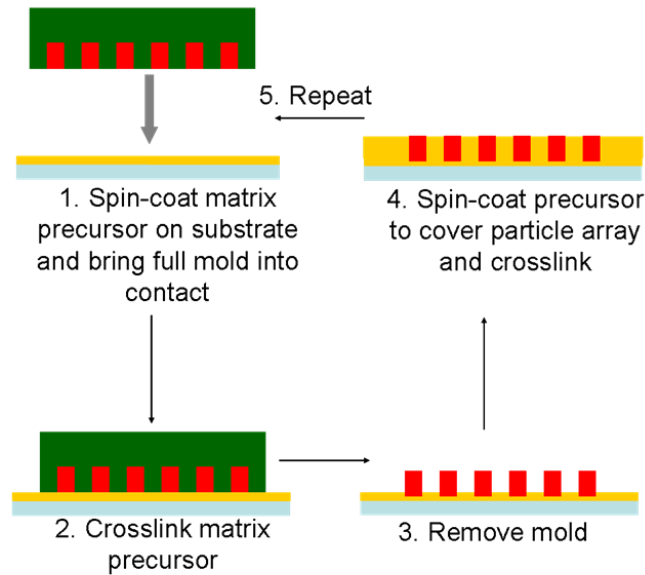


Figure 5.1. Simplified fabrication scheme for crosslinked PRINT composite films

5.2.2.1.2 Characterization

Composite films were generated with thermoplastic particles, such as polyvinylpyrrolidone (PVP), polystyrene (PS), poly(methyl methacrylate) (PMMA), and the semi-conducting polymer, MDMO-PPV. Thermoset particles, such as crosslinked trimethylolpropane ethoxylate triacrylate resin, were also incorporated into the composite. The composition of the continuous phase included both PEG-DMA and epoxy crosslinked systems. Typically, the final composite films were approximately 2 square inches large, though films were fabricated with dimensions as large as 6 inches.

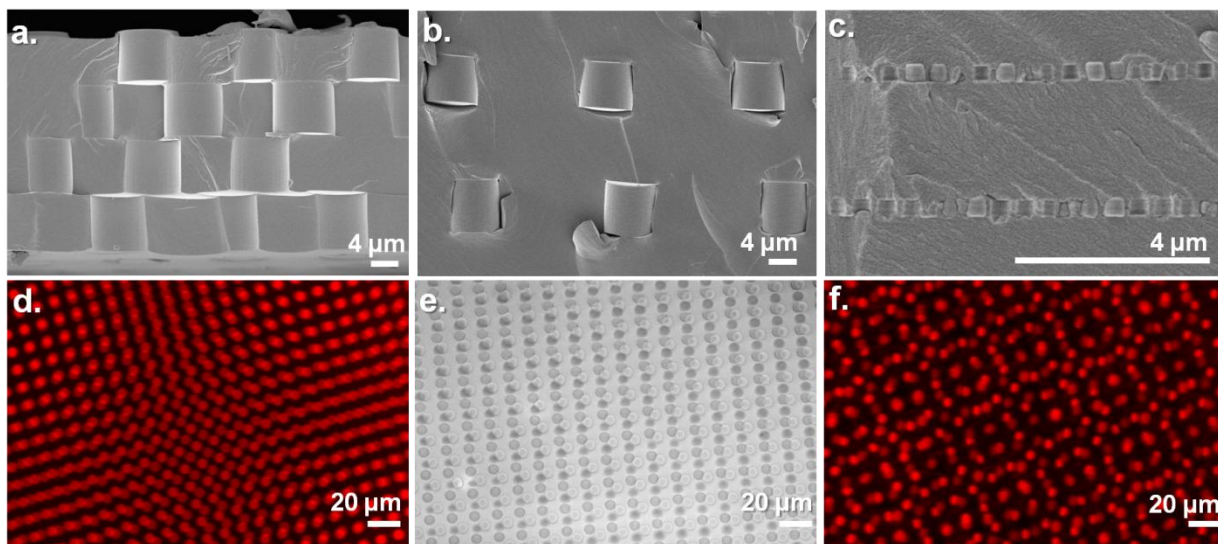


Figure 5.2. (a-c) SEM images of film cross-sections and (d-f) top-view optical/fluorescence images of composite films. The examples are (a) a PEG/triacrylate resin composite film with 7 μm cylindrical triacrylate particles, (b) is an epoxy/triacrylate resin composite film with 7 μm cylindrical triacrylate particles, (c) is a PEG/triacrylate resin composite film with 200 nm cylindrical triacrylate particles, (d) is a PEG/triacrylate resin 2-layer composite film with 7 μm cylindrical triacrylate particles (rhodamine B dye used in particles for imaging), (e) is a PEG/PS 3-layer composite film with 7 μm cylindrical PS particles and (f) is a PEG/MDMO-PPV 2-layer composite film with 7 μm cylindrical MDMO-PPV particles.

The microstructure of the PRINT composite films was evident when the films were sectioned and imaged with SEM. In Figures 5.2a-c, the regular arrangement of uniform, cylindrical triacrylate resin particles is clearly identifiable in the continuous epoxy and PEG-DMA matrices. Size control was demonstrated by varying the particle size from 7 μm to 200 nm. Particle packing within each layer was also controlled, as demonstrated by the square lattice arrangement of the 7 μm cylinders and the hexagonal packing of the 200 nm cylinders. The particle dimensions, horizontal particle spacing, and arrangement of the particles within each layer were precisely governed by the silicon master template used to fabricate the mold. This template, which was fabricated using standard photolithography, can be designed to have a preferred particle shape, size, spacing, and pattern with a high degree of spatial

resolution. It is important to note that the particles in the composite films were not registered perpendicular to the plane of the film, as evidenced from the top-view fluorescence and DIC images of composite films with 7 μm cylindrical particles arranged on a square lattice within each layer (Figure 5.2d-f). Complex Moire patterns resulted from the pattern mismatch between layers, suggesting that these films may exhibit interesting optical properties.

The PEG-DMA/PVP ordered composite film was a particularly interesting example because the 1-vinyl-2-pyrrolidone monomer dissolves non-polar compounds such as the antiproliferative agent, Paclitaxel. Angled views of a 3-D confocal microscopy projection of the PEG-DMA/PVP composite (containing 10 wt% Paclitaxel in the PVP particles) is presented in Figure 5.3. PEG is a non-toxic, biocompatible polymer and PVP is a common water-soluble excipient used in drug delivery applications. By varying the cross-link density of the PEG matrix in each layer, the release of the drug could potentially be controlled and sustained, thereby illustrating the potential for this fabrication to be used in generating thin films for local therapeutic treatment.

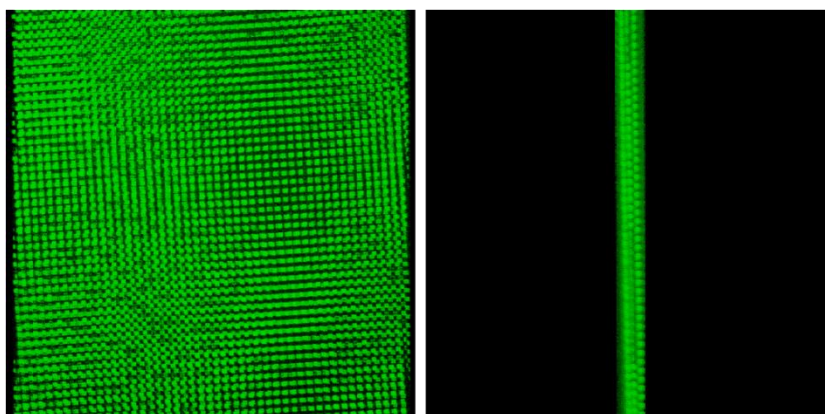


Figure 5.3. Angled views of the 3-D confocal microscopy projection of a PEG/PVP 3-layer composite film with 10 wt% Paclitaxel in the 5 μm cubic PVP inclusions (fluorescein *o*-acrylate dye used in particles for imaging)

One means of quantitatively characterizing these films is to use thermal analysis. Thermogravimetric analysis (TGA). For example, the thermal degradation of a PEG/PS composite film containing 7 μm cylindrical PS particles was compared to that of pure PEG and pure PS. Pure PS and pure PEG exhibited 5% weight loss temperatures at 363 $^{\circ}\text{C}$ and 302 $^{\circ}\text{C}$, respectively. The PEG/PS composite film, on the other hand, exhibited a 5% weight loss temperature of 240 $^{\circ}\text{C}$, with a distinct secondary decomposition at approximately 340 $^{\circ}\text{C}$. The shape of the TGA trace clearly indicates the presence of two distinct phases (Figure 5.4). Both decomposition temperatures were found to be lower than the pure polymers, suggesting that the composite was not as thermally stable as the pure materials.

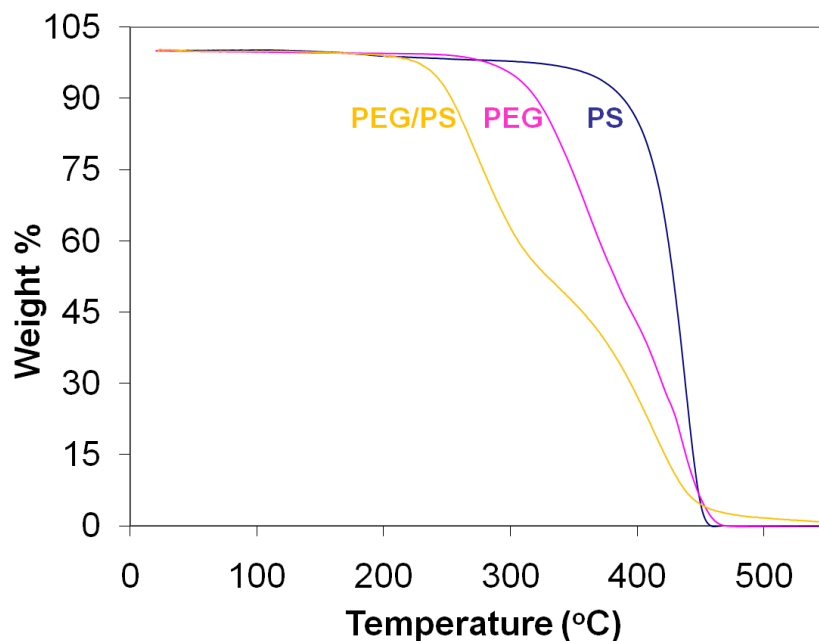


Figure 5.4. TGA decomposition curves for pure PEG, pure PS and the ordered PEG/PS composite film.

Another remarkable advantage of this fabrication process is the ability to separate miscible polymeric systems into well-ordered phases. This can be valuable in fabricating materials with novel release profiles¹⁴ or mechanical properties. For example, two PEG-

DMA monomers of differing molecular weights were used to fabricate a crosslinked ordered composite film with the lower molecular weight monomer ($M_n = 550$ g/mol) as the continuous phase and the higher molecular weight monomer ($M_n = 750$ g/mol) as discrete 5 μm cubic particles. A transparent free-standing 16-layer PRINT composite thin film was fabricated and the presence of the two cross-linked PEG phases with different crosslink densities was confirmed by Dynamic Mechanical Analysis (Figure 5.5). Glass transition temperatures (T_g), determined from $\tan \delta$ peaks, were found to be -38.1 $^{\circ}\text{C}$ and 19.3 $^{\circ}\text{C}$ for pure crosslinked 750 g/mol PEG-DMA and 550 g/mol PEG-DMA, respectively. When the 550 g/mol PEG-DMA and 750 g/mol PEG-DMA monomers were blended to form a homogeneous solution (4:1 volume ratio) and then crosslinked, the gel was found to have a T_g of -0.8 $^{\circ}\text{C}$. Conversely, the PRINT composite, with approximately the same prepolymer volume fraction as the homogeneous blend, had a $\tan \delta$ peak at 18.2 $^{\circ}\text{C}$, comparable to the T_g of 550 g/mol PEG-DMA (the continuous phase of the composite), with a slight shoulder at approximately -35 $^{\circ}\text{C}$, which may be an indication of the 750 g/mol PEG-DMA crosslinked particle domains.

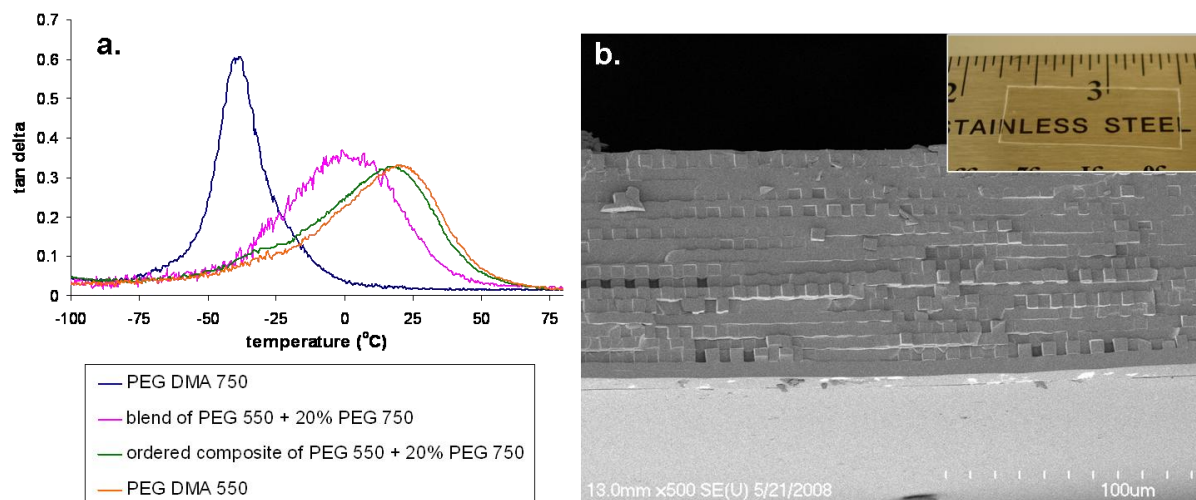


Figure 5.5. Dynamic Mechanical Analysis of an all-PEG composite where (a) shows the $\tan \delta$ curves for pure 750 g/mol PEG-DMA, pure 550 g/mol PEG-DMA, a 4:1 blend of 750 g/mol PEG-DMA and 550 g/mol PEG-DMA and an ordered composite 4:1 750/550 g/mol PEG-DMA, and (b) is an SEM image of the ordered 4:1 750/550 g/mol PEG-DMA composite film cross-section containing 16 particle layers with an inset picture of the transparent film.

5.2.2.2 Thermoplastic Polymer Systems

5.2.2.2.1 Fabrication

One method for fabricating the thermoplastic matrix/crosslinked particles system is illustrated schematically in Figure 5.6. This method was used to fabricate poly(vinylidene fluoride)/PEG (PVDF/PEG) composite films. The PEG particles were harvested onto a sacrificial polymer layer, polyvinylpyrrolidone (PVP). An 8 wt% PVDF in methylethylketone (MEK) solution of the continuous phase was cast onto the harvested array. After evaporating the MEK solvent, the PVP layer was dissolved in water to lift off the PVDF/PEG composite layer. The layer was dried carefully ensuring all solvent was removed, then multiple PVDF/PEG layers were stacked and heated to 175 °C under pressure using a hydraulic press. This method, however, required that the sacrificial polymer layer and the continuous phase polymer (in this example, PVP and PVDF, respectively) have

orthogonal solvent solubilities. For example, this process would not work if PVP were soluble in MEK. To overcome this issue, the particles can be harvested directly onto the continuous phase. As an example, polycarbonate (PC)/PEG composite films were fabricated, where thin PC films (prepared by casting a 8 wt% solution of PC in chloroform) on PET were brought into conformal contact with the full mold of particles and heated above the glass transition temperature of PC. Once cooled, the mold was pulled apart to release the particles onto the PC layer. The layers could then be stacked and melt-pressed at 155 °C.

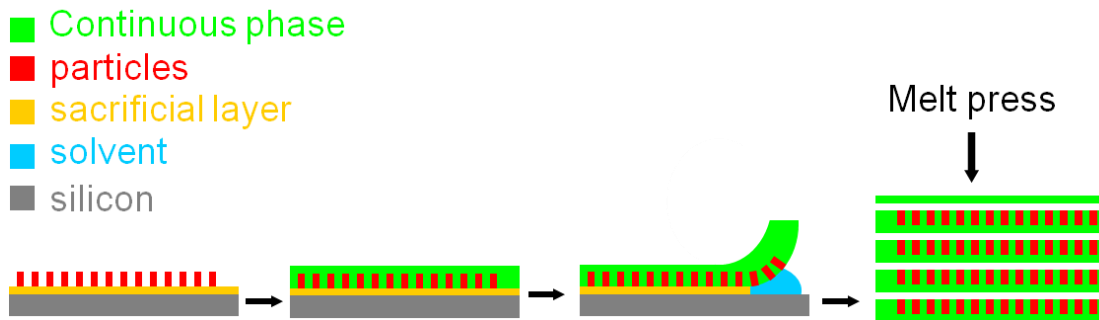


Figure 5.6 Simplified fabrication scheme for thermoplastic PRINT composite films

The fabrication process can be made continuous by replacing the layer stacking step with a rolling process, where the layer is collected and stacked at the same time. This was investigated on a very small scale using a capillary tube as the cylindrical substrate. The tube was coated with an adhesive (carbon tape) and one end of the composite layer was stuck to the tube. The tube was then gently rolled to collect the layer onto the tube. Once the layer was completely wrapped around the tube, it was tightly wrapped in foil and heated to consolidate the layers. The multilayer composite film was then removed from the tube and imaged. Figure 5.7 describes this modification.

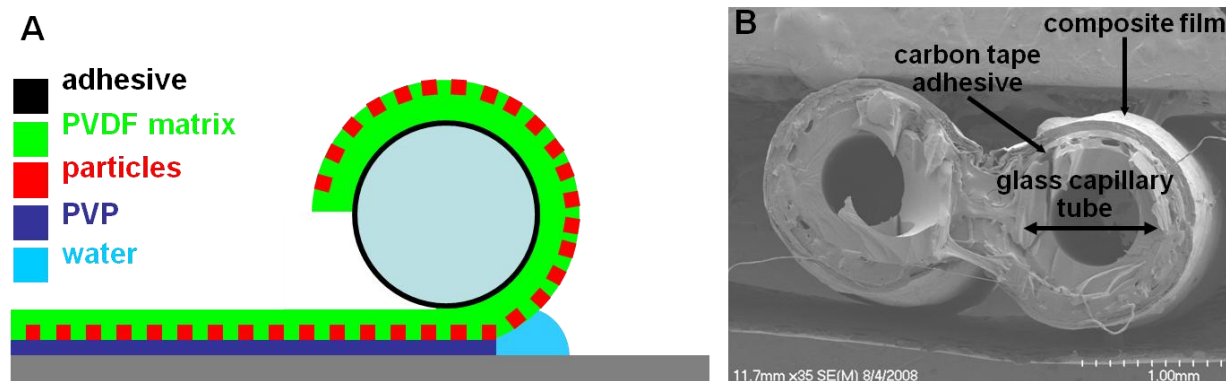


Figure 5.7. (A) Simplified fabrication scheme for continuous thermoplastic PRINT composite films and (B) cleaved capillary tube with ordered composite PVDF/PEG composite film wrapped around it.

5.2.2.2.2 Characterization

The thermoplastic composite films were analyzed using microscopy. A series of PVDF/PEG composite films were fabricated using the continuous fabrication method, where the aspect ratio of the particles was increased from 0.25 to 0.5 to 1 (Figure 5.8). As demonstrated by Figure 5.8, the films were successfully fabricated but the particle order within the layers was not well preserved in some cases. This may have been due buckling of the layer while it was being wound around the cylindrical substrate. For this method to work well, the composite layer has to be held taut as it is wrapped around the tube, which is difficult to do on such a small scale. The method, though, holds much promise as a potential route on a much larger scale.

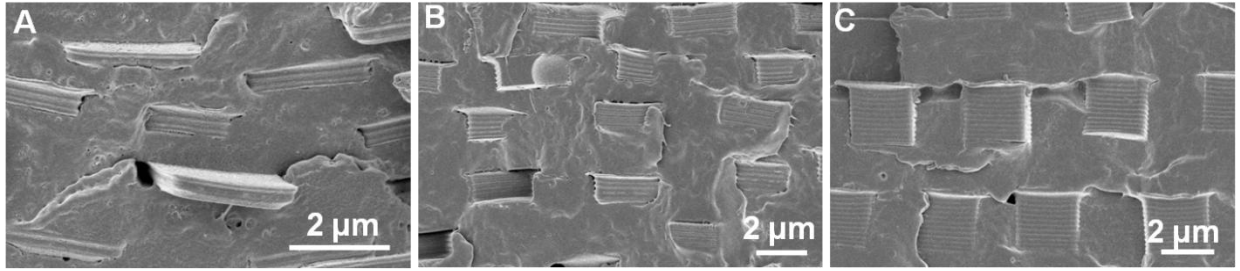


Figure 5.8. SEM images of cross-sections of PVDF/PEG composite films where the $3 \times 3 \mu\text{m}$ PEG particles have increasing aspect ratio: (A) 0.25, (B) 0.5 and (C) 1.

Particle orientation of highly anisotropic particles within the composite films can be controlled with this PRINT composite fabrication process, by rotating the individual layers prior to lamination. For example, two bilayer polycarbonate (PC) films containing highly anisotropic rectangular rod ($20 \times 4 \times 5 \mu\text{m}$) PEG-DMA cross-linked particles were fabricated: one with particle layers oriented parallel to each other and the other with particle layers oriented perpendicular to each other. To fabricate these composites, the free-standing PC/particle layers were stacked either with particles oriented in the same direction or one layer was rotated 90° , so that the particle layers were orthogonal. The layers were laminated at 155°C , above the glass transition temperature (T_g) of PC (T_g of PC = 150°C). Confocal microscopy was used to analyze the films (Fig. 5.9). Figure 5.9a shows the film with parallel layers – as can be observed in the 3-D projection and the z-slices, the particle layers are pointing in the same direction ($\pm 5^\circ$). Conversely, in Figure 5.9b the particles in the two layers are clearly orthogonal.

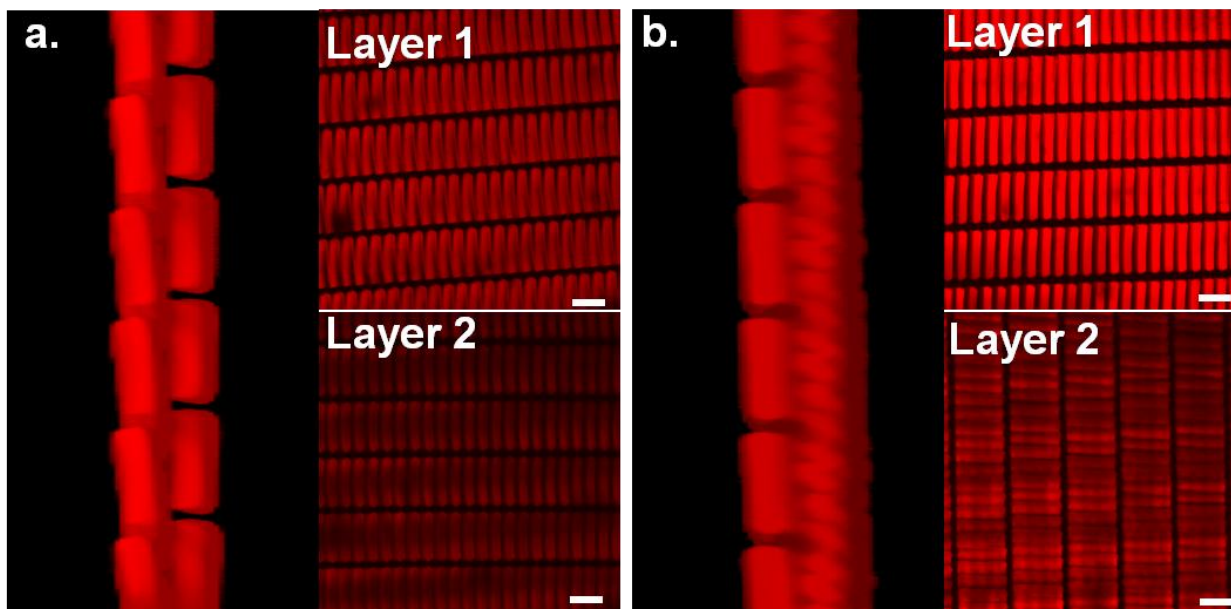


Figure 5.9. Confocal microscopy study of ordered PC/PEG bilayer composite films showing two different relative layer orientations where in (a) both particle layers are parallel and in (b) the particle layers are perpendicular. Scale bars represent 10 μm .

5.2.2.3 Polymer/Barium Titanate

5.2.2.3.1 Barium Titanate Sol-gel Synthesis

The BaTiO_3 sol was prepared by first dissolving barium acetate in glacial acetic acid (42 wt%) at 80 $^\circ\text{C}$. In a separate vessel, equimolar amounts of titanium^{IV} isopropoxide (equimolar to barium acetate) and acetylacetonone were combined. The two solutions were mixed and the sol was cooled to room temperature while stirring. The sol was diluted with 15 wt% 2-methoxyethanol, then filtered through a 0.45 μm syringe filter.

5.2.2.3.2 Bulk Ceramic Synthesis and Characterization

Bulk BaTiO_3 powder samples were characterized with an X-ray Diffractometer. XRD confirmed the presence of cubic crystalline BaTiO_3 . The spectrum is shown in Figure

5.10. Thin films of the xerogel and ceramic BaTiO₃ were also analyzed with ATR FTIR microscopy (Figure 5.11). The xerogel spectrum had a broad band around 3400 cm⁻¹, indicative of acid and alcohol groups, bands around 3000 cm⁻¹ – 2900 cm⁻¹, characteristic of CH₂ and CH₃ groups, and bands at 1550 cm⁻¹ and 1415 cm⁻¹, due to the COO groups that have chelated Ti and Ba. Most of these bands disappear after calcination, and the following peaks characteristic of BaTiO₃ crystalline ceramic appear: a small band around 3500 cm⁻¹, suggesting the presence of surface OH groups, and a band at 1144 cm⁻¹ due to Ti-OH stretching.¹⁵

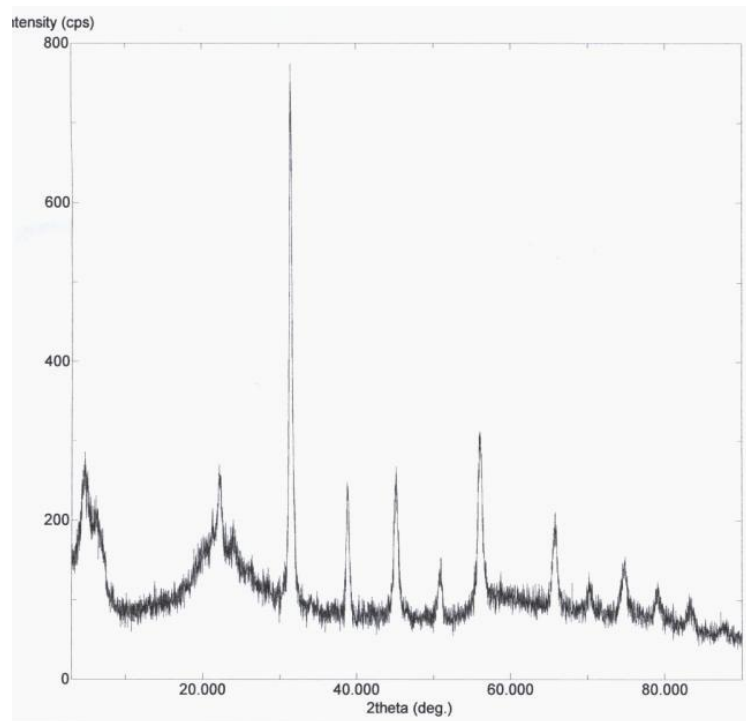


Figure 5.10. XRD spectrum for sol-gel derived BaTiO₃ powder.

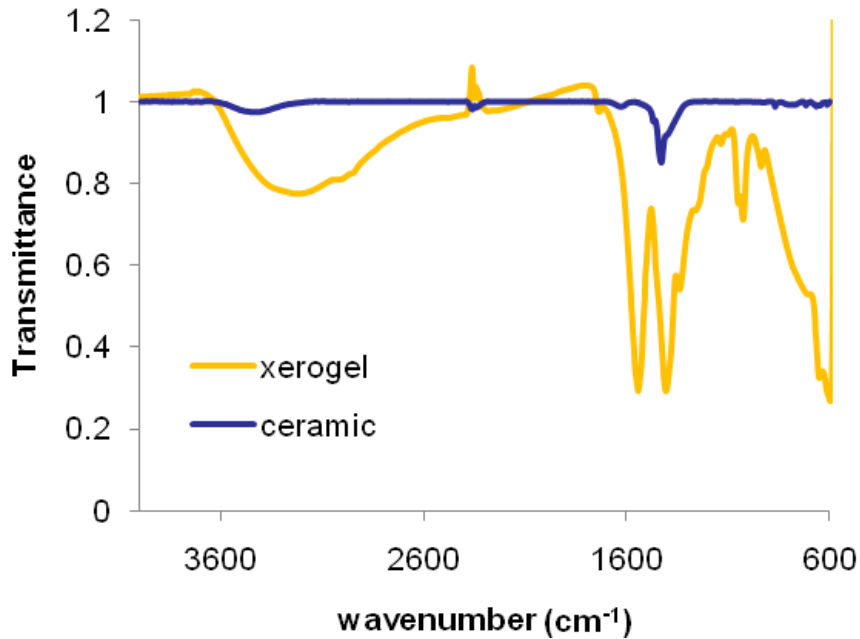


Figure 5.11. FTIR Spectrum of BaTiO₃ xerogel and ceramic films

5.2.2.3.3 BaTiO₃ Particle Array Fabrication and Characterization

Different substrates were used in the BaTiO₃ particle array fabrication including: silicon, sodium chloride (NaCl), and single crystal magnesium oxide (MgO). MgO was chosen because it is lattice-matched with many ferroelectric and superconducting materials.¹⁶ MgO was found to be the best surface for the process, but due to the costliness of single crystal MgO substrates, polycrystalline sol gel derived MgO was prepared. The lattice-matching properties were no longer relevant as the films were polycrystalline, however, the sol-gel derived MgO substrates still worked best with the BaTiO₃ particles. The MgO sol was prepared by dissolving 8.3 wt% magnesium nitrate hexahydrate (Mg(NO₃)₂·6H₂O) and 16.7 wt% polyvinylpyrrolidone (PVP, Acros, M_n = 58,000 g/mol) in distilled water (75 wt%). Silicon wafers were cleaned in piranha solution prior to film deposition. The MgO sol was spin coated onto the wafer and heated to 485 °C for 5 minutes. This was repeated 4

times to build up a MgO film thickness of approximately 200 nm. The final film was annealed at 800 °C for 1 hour.

To assess whether the BaTiO₃ sol would mold well, embossed BaTiO₃ films were fabricated. Figure 5.12 shows nanometer and micron-sized features successfully replicated in BaTiO₃ films. To fabricate scum-free particle arrays, the PFPE molds were first capillary filled with the BaTiO₃ sol. The sol in the mold cavities was converted to the xerogel by heating to 85 °C, where the particles were able to retain the mold features. The xerogel particles were harvested with a thin layer of polycyanoacrylate adhesive onto the MgO-coated silicon wafer. After harvesting, the array was heated in air to 700 °C for 1 hour to calcine and crystallize the ceramic particles then cooled to room temperature at a rate of 10 °C/min. In Figure 5.13, discrete BaTiO₃ particle arrays in MgO-coated silicon were analyzed with Energy Dispersive Spectroscopy (EDS). The elemental line scans and mapping clearly demonstrate that the cubic BaTiO₃ features were not connected to one another on the MgO substrate.

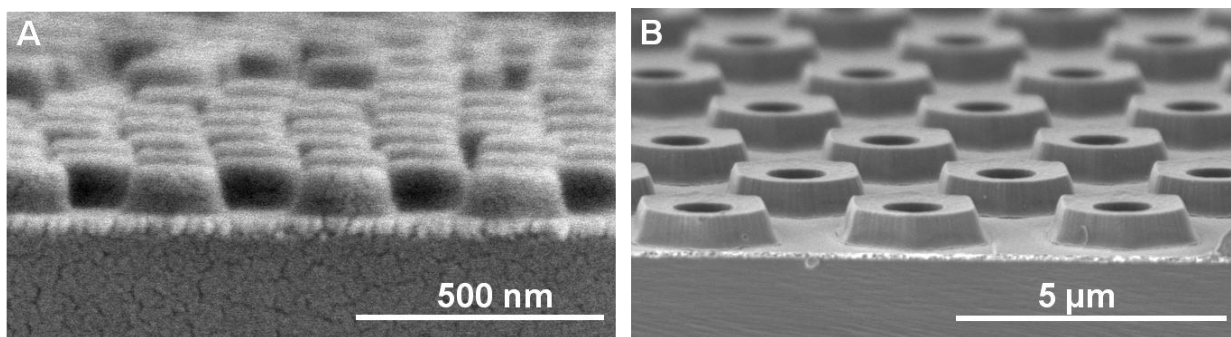


Figure 5.12. SEM images of BaTiO₃ embossed films fabricated from (A) a 200 × 200 nm template and (B) a 3 μm hexnut template.

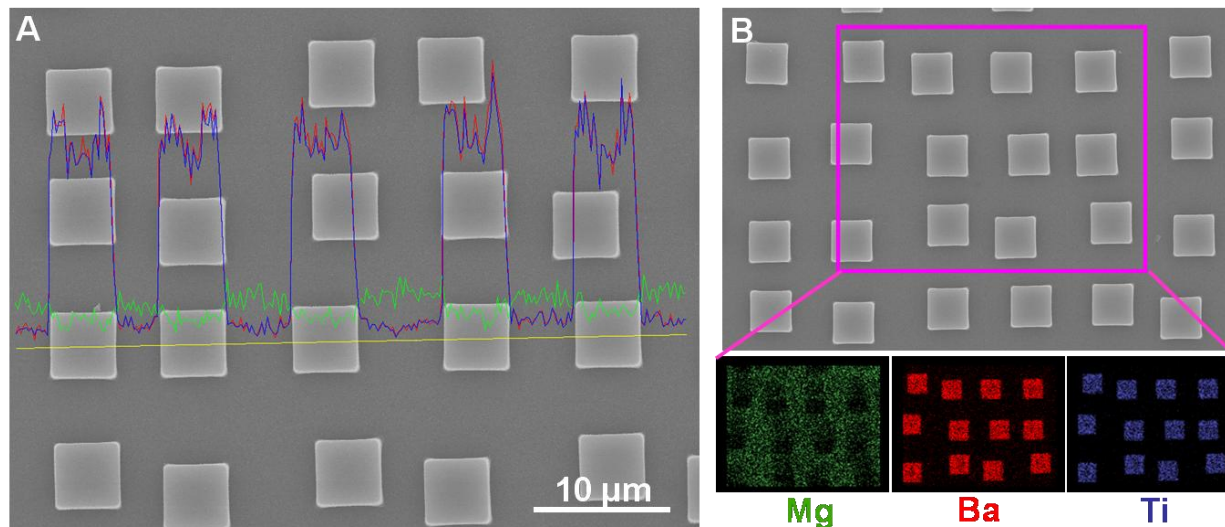


Figure 5.13. SEM images of scum-free BaTiO₃ cubic particles analyzed with Energy Dispersive Spectroscopy, where (A) shows line scans and (B) elemental mapping indicating the presence of Mg, Ba and Ti.

An important characteristic of the calcination step was a 50 % reduction in both the height and width of the particles. After conversion of the sol to the xerogel, the mold feature dimensions were replicated well in the xerogel particles. Converting from the xerogel to the polycrystalline ceramic however, resulted in feature shrinkage as shown in Figure 5.14, where xerogel cylinders with 4.5 μm diameter and 3 μm height were converted to short disk-like particles with a 2.5 μm diameter and 0.9 μm height. Thus, in order to fabricate features of a desired size, templates were used that had feature dimensions double the desired size.

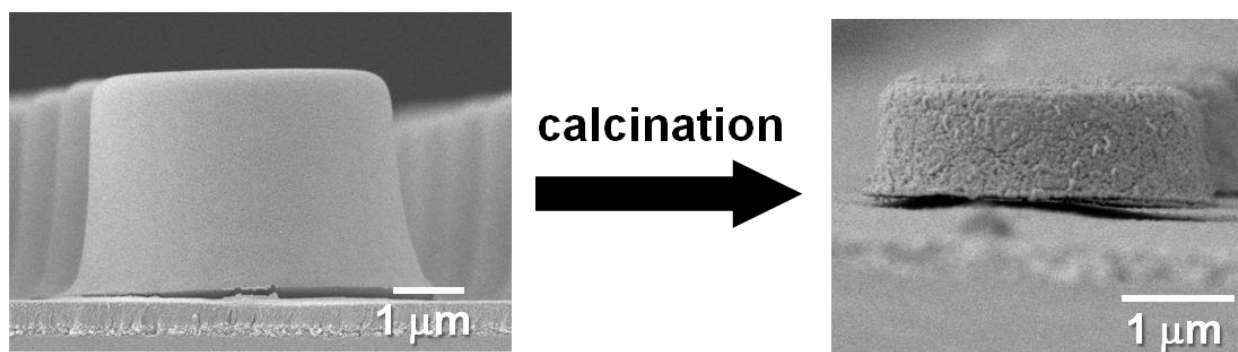


Figure 5.14. SEM images showing the shrinkage that occurs in the conversion of the BaTiO₃ xerogel (at left) to the polycrystalline ceramic (at right)

5.2.2.3.4 Polymer/BaTiO₃ Composite Film Fabrication and Characterization

The fabrication of polymer/BaTiO₃ composite films is illustrated schematically in Figure 5.15. The fabrication is very similar to that described previously for the thermoplastic polymer composite films, but instead of a polymer sacrificial layer, an inorganic sacrificial layer (MgO) was required. Crosslinked matrices, for example PFPE, were used as well with the ceramic particles by casting the monomer onto the array, partially photocuring, and then lifting off. A second layer was added by placing the first partially cured composite layer onto a second array with uncured monomer – the two layers were completely cured and then lifted off. Subsequent layers were added similarly.

Free-standing PVDF/BaTiO₃ composite film examples are shown in Figures 5.15b-d, with 400 × 200 nm, 3 × 0.5 μm and 3 × 2.5 μm cylindrical particles. Similar to the polymer/polymer composite films, the polymer/ceramic composites exhibited exceptionally well-controlled, non-aggregated nano- and microstructure. Starting at the smallest length scale were the nano-sized crystalline domains (10 - 50 nm) of the BaTiO₃ particles (cubic crystalline phase, as determined by XRD), then extending out was another length scale defining the shape of the polycrystalline ceramic particle (nm to μm), followed by the length

scales characterizing the spacing between particles both laterally and vertically (nm to μm), then finally the macroscopic dimensions of the composite film (μm to cm). Thus, these ordered composite films can be controlled and characterized at multiple levels of structural hierarchy.

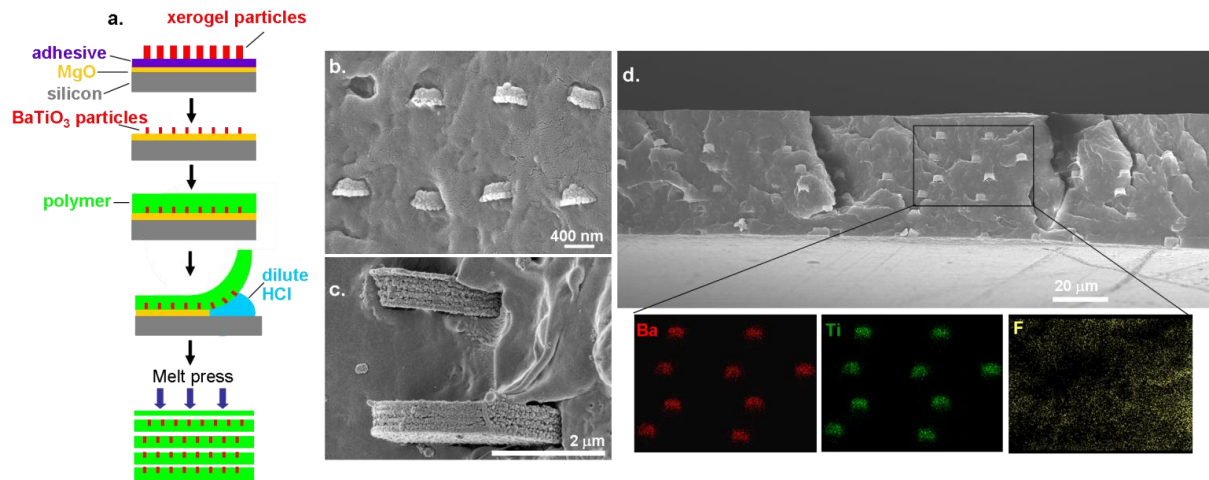


Figure 5.15. Ordered polymer/ceramic composite films showing (a) simple fabrication scheme with SEM images of examples of PVDF/BaTiO₃ film cross-sections with (b) 400 x 200 nm cylinders, (c) 3 x 0.5 μm cylindrical particles and (d) 3 x 2.5 μm cylindrical particles, with Energy Dispersive Spectroscopy elemental mapping identifying the Ba and Ti from the ceramic particles and the F from the polymer.

With the control that the PRINT process affords in composite film fabrication, it is possible to investigate structure – property relationships. A very simple manifestation of this was to vary the BaTiO₃ weight fraction in PC/BaTiO₃ ordered composite films, while maintaining uniform shape, size, spacing, and orientation of the particles, as well as thickness of the composite films, and then monitor the changes in thermal degradation properties of the composite with Thermogravimetric Analysis (TGA). PC/BaTiO₃ films were prepared with 5 × 5 × 2 μm particle inclusions, and the particle shape was a rectangular prism with one concave side (resulting from meniscus formation during mold filling). A series of films were

fabricated with the BaTiO₃ content varying from 0 wt% to 18.4 wt%. The TGA curves exhibited a clear trend in decreasing thermal stability with increasing BaTiO₃ content (Figure 5.16). The decomposition temperature (at 5 % weight loss) decreased linearly with increasing BaTiO₃ wt% except at the highest weight fraction measured.

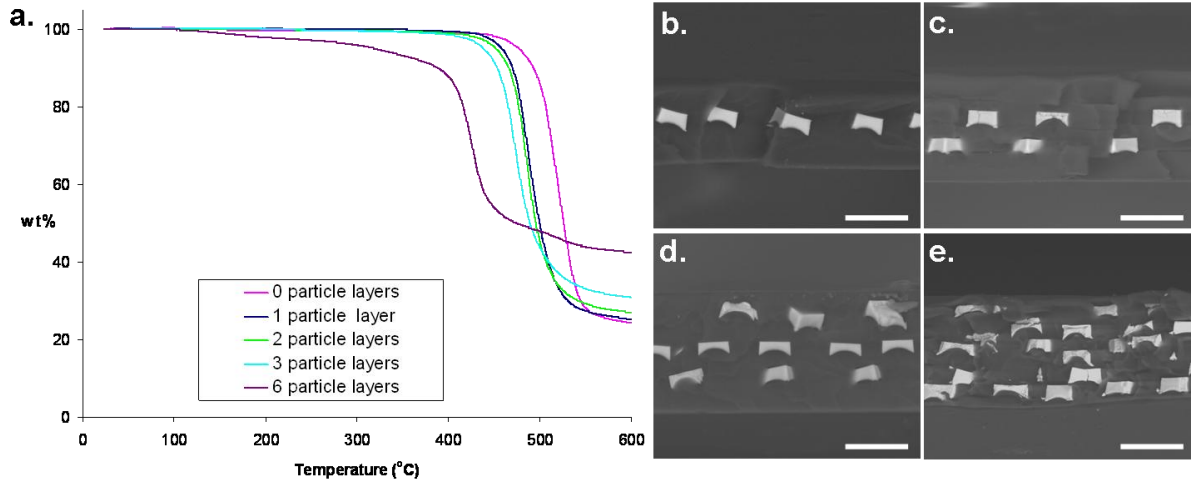


Figure 5.16. TGA study of PC/BaTiO₃ ordered composite films where (a) shows the decomposition curves for films with increasing number of particle layers and ESEM images of the composite film cross-sections with (b) 1, (c) 2, (d) 3, and (e) 6 particle layers. Scale bars represent 10 μm .

The PVDF/BaTiO₃ and PC/BaTiO₃ composite films were also characterized electrically. To determine the dielectric constant (ϵ) and dielectric loss tangent ($\tan \delta$), top and bottom contact gold electrodes were sputter-coated onto the films, and measurements were made using an LCR meter (L – Inductance, C – Capacitance, R – Resistance). Frequency sweeps (1 kHz - 1 MHz) of capacitance (C) and $\tan \delta$ were performed. ϵ was calculated from measured capacitance values using Equation 5.1. The dielectric strength (V_B , breakdown voltage) was measured using an in-house breakdown voltage set-up. A ball-plane electrode assembly was used for the breakdown measurements, and the film sample was kept

immersed in Fluorinert FC40 during measurements. The set-up is shown schematically in Figure 5.17. From these measurements, the maximum energy density (E_{max}) of the composite film was calculated according to Equation 5.2.

$$C = \frac{\epsilon_o \epsilon A}{d} \quad \text{Equation 5.1}$$

$$E_{max} = \frac{1}{2} \epsilon_o \epsilon E_B^2 \quad \text{Equation 5.2}$$

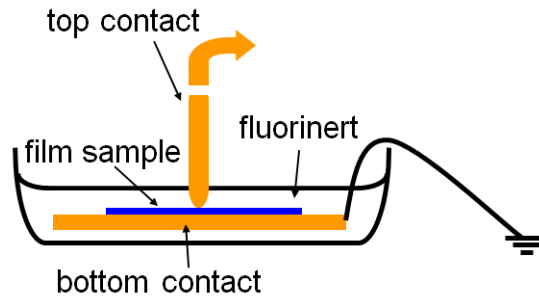


Figure 5.17. Schematic illustration of the breakdown testing apparatus

The results from a series of PVDF/BaTiO₃ and PC/BaTiO₃ composite films are presented in Table 5.2. Higher volume fractions were achievable with the PC/BaTiO₃ composite films because the PC films were stronger and did not disintegrate when very thin. For the series of PC films, ϵ remained fairly constant (3.4 – 3.6) up to 6.4 wt% BaTiO₃, but increased considerably to 6.51 with 18.4 wt% BaTiO₃. The breakdown voltage remained constant up to 3.5 wt% BaTiO₃, then decreased to 222 V/ μ m at 18.4 wt% BaTiO₃. As E_{max} is proportional to V_B^2 , E_{max} exhibited a similar trend to V_B , and decreased with increasing BaTiO₃ wt%. The PVDF/BaTiO₃ composite films did not exhibit any clear trends in electrical properties as a function of BaTiO₃ wt%. In both cases, the energy density of the films was not improved by the addition of BaTiO₃. It is suspected that poor film quality –

film inhomogeneity and air voids – as well as low particle volume fractions, adversely affected the properties of the films.

Table 5.2. Electrical characterization of PC/BaTiO₃ and PVDF/BaTiO₃ composite films

Wt% BaTiO ₃	ϵ^*	$\tan \delta (\%)*$	V_B (V/ μm)	E_{max} (J/cc)
PC				
0	3.63 \pm 0.23	0.36 \pm 0.06	438 \pm 92	3.2
2.2	3.32 \pm 0.03	0.31 \pm 0.08	437 \pm 45	2.5
3.5	3.45 \pm 0.08	0.25 \pm 0.06	436 \pm 47	3.0
6.4	3.38 \pm 0.02	0.34 \pm 0.03	318 \pm 29	1.8
18.4	6.51 \pm 0.32	1.08 \pm 0.12	222 \pm 20	1.5
PVDF				
0	9.98 \pm 2.12	2.70 \pm 0.47	283 \pm 55	3.9
8.1	9.85 \pm 0.69	1.91 \pm 0.17	339 \pm 100	4.3
10.3	11.0 \pm 1.3	2.05 \pm 0.13	317 \pm 60	4.3
10.9	10.8 \pm 0.5	2.03 \pm 0.11	310 \pm 52	3.9

*Frequency at 1 kHz

Due to the limits in the maximum volume fraction achievable using the sol-gel method for particle fabrication, alternative methods that did not require a calcination step were investigated. The use of commercially available BaTiO₃ powders was explored. In one example, a curable monomer suspension, consisting of 50 wt% BaTiO₃ powder, 49 wt% bis[(2-methacryloxy)ethyl]phosphate and 1 wt% DEAP, was used to fabricate composite

particles for the composite film. The resulting film had 3 distinct phases: the BaTiO₃ nanoparticles randomly dispersed within a second phase of ordered microparticles of a crosslinked resin uniformly dispersed within a PVDF continuous matrix (Figure 5.18). The dielectric properties of this film were found to be: $\epsilon = 7.9 \pm 0.4$, $\tan \delta = 3.2 \pm 0.3 \%$ and $V_B = 238 \pm 41 \text{ V}/\mu\text{m}$. Alternatively, a suspension of the BaTiO₃ nanoparticles in a volatile solvent was used to fill the mold. Unfortunately, large amounts of scum accumulated on the surface of the mold, so this approach needs more optimization.

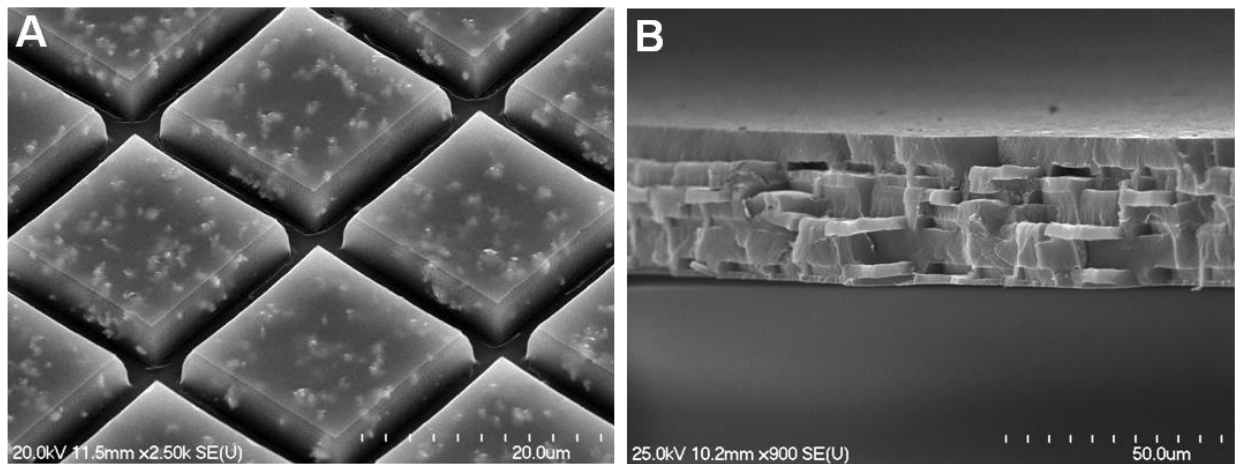


Figure 5.18. (A) SEM image crosslinked phosphate resin/BaTiO₃ composite particles on a harvesting layer and (B) SEM image of a cross-section of a tri-phasic PVDF/crosslinked phosphate resin/BaTiO₃ composite film

5.2.2.4 Polymer/metal

The fabrication of ordered polymer/metal composite films was also achieved using the same fabrication method described for the thermoplastic systems. The PFPE mold was filled with silver paste and the solvent was allowed to evaporate. A thin film of PC was brought into contact with the mold, and after applying heat and pressure, the mold was removed transferring the silver to the PC layer. The layers were stacked and melt-pressed as

described previously. In Figure 5.19, ESEM images of the harvesting layer and the ordered composite film are displayed.

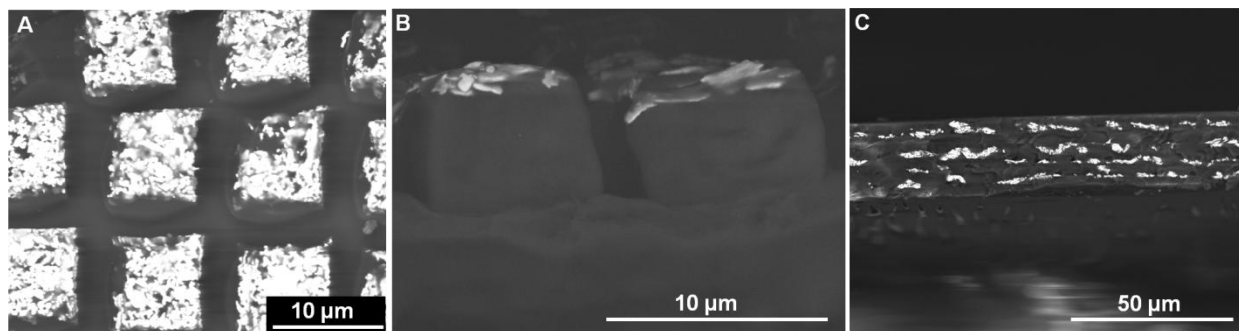


Figure 5.19. ESEM images of (a) top view harvesting layer with silver flakes on PC, (b) side view harvesting layer with silver flakes on PC and (c) PC/silver ordered composite film

5.3 Conclusions and Future Outlook

A versatile, scalable, composite film fabrication process that allows for the tailoring of composite film nano- and microstructures has been described in this chapter. The PRINT process was adapted to composite film fabrication because an important advantage of the PRINT process is that the particles are fabricated in an intrinsically non-aggregated state. With such 2-dimensional arrays of nano- and micro-particles, simple strategies can be employed to transfer the particles to a matrix without aggregation to build up more complex, hierarchically ordered, 3-dimensional structures. Films were fabricated with different material combinations to yield structurally complex films with well-defined morphologies in which uniformly shaped polymeric or inorganic particles of one component were evenly dispersed with a desired periodicity within the other component. The scalability of the PRINT process, as a particle fabrication technology, has been demonstrated commercially

with continuous manufacturing,¹² and so the techniques described herein can be readily adapted to roll-to-roll technology.

For the case of polymer/polymer composite films, to attain the same morphological control via the blending of immiscible polymers, stringent control of numerous processing conditions is required.¹⁷ Additionally, the PRINT polymer composite films have domain sizes and morphologies that rival blended polymer and block copolymer systems; and unlike these other approaches, with the PRINT process it is possible to take polymers that are typically miscible, and produce composites with well-ordered domains. Given the fact, that novel combinations of materials and unique types of nanostructures are available with this process that cannot be accessed otherwise, there is great promise in numerous optical, sensor and biomedical applications. For the polymer/ceramic composite films, there is still great promise in using this process, however optimization is required especially as dielectric properties are strongly affected by film defects. Alternative approaches to the sol gel route to BaTiO₃ particles would benefit the overall film fabrication, and the concept of using the PFPE mold to pattern commercial BaTiO₃ nanopowders into shape specific aggregates is one promising route.

5.4 References

1. Feenstra, J.; Sodano, H. A. *J. Appl. Phys.* **2008**, 103, 124108-5.
2. Kim, P.; Doss, N. M.; Tillotson, J. P.; Hotchkiss, P. J.; Pan, M.-J.; Marder, S. R.; Li, J.; Calame, J. P.; Perry, J. W. *ACS Nano* **2009**, 3, 2581-2592.
3. Lott, J.; Xia, C.; Kosnosky, L.; Weder, C.; Shan, J. *Adv. Mater.* **2008**, 20, 3649-3653.
4. Schroeder, R.; Majewski, L. A.; Grell, M. *Adv. Mater.* **2005**, 17, 1535-1539.
5. Hampton, M. J.; Williams, S. S.; Zhou, Z.; Nunes, J.; Ko, D.-H.; Templeton, J. L.; Samulski, E. T.; DeSimone, J. M. *Adv. Mater.* **2008**, 20, 2667-2673.
6. Guo, N.; DiBenedetto, S. A.; Kwon, D.-K.; Wang, L.; Russell, M. T.; Lanagan, M. T.; Facchetti, A.; Marks, T. J. *J. Am. Chem. Soc.* **2007**, 129, 766-767.
7. Kim, P.; Jones, S. C.; Hotchkiss, P. J.; Haddock, J. N.; Kippelen, B.; Marder, S. R.; Perry, J. W. *Adv. Mater.* **2007**, 19, 1001-1005.
8. Tomer, V.; Randall, C. A.; Polizos, G.; Kostelnick, J.; Manias, E. *J. Appl. Phys.* **2008**, 103, 034115-7.
9. Brosseau, C.; Beroual, A.; Boudida, A. *J. Appl. Phys.* **2000**, 88, 7278-7288.
10. Calame, J. P. *J. Appl. Phys.* **2006**, 99, 084101-11.
11. Gratton, S. E. A.; Williams, S. S.; Napier, M. E.; Pohlhaus, P. D.; Zhou, Z.; Wiles, K. B.; Maynor, B. W.; Shen, C.; Olafsen, T.; Samulski, E. T.; DeSimone, J. M. *Acc. Chem. Res.* **2008**, 41, 1685-1695.
12. Merkel, T.; Herlihy, K.; Nunes, J.; Orgel, R.; DeSimone, J. M. *Langmuir* **2009**, in press.
13. Rolland, J. P.; Maynor, B. W.; Euliss, L. E.; Exner, A. E.; Denison, G. M.; DeSimone, J. M. *J. Am. Chem. Soc.* **2005**, 127, 10096-10100.
14. Lu, S.; Anseth, K. S. *J. Controlled Release* **1999**, 57, 291-300.
15. Harizanov, O.; Harizanova, A.; Ivanova, T. *Mat. Sci. Eng. B* **2004**, 106, 191-195.
16. Fu, X.; Song, Z.; Wu, G.; Huang, J.; Duo, X.; Lin, C. *J. Sol-Gel Sci. Technol.* **1999**, 16, 277-281.
17. Tran-Cong-Miyata, Q.; Nishigami, S.; Ito, T.; Komatsu, S.; Norisuye, T. *Nat. Mater.* **2004**, 3, 448-451.